2007

MACHINE VISION RECOGNITION OF THREE-DIMENSIONAL SPECULAR SURFACE FOR GAS TUNGSTEN ARC WELD POOL

Hongsheng Song
University of Kentucky, hs.song@uky.edu

Recommended Citation

Song, Hongsheng, "MACHINE VISION RECOGNITION OF THREE-DIMENSIONAL SPECULAR SURFACE FOR GAS TUNGSTEN ARC WELD POOL" (2007). *University of Kentucky Doctoral Dissertations*. 531.
https://uknowledge.uky.edu/gradschool_diss/531

ABSTRACT OF DISSERTATION

Hongsheng Song

The Graduate School

University of Kentucky

2007

MACHINE VISION RECOGNITION OF THREE-DIMENSIONAL SPECULAR SURFACE FOR GAS TUNGSTEN ARC WELD POOL

ABSTRACT OF DISSERTATION

A dissertation submitted in partial fulfillment of the
requirements for the degree of Doctor of Philosophy in the
College of Engineering
at the University of Kentucky

By
Hongsheng Song

Lexington, Kentucky

Director: Dr. YuMing Zhang, Professor of Electrical Engineering

Lexington, Kentucky

2007

ABSTRACT OF DISSERTATION

MACHINE VISION RECOGNITION OF THREE-DIMENSIONAL SPECULAR SURFACE FOR GAS TUNGSTEN ARC WELD POOL

Observing the weld pool surface and measuring its geometrical parameters is a key to developing the next-generation intelligent welding machines that can mimic a skilled human welder who observes the weld pool to adjust welding parameters. It also provides us an effective way to improve and validate welding process modeling. Although different techniques have been applied in the past few years, the dynamic specular weld pool surface and the strong weld arc complicate these approaches and make the observation /measurement difficult.

In this dissertation, a novel machine vision system to measure three-dimensional gas tungsten arc weld pool surface is proposed, which takes advantage of the specular reflection. In the designed system, a structured laser pattern is projected onto the weld pool surface and its reflection from the specular weld pool surface is imaged on an imaging plane and recorded by a high-speed camera with a narrow band-pass filter. The deformation of the molten weld pool surface distorts the reflected pattern. To derive the deformed surface of the weld pool, an image processing algorithm is firstly developed to detect the reflection points in the reflected laser pattern. The reflection points are then matched with their respective incident rays according to the findings of correspondence simulations. As a result, a set of matched incident ray and reflection point is obtained and an iterative surface reconstruction scheme is proposed to derive the three-dimensional pool surface from this set of data based on the reflection law. The reconstructed results proved the effectiveness of the system.

Using the proposed surface measurement (machine vision) system, the fluctuation of weld pool surface parameters has been studied. In addition, analysis has been done to study the measurement error and identify error sources in order to improve the measurement system for better accuracy. The achievements in this dissertation provide a useful guidance for the further studies in on-line pool measurement and welding quality control.

KEYWORDS: Machine Vision, Welding Sensor, Specular Surface, Image Processing, Reconstruction

Hongsheng Song

07/24/2007

MACHINE VISION RECOGNITION OF THREE-DIMENSIONAL SPECULAR SURFACE FOR GAS TUNGSTEN ARC WELD POOL

By

Hongsheng Song

YuMing Zhang
Director of Dissertation

YuMing Zhang
Director of Graduate Studies

07/24/2007
Date

DISSERTATION

Hongsheng Song

The Graduate School

University of Kentucky

2007

MACHINE VISION RECOGNITION OF THREE-DIMENSIONAL SPECULAR SURFACE FOR GAS TUNGSTEN ARC WELD POOL

DISSERTATION

A dissertation submitted in partial fulfillment of the
requirements for the degree of Doctor of Philosophy in the
College of Engineering
at the University of Kentucky

By
Hongsheng Song

Lexington, Kentucky

Director: Dr. YuMing Zhang, Professor of Electrical Engineering

Lexington, Kentucky

2007

DEDICATED TO MY FAMILY

ACKNOWLEDGEMENT

The research work in this dissertation is funded by the National Science Foundation Project under grant DMI-0527889, Kentucky Opportunity Fellowship and University of Kentucky Center for Manufacturing.

Firstly I would like to sincerely thank my advisor Dr. YuMing Zhang for his invaluable guidance, continuous encouragement and constructive instructions. I am also grateful to Drs. Bruce L. Walcott, Alan T. Male, Jingshan Li, I. S. Jawahir and Larry Holloway for their helpful insight and supervision. Some of my early research work was done with the help of Dr. Gohar M. Saeed, and here I want to thank him. Also I want to thank all of my colleagues in the Welding Research Lab: Jinsong Chen, Xiaodong Na, Kun Qian, Kehai Li, Xiaopei Liu, Yu Shi, Yi Huang, Zhenzhou Wang, Xiangrong Li, Yan Shao, Aparna Janga and Xiaoji Ma for their helpful suggestions for my work.

In addition, I want to give my thanks to my parents and brother for their endless love and support throughout all my life. Lastly I'd like to express my great appreciation to my wife, Jinrong, for bringing me and sharing with me so many wonderful things in my life.

TABLE OF CONTENTS

LIST OF TABLES

LIST OF FIGURES

CHAPTER 1

INTRODUCTION

1.1 Background

Welding processes are widely used in many manufacturing areas, such as automotive, aerospace and shipbuilding industries. Meanwhile, welding is a labor intensive and skilled operation. Although current welding robots can provide consistent motion to assure and help to improve weld productivity, they lack the intelligent capabilities that human welders possess to achieve good weld quality through observation of the welding process. Thus, being more intelligent is the ultimate direction for the next-generation automated welding machines. Since skilled human welders can achieve good welding quality (full penetration) by concentrating on observing the weld pool (surface), the pool surface must contain sufficient information about the weld quality. In addition, the research on weld pool surface can also help better understand complex welding processes and provide critical experimental data to validate numerical weld pool models. Hence observation and measurement of three-dimensional weld pool surfaces become a fundamental capability that next generation automated welding machines and welding researchers must possess, and a number of early efforts have been devoted to sensing weld pool related parameters by using a few methods including machine vision technology, X-ray radiation, ultrasonic and acoustic emission etc. [1] [2] [3] [4].

Among existing methods, vision-based ones have been studied more extensively. In machine vision based methods, vision-based sensors acquire images from the weld pool and image processing algorithm is followed to analyze and extract weld pool related parameters so that control systems can use these parameters as feedback to adjust welding parameters [5] [6] [7]. Early work on vision-based direct view of weld pool has been done in the Welding Research Laboratory at the University of Kentucky using a specially designed commercial camera whose high speed shutter is synchronized with a short duration pulsed laser [5]. This camera allows the arc light be eliminated from the image to acquire a weld pool image shown in Figure 1-1 (a). As a result, the two-dimensional boundary of the weld pool is clearly captured. To use this camera in three-dimensional weld pool surface imaging, a special technique was used which projected the structured illumination laser through a frosted glass [6], and the acquired one of the images is shown in Figure 1-1 (b) [6]. In a separate effort, Mnich and his colleagues used stereovision methods to determine the three-dimensional shape of the weld pool [7]. Another effort used similar principle but introduced the biprism technique to reduce the number of needed cameras from two to one [8].

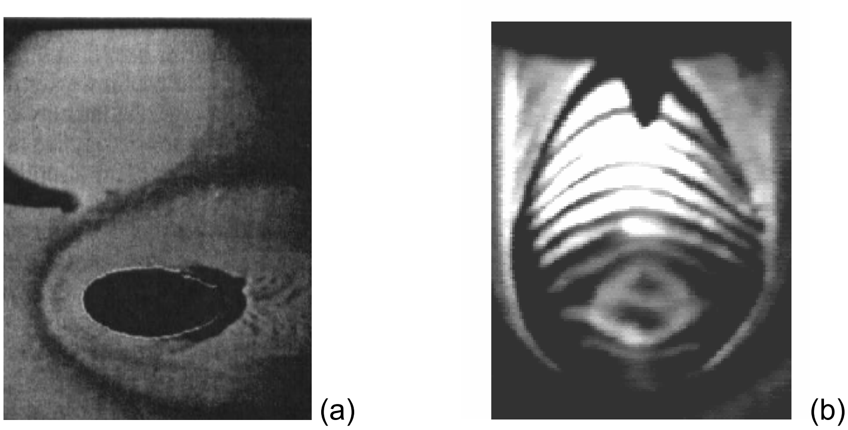

Figure 1-1, Captured Images for (a) 2D measurement [5] and (b) 3D measurement [6]

While all these methods have achieved certain successes, they are still not practical for commercial use. For example, although the special camera with laser-shutter synchronization can acquire beautiful images using a frosted glass like that in Figure 1-1 (b), the camera is extremely expensive and its speed can only reach 30 frames per second because it uses pulsed illumination laser to suppress the arc light while the average power of illumination laser is relatively low. Because the weld pool surface is highly dynamic, acquiring useful information on weld pool surface requires a much higher imaging frame rate.

1.2 Objective and Approach

Observing the weld pool surface and measuring its geometrical parameters is very important for the development of next generation intelligent welding machine and for the modeling/control of complex welding processes. Unfortunately, the strong weld arc and the dynamic specular weld pool surface prevent all existing commercial vision systems from being qualified. In addition, the sensor must function in the environment of welding which is known to be harsh. Hence, although the measurement of the weld pool surface is important, limited valuable work has been done in this area and the welding community still requires methods which are more robust, accurate, cost effective, and suitable for welding environment.

As a part of NSF project “Sensor: measurement of dynamic weld pool”, the objective of our study in this dissertation is to build an innovative sensor using machine vision techniques which can measure a highly dynamic gas tungsten arc (GTA) weld pool surface despite the pool's specular nature and the presence of bright plasma arc.

As mentioned earlier, the bright arc and specular weld pool surface are the two major difficulties for observing the weld pool. Based on the previous work [4] [5] [6], a new approach [9] [10] is proposed to observe and measure (reconstruct) three-dimensional gas tungsten arc (GTA) weld pool surfaces using non-contact top-side optical sensor in this dissertation. Here gas tungsten arc welding is the primary arc welding process for precision joining of metals. In the proposed machine vision sensing system, a structured light pattern (multiple-line or dot-matrix) produced by a low-power illumination laser diode is projected onto the weld pool surface and the corresponding specular reflection is observed on a particular imaging plane by a high-speed camera. Because the arc radiation decays very fast with the travel distance while the reflection of the projected laser almost remains its intensity, it is possible that the reflection of the projected laser can be clearly imaged on the imaging (interception) plane. Since the imaging on the interception plane is continuous, the imaging speed is only affected by the frame rate of the camera used. It is apparent that this proposed method is more cost-effective, convenient, robust, and suitable for manufacturing applications. From the reflected images, the dynamic changes of weld pool surface can be observed and the impact of weld parameters during the process can also be analyzed [9].

Furthermore, the reflected images can be processed to extract some useful information, such as the positions of reflected laser lights and some features of the reflected pattern, to help us understand the process and provide necessary data for the later weld pool surface reconstruction scheme [11] [12]. Although the formation of the image is governed by the reflection law, the image itself does not provide an intuitive view about the dimensions of the weld pool surface. Thus the related reconstruction scheme can be proposed to derive the three-dimensional shape of the weld pool surface by solving an inverse problem of the reflection law [13]. In addition, the recognition ability of the proposed system can help us to investigate the behaviors of the weld pool surface in different welding applications.

Briefly, the main approach to reach our goal includes three relatively simple ideas:

(1) Exploit the difference between propagation in structured laser light and plasma arc to clearly image laser rays mirrored from the weld pool surface in the presence of bright plasma, thus changing the specular surface from a difficulty to an advantage;

(2) Apply machine vision (image processing) techniques to extract useful information from the captured reflected images;

(3) Based on the acquired data and reflection law, develop reconstruction scheme to effectively rebuild the three-dimensional weld pool surface.

1.3 Organization

In this dissertation, a machine vision sensing system is developed to recognize (measure) three-dimensional specular gas tungsten arc weld pool surface, and the main research steps and results are discussed sequentially in the following chapters. The relationships among the chapters are shown in Figure 1-2.

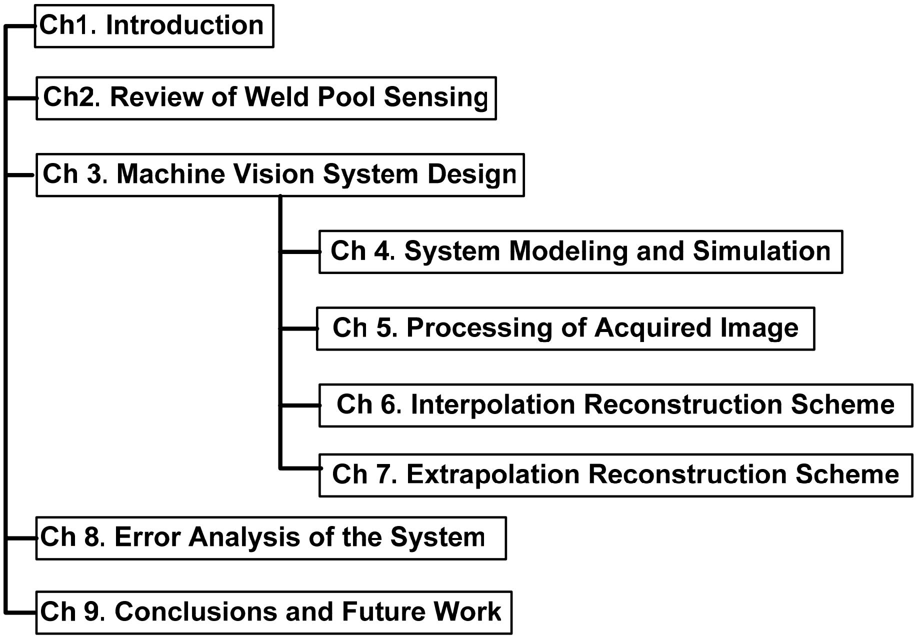

Figure 1-2, Organization of the dissertation

In Chapter 1 “Introduction”, the research background, objective and the proposed method are presented.

In Chapter 2 “Review of Weld Pool Sensing”, a number of previous approaches developed for sensing the weld pool surface in various welding applications, such as gas tungsten arc welding (GTAW), gas metal arc welding (GMAW) and laser welding, are discussed in detail. The applied sensing techniques include machine vision, X-ray radiation, ultrasonic, thermal sensing and so on.

Chapters 3 - 8 present the whole proposed machine vision sensing system. The main achievements and contributions of this dissertation are also discussed.

In Chapter 3 “Machine Vision System Design”, a new machine vision sensing system using structured laser light is proposed. In this system, multiple-line or dot-matrix pattern of structured laser light is projected onto the molten specular weld pool surface and the reflection is intercepted by an imaging plane. At the same time, the reflected image is captured by a high-speed camera. In this chapter, the system configuration is described and the acquired reflected images are also shown, which proved the feasibility of the proposed method. A 19-by-19 commercially available dot-matrix pattern is selected as the projected structured light for our study.

In Chapter 4 “System Modeling and Simulation”, different coordinate systems used to model the proposed sensing system are discussed. In the meanwhile, the correspondence simulation is conducted to investigate the possible corresponding relationships between the reflected dots on the imaging plane and the projected rays in the dot matrix. Different shapes (concave and convex) and different dimensional parameters (width, length and depth) of weld pool surface are tested according to the practical situations. The simulation results effectively direct the development of weld pool reconstruction scheme.

Chapter 5 “Processing of Acquired Image” present the developed imaging processing algorithms applied for calibration image and reflected image. The calibration image is taken before the experiment used for imaging plane calibration and the proposed axis identification algorithm extracts the axes on imaging plane. In the reflected image, the deformed dot-matrix reflection pattern is captured, and accordingly dot extraction algorithm and feature extraction algorithm are proposed to obtain some useful information.

Based on achieved information, in Chapter 6 “Interpolation Reconstruction Scheme” and Chapter 7 “Extrapolation Reconstruction Scheme”, two schemes which are called IRS and ERS are discussed in detail. In both schemes, slope-based surface reconstruction method and two-dimensional boundary model are included. The main difference between ERS and IRS is the way to derive the surface and determine the surface boundary. Their reconstruction results are shown and compared. Especially in Chapter 7, the variation of the weld pool surfaces is investigated.

In Chapter 8 “Error Analysis of System”, the errors of the reconstructed three-dimensional weld pool surface by using the proposed machine vision measurement system are investigated and analyzed. The experimental results show the small measurement error is acceptable and the system limitation error and reconstruction methodology error is insignificant, which verify the accuracy of the proposed three-dimensional weld pool surface measurement system.

At last, in Chapter 9 “Conclusion and Future Work” the main findings and contributions are concluded and the future research work to improve the system is also addressed.

CHAPTER 2

REVIEW OF WELD POOL SENSING

2.1 Overview

With the development of new welding technologies, such as laser welding, in recent years the welding process has been widely applied in manufacturing industries from vehicle assembly in automotive production to the joining of micro-electric components in electronics field [14]. Intelligent welding machine has become the trend of next generation welding application. A primary concern over the industry spectrum is how to monitor and control welding quality fast, reliably and cost-effectively. Therefore, a number of on-line inspection and sensing systems have been developed to monitor welding quality, control welding process and reduce overall costs.

As a kind of welding process, Gas Tungsten Arc Welding (GTAW) often must be used to produce high-quality weld because of its capability in precision control of the fusion process [15]. The general procedures of GTAW are as below. Firstly, two pieces of metal are placed side by side and the welding torch is set above the seam. Then during the welding process, torch or work piece will be moved along the seam at a certain speed and the high-temperature welding arc under a certain current will melt the metal along the seam. At last, the two work pieces are joined together shortly after cooling down. To decide the quality of the welding process, the penetration depth is used as a very important criterion. The extent of penetration can be further decided by the top-side and back-side bead widths, which can be measured or deduced by the shape of weld pool surface during welding process [16].

Figure 2-1 shows some different penetration statuses in the welding process from the profile view. Generally the full penetration in Figure 2-1 (a) is desired and even need 100% guaranteed for some critical applications. If partial penetration in Figure 2-1 (b) is allowed to prevent burn-through, welds may be made using the established procedure with a welding robot if the seam tracking accuracy is met [17]. However, over-penetration in Figure 2-1 (c) should be avoided since it will damage material properties. From the figures, it can be seen that different shapes of weld pool surface are associated with different welding situations, and depend on different welded metals and welding parameters the shape of weld pool surface is different. Thus some mathematical models can be established to decide the penetration status from observed weld pool surface [18].

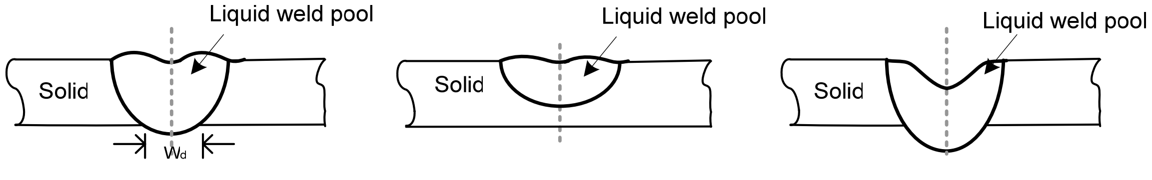

(a) Full-penetration (b) Partial-penetration (c) Over-penetration

Figure 2-1, Different penetration statuses (profiles) in the welding process [17]

In this chapter, firstly some vision-based weld pool observation methods are introduced and they can be classified as a kind of the machine vision application, which is also used in our study. Then other different techniques used for sensing the welding process, such as x-ray, ultrasonic and acoustic sensors, are reviewed. These techniques cover many types of applications including laser welding, gas tungsten arc welding (GTAW), gas metal arc welding (GMAW) and plasma arc welding (PAW). Their advantages and limitations are also discussed.

2.2 Vision-based Technique

As a vision-based technique, machine vision (MV) is the application of computer vision to industry and manufacturing [19]. Whereas computer vision is mainly focused on machine-based image processing, machine vision most often requires also digital input/output devices and computer networks to control other manufacturing equipment such as robotic arms. Machine Vision is a subfield of engineering that encompasses computer science, optics, mechanical engineering, and industrial automation. The relation between machine vision and various other fields is shown in Figure 2-2. Machine vision systems are programmed to perform narrowly defined tasks such as counting objects on a conveyor, reading serial numbers, and searching for surface defects.

Computers do not "see" in the same way that human beings are able to. Cameras are not equivalent to human optics and while people can rely on inference systems and assumptions, computing devices must "see" by examining individual pixels of images, processing them and attempting to develop conclusions with the assistance of knowledge bases and features such as pattern recognition engines. Although some machine vision algorithms have been developed to mimic human visual perception, a number of unique processing methods have been developed to process images and identify relevant image features in an effective and consistent manner.

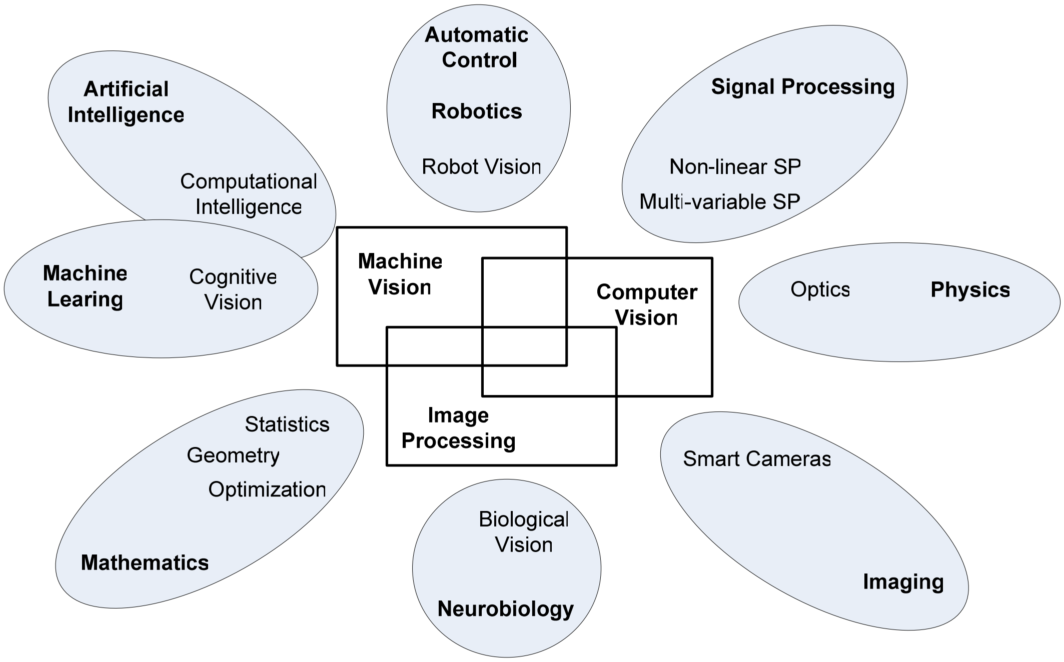

Figure 2-2, Relation between machine vision and various other fields [19]

In the welding process, the vision-based sensors are used to determine the state of the weld pool. Generally, a human welder uses vision to see the weld pool and decide the state of weld process, and then the parameters, such as weld current and speed, are adjusted accordingly. In the same way, vision-based sensors acquired the images of the weld pool as the function of eyes, and image processing is done after that to tell the shape of weld pool surface. Then the related control algorithms will be applied to adjust the parameters of the process to ensure the welding quality [20]. Usually the vision-based sensors can be divided into two categories: two-dimensional and three-dimensional [21].

2.2.1 Two-dimensional observation and analysis

Two-dimensional (2D) shape of the weld pool has been studied by many means. The 2D geometric parameters, such as the length, width and area, are used to develop a model to predict the penetration of the weld work pieces. In this area, the generic method is using monochrome or color cameras with a band-pass filter to acquire weld pool images. Here some of them [21] are presented.

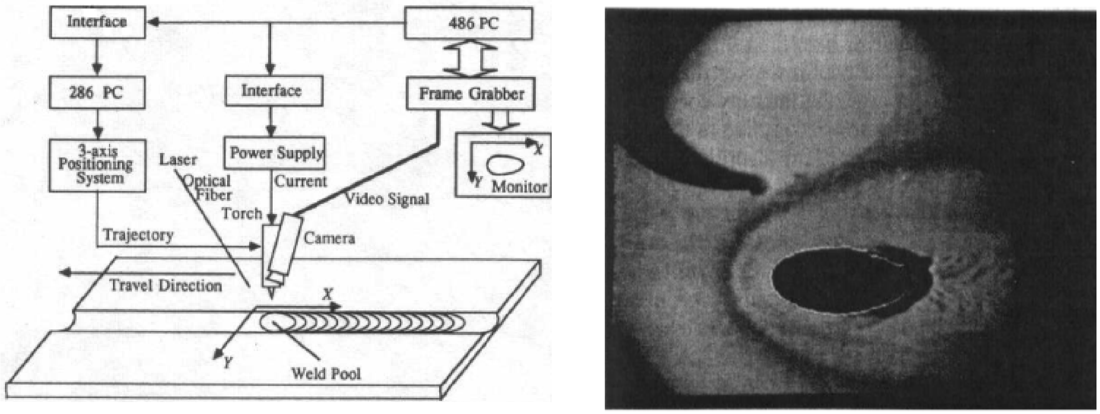

Figure 2-3, Experiment set-up and the acquired image [22]

An earlier work was done in the University of Kentucky [22] by using the laser strobe system. The laser strobe system includes a pulse laser illumination unit, a camera head and a system controller. The laser wavelength is centered at 337.1 nm and a camera fitted with an optical filter in wavelength 330-340nm is used to observe the weld pool at an angle to the welding direction (see Figure 2-3). Since the camera is synchronized with the pulsed laser, the laser power density during ‘on’ duration is much higher than welding arc and clear images of weld pool surface can be captured as shown in Figure 2-3. On-line weld pool edge extraction is done based on the grayness difference and its directional gradient among the weld pool, the heat affected zone (HAZ) and the base metal. Meanwhile the weld pool area was controlled by using an adaptive algorithm. To prove the effectiveness of the control system, various experiments have been performed by using different system parameters. The experimental results verified the controller could maintain the pool size closer to the desired level with the variations in the system.

Another important technique for a 2D weld pool boundary measurement is the co-axial viewing of the weld pool. It was first proposed by Richardson et al [23]. It has been widely investigated by some researchers. In the co-axial viewing method, the electrode is used to block the arc.

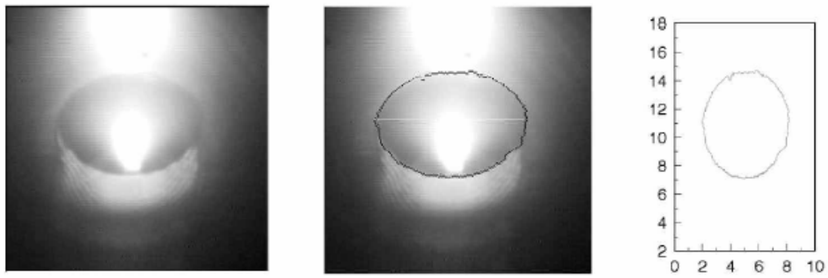

(a) raw image (b) processed image (c) weld pool of real size

Figure 2-4, Weld pool geometry at current of 90 A and speed of 103mm/s [24]

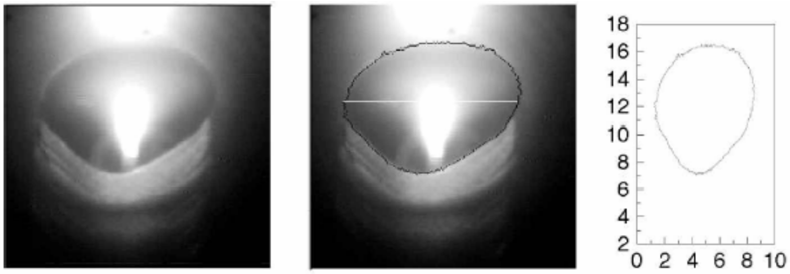

(a) raw image (b) processed image (c) weld pool of real size

Figure 2-5, Weld pool geometry at current of 100 A and speed of 113mm/s [24]

Different type of research was done by Wu et al. from the Institute of Material Joining at Shandong University, China [18]. They used a regular CCD sensor having a resolution of 600 TV lines and 8 shutter speeds. The CCD was fitted with a narrow band filter centered at 610 nm, bandwidth 20 nm and transparency of 27%. A series of image processing algorithms were then performed such as eliminating the noise, enhancing contrast and extracting edges of the weld pool.

The two-dimensional size (length and width) of the weld pool is determined by using the calibration transformation of 0.043mm/pixel. Figure 2-4 and Figure 2-5 show some of the images captured, the result of the image processing, and the extracted shape of the weld pool [24]. The research performed had practical implementations in the industry since the equipment used was cheap, and was based on passive sensing (no laser). However the measurement was only two-dimensional and the state of the weld pool penetration cannot be precisely determined by it.

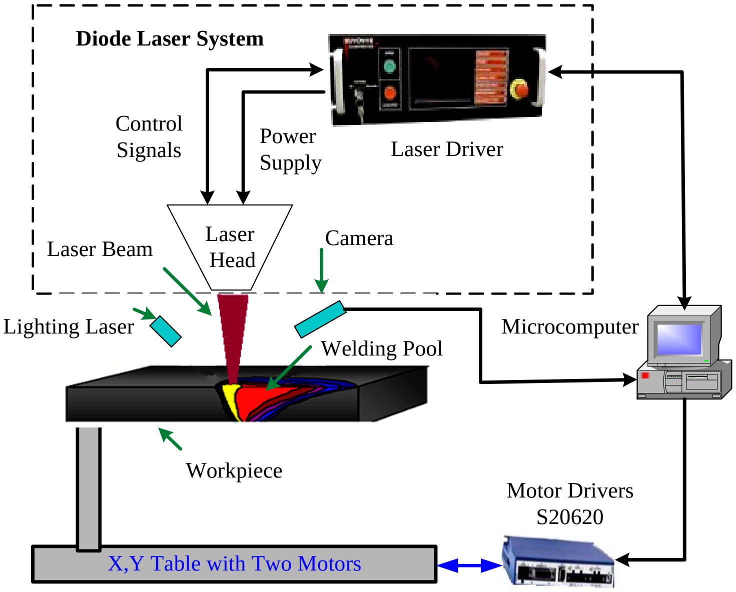

Figure 2-6, Welding fixture and hardware of control system [25]

The same laser strobe system mentioned above is also used for sensing and controlling the two-dimensional weld pool in laser welding by Duan et.al [25]. The proposed system is shown in Figure 2-6 and the captured weld pool images under different driver current and work piece travel speed are shown in Figure 2-7 and Figure 2-8. As can be seen, the size of weld pool increases with the increase of welding current and speed. Based on the acquired 2D weld pool information, a Cerebellar Model Articulation Controller- (CMAC-) based modeling method and closed-loop control system were developed to estimate and control the weld fusion by measuring the topside and backside bead widths of the weld pool in laser welding. The results of closed-loop control simulations in laser welding process demonstrate that the developed control system is effective and robust to fluctuations or variations that lead to the changing parameters of the non-linear model.

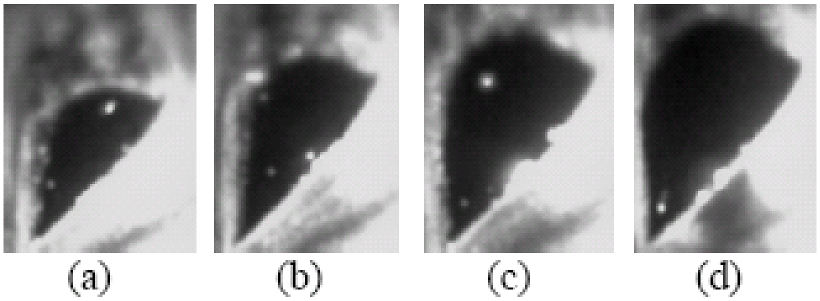

Figure 2-7, Weld pools with different welding current. Speed: 3.86 mm/s; laser beam angle: 52 degree, 1 mm stainless steel, (a) 33.1 A, (b) 35.3 A, (c) 37.7 A, (d) 39.5 A

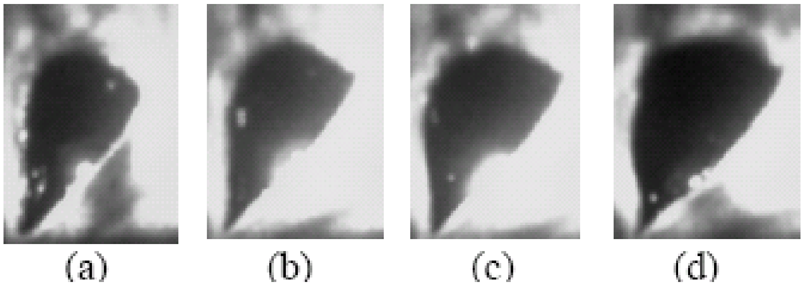

Figure 2-8, Weld pools with different welding speed. Current: 35 A; laser beam angle: 52 degree,1mm stainless steel, (a) 4.43 mm/s, (b) 3.87 mm/s, (c) 3.3 mm/s, (d) 2.74 mm/s

2.2.2 Three-dimensional observation and analysis

Three-dimensional (3D) observations/measurements provide more insight on the state of the weld pool by adding another dimension, the depth of depression, to the measurement. More detailed information about the condition of the weld pool can also be determined in 3D measurement experiments. For 3D analysis, many techniques such as stereovision, biprism and structured light have been used to determine the depth of the weld pool experimentally [21].

The first true 3D observation method for the weld pool surface was developed at Welding Research Laboratory, University of Kentucky (UK) based on two major advances [26]. First, to eliminate the influence of the bright arc light, a short duration pulsed laser was projected onto the weld pool and the camera shutter was synchronized with the pulse duration. The arc light was essentially eliminated from the image when the shutter speed was fast enough. Second, a special technique [26] was proposed in order to acquire information from the specular surface. In fact, common practice for measuring a surface is to project a structured light onto the surface and sense the diffuse reflection from the surface [27] [28] [29]. Unfortunately, the weld pool surface is specular and no substantial amount of structured light can be reflected diffusely. The special technique proposed in [26] is to project the laser through a frosted glass so that the laser's travel direction changes because any point of the frosted glass becomes a new point light source which disperses light with a certain diffuse angle. The camera views the slits (grid openings) through their reflection from the weld pool surface. Their virtual image [30] consists of bright stripes deformed by the weld pool surface deformation and is sensed by the camera [26]. The resultant image contains the information about the shape of the weld pool surface.

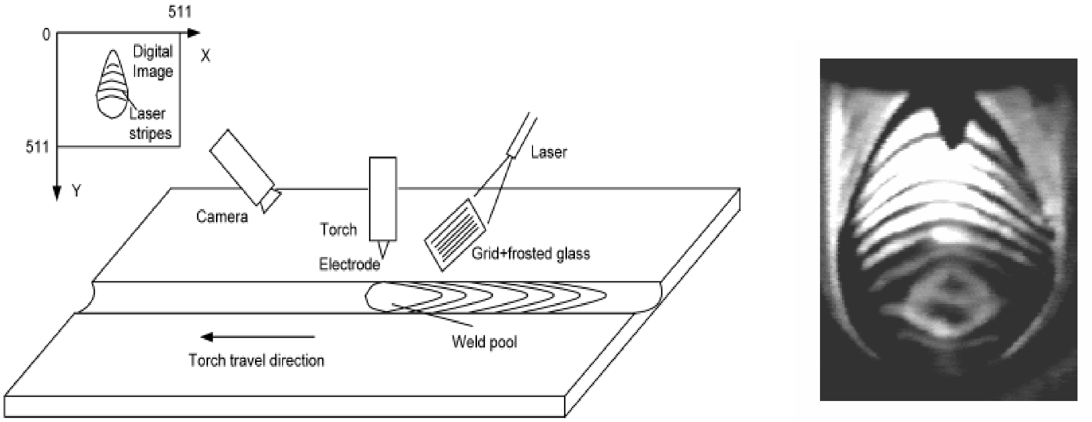

Figure 2-9, Experiment scheme and image acquired under high power pulsed laser [26]

In the experiments the camera observed the weld pool at an angle to the direction of the weld (Figure 2-9) and the weld pool area was controlled using an adaptive algorithm. A complete weld pool detection and edge extraction in real time was written based on the grayness difference and directional gradient of grayness between the weld pool and the heat affected zone (HAZ) and the base metal. As can be seen, the above method is capable of obtaining specular reflection from the weld pool surface in the presence of the bright arc. However, the synchronization of the laser and high-speed shutter requires specific, high-cost and sophisticated equipment, which is not suitable for use in production. More critically, to suppress the arc, the power of the laser during the pulse must be very high (70 kW for images shown in Figure 2-9) and the frame rate thus cannot be very high (30 frames per second for images in Figure 2-9) because a high frame rate would increase the average power of the illumination laser.

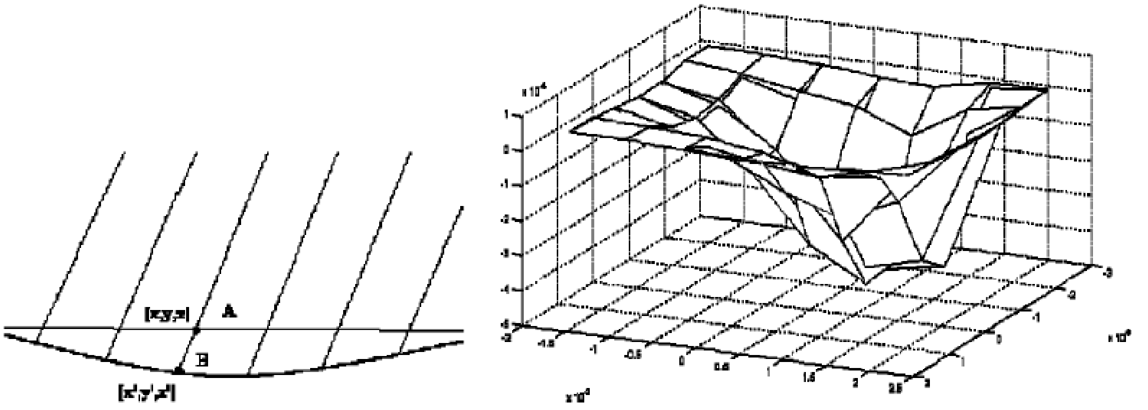

(a) (b)

Figure 2-10, Simulation of 3D weld pool surface (a) Approximation of reflection point (b) Estimated weld pool surface from slope field [31]

Saeed, Lou and Zhang at the University of Kentucky have done some numerical simulations using slope field and point tracking techniques to compute the 3D shape of the weld pool surface [31]. In their method a 7 × 7 dot matrix pattern of laser is projected on the weld pool. The reflection of the dot matrix was observed on the imaging plane. On the basis of the geometry, law of reflection and using an approximation, the slope field of the surface was computed and an estimated weld pool surface is formed as shown in Figure 2-10. Although this simulation work is done only considering the simplified and ideal welding environment, it provides a good research direction for the study in this dissertation.

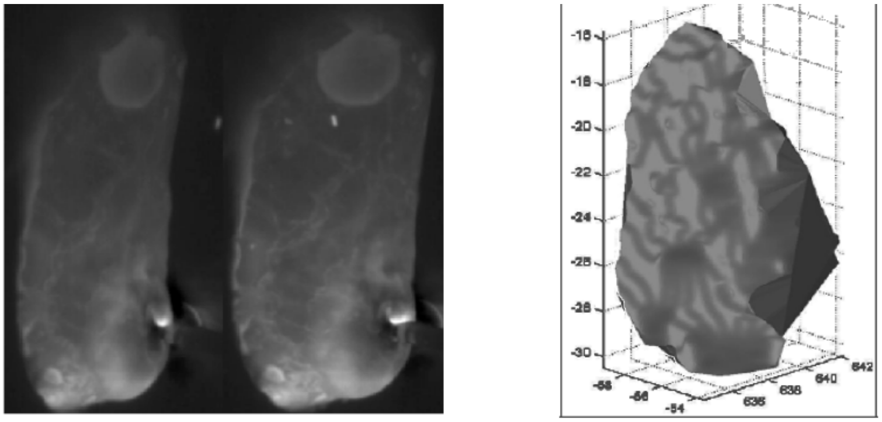

(a) Stereo image pair (b) Rendered weld pool 3D plot

Figure 2-11, Stereovision method to measure 3D weld pool surface [32]

As a computer vision technique, stereovision method was also used to determine the 3D shape of the weld pool. In the experiment two paired cameras have been used to capture images [32]. The process used for welding was pulsed GMAW, and the paired images of the weld pool were captured during the "off" period of the arc. Therefore no external illumination was used. A computer was used to trigger the cameras simultaneously so that the images are concurrent and the cameras are also synchronized with the robotic welder to snap the images when the arc is off. The paired images are rectified using calibration parameters obtained through the stereo calibration procedure. As the weld pool surface was highly patterned in the experiment, an image correlation-type measure was used to match points between the two rectified images. Then by using stereo processing algorithms the weld pool shape is rendered in three dimensions, which can be seen in Figure 2-11. The complication of this method makes it unsuitable for practical application.

Another more practical measurement using biprism technique was conducted by Yoo and Lee at Seoul National University, which use the similar principle of stereo imaging [33]. A stereo system using a single CCD camera fitted with single lens and a biprism in front of it is configured. Figure 2-12 (a) shows the principle of biprism to obtain two virtual images Xl and Xr of a point Xp. In the method clear molten pool images were obtained and weld pool boundaries on the left and right images were also extracted, see Figure 2-12 (b). In order to determine the corresponding points, the intensity-based and filter based matching algorithms were applied [34]. The research is still in progress and the accuracy of the system as mentioned by the authors is reasonable.

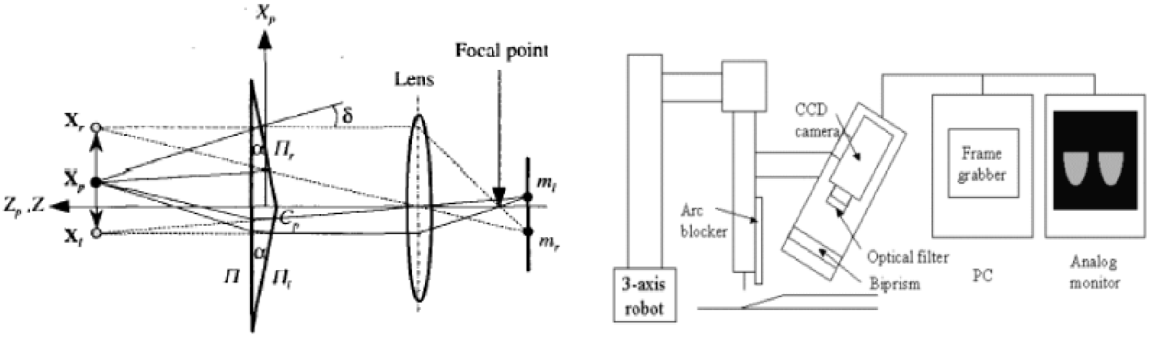

(a) Geometry principle (b) system setup

Figure 2-12, Biprism method [33]

A structured light technique was used by Saeed et al. to determine the 3D profile of the weld pool surface [34]. In the experiment, a laser line is projected onto the weld pool surface from a known position with an angle. And the line is reflected specularly when welding process begins and weld pool is in molten status. The reflected laser beam from the weld pool surface is captured by a calibrated compact CCD sensor. From the acquired images, the profile of the weld pool surface can be extracted using ray-tracing technique and the parameters of the CCD sensor. If the line is projected onto the center of the weld pool, the depth of weld pool can also be extracted. The experiment scheme and results are shown in Figure 2-13 and Figure 2-14 respectively.

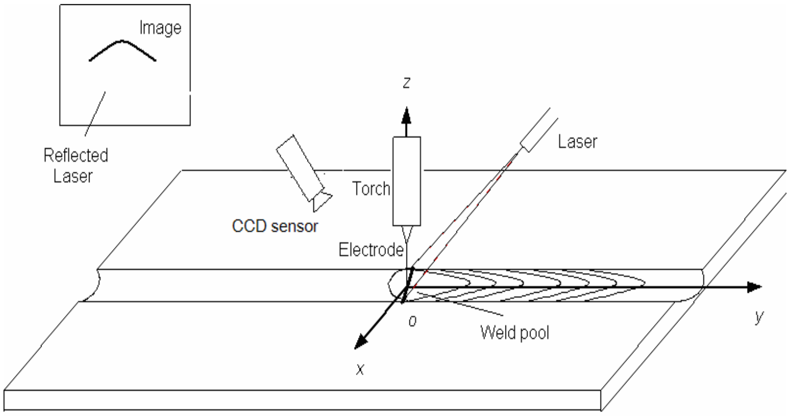

Figure 2-13, Structured light technology used in weld pool observation [34]

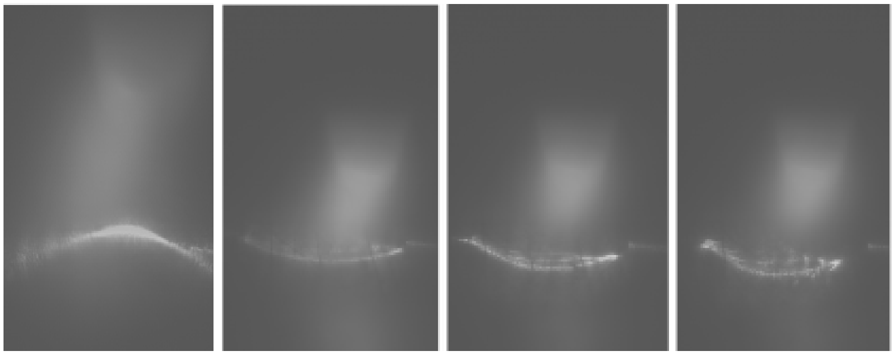

(a) (b) (c) (d)

Figure 2-14, (a) laser reflected from convex weld pool surface, no penetration; (b) Laser reflected from concave weld pool surface, little penetration; (c) welding current increased to make greater penetration; (d) penetration increased with increase of welding current. [34]

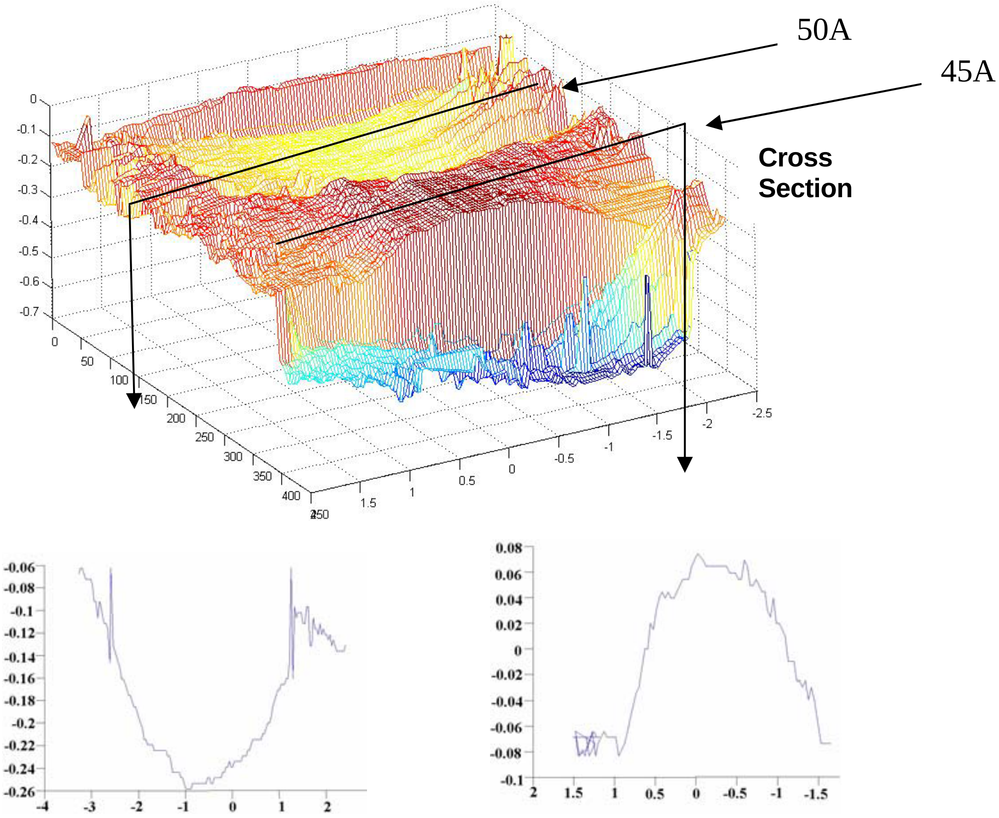

Figure 2-15, Weld pool profiles in an experiment at different currents [34]

In the extended experiments the optimal incident laser angle, the observing angle and other optics' parameters are also determined [34]. The distortion in the laser line distinctively showed the shape of the weld pool. Figure 2-14 shows some of the images captured by the compact sensor. As can be seen from the images, the bright arc above the surface affects the observation seriously, which can not be avoided because of the direct observation using CCD sensor.

In this technique, incorporated use of a calibrated CCD sensor and structured light make it possible to extract the depth of pool from captured images. Figure 2-15 shows weld pool surface profiles from an experiment using stainless steel metal plate of 1.85mm thickness at a speed of 2mm/second and variable current. When the current is increased to 50 amps, penetration is achieved and the weld pool surface depth averages 0.5mm. When the welding current is decreased to 45 amps, the weld pool surface is in partial penetration state and the profile looks like a mountain (due to convex blob shape of weld pool).

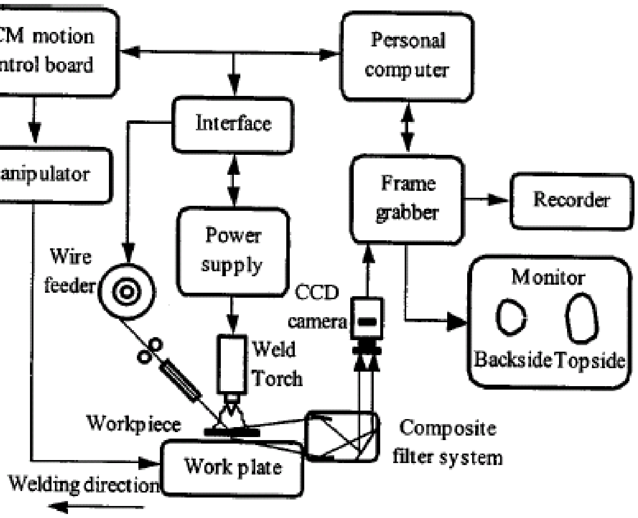

Figure 2-16, Experimental system for monitoring GTAW with wire filler [35]

A vision-based sensing system was developed for pulsed GTAW with wire filler by Zhao et al., which is shown in Figure 2-16 [35]. The experimental system for the pulsed GTAW included a welding power source, a work plate, a cooling water pump, and other auxiliary equipment. The CCD imaging system included a CCD camera, an optical lens systems and a frame grabber. Double-sided weld pools were recorded through a filter system to focus on the same target of the CCD camera. A two-dimensional image processing algorithm was developed to extract the plane shape parameters for convex and concave weld pools. An improved shape from shading (SFS) algorithm using a single image was proposed based on the generalized reflectance map. The algorithm feasibility was verified by reconstructed results from a single synthetic image formed with a known shape object. The weld pool surface height was successfully recovered from a single weld pool image in actual visual sensing conditions.

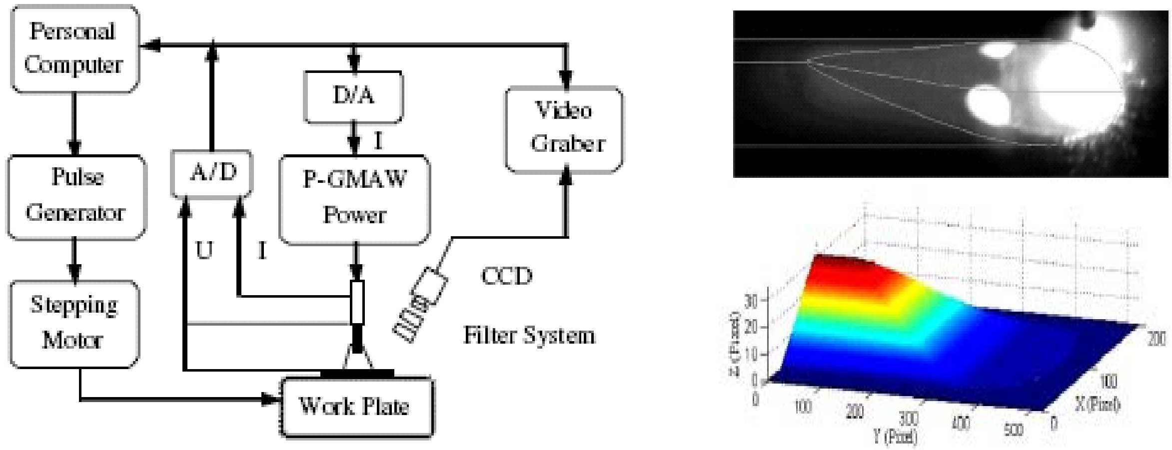

(a) (b)

Figure 2-17, (a) Visual image sensing system of a P-GMAW weld pool, (b) Boundary extraction with a current of 79.5 A and reconstructed 3D mesh from the model [36]

Another sensing system used to reconstruct the three-dimensional P-GMAW (pulsed gas metal arc welding) weld pool shape from the two-dimensional visual image was developed by Guangjun Zhang et al [36]. The system is shown in Figure 2-17 (a). In this approach, a new mathematics model was built to describe the 3D shape of a weld pool and four parameters were used to determine the weld pool shape: the maximum width *W*, the length of the pool tail *L*, the height of the rear of the pool *H* and the projection of the rear angle onto the work piece plane θ_L. As shown in Figure 2-17 (b) the sensing system and image processing algorithms developed were able to extract the model parameters from the 2D weld pool images online and the 3D shape of the weld pool boundary was successfully reconstructed from the 2D image according to the mathematics model. The error analysis shows that the errors mainly come from the visual system (edge detection errors and image distortion etc.) and the asymmetry of the detected object. These errors can be reduced by using ameliorate scaling methods of the visual system and by using binocular vision.

2.3 Other Techniques

Despite the machine vision based sensor, some other techniques are also applied for the observation of weld pool surface, which are introduced from different areas. As far as we know, there is currently no system commercially available which satisfies all the observation requirements of the ideal system. Here some of the techniques are listed: (The range of application and accuracy of control of the systems are discussed [37].)

- X-ray Radiation

An early weld pool observation was conducted at the Ohio State University by Rokhlin and Guu using radiography [38]. The radiation of the received x-ray increases with the depression depth. And the research concluded that the weld penetration and pool depression are closely related and therefore the weld depression was useful for controlling weld penetration. However, the principle behind this method is to measure the material thickness. For full penetration where backside pool surface deformation occurs, the pool surface shape will be difficult to extract.

- Ultrasonic technique

Another way to measure the depth of penetration of a weld pool is to locate the fusion interface between the weld pool and parent metal using ultrasonic waves [39]. The ultrasonic wave is generated by an angled piezoelectric transducer in contact with the surface, as shown in Figure 2-18. As can be seen, the deeper the weld pool, the shorter the total beam path.

For ultrasonic techniques, some conditions should be met in order to make it effective. One of them is that the work piece must have a simple, uniform surface with minimum irregularities to ensure good coupling between the work piece and the transducer. Another thing is since the transducers must track the weld pool, the component vibration or unexpected probe movement must be prevented during the process. The accuracy of control needs to be improved before they can be used for practical applications.

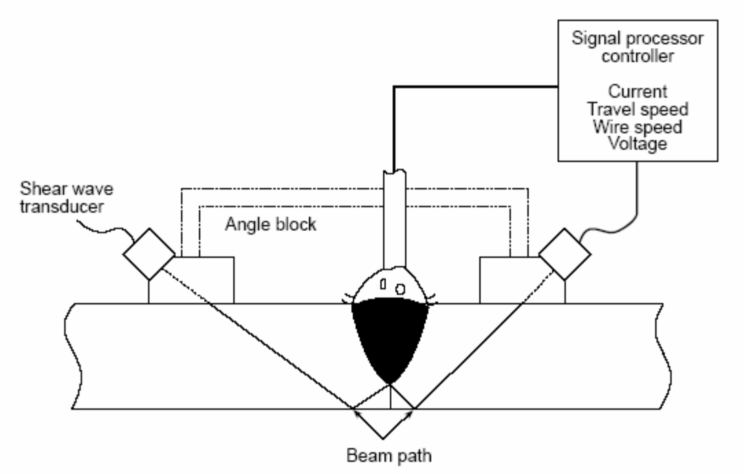

Figure 2-18, Ultrasonic penetration sensing system [39]

- Weld pool sag sensing method

When full penetration is achieved in the welding process, the weld pool surface begins to sag towards the back of the plate because of the arc pressure and gravity. This characteristic is utilized in weld pool sag sensing method [40]. The sag movement can be detected through the increase in arc length, or the change in profile of the weld pool.

However, the magnitude of the movement is very small and this limits the accuracy attainable. The accuracy is reduced by the increase of the work piece thickness, and by weld pool oscillations due to pulsed welding current, addition of filler wire and other unstable factors. Thus weld pool sag sensing method is limited to butt welds in the flat position and requires a highly accurate power source.

- Acoustic emission sensing technique

In the welding process, the stresses due to the thermal gradient of the weld and change of the fused metal volume generate acoustic emissions. The acoustic emissions travel throughout the work piece and can be detected. As penetration changes from partial to full, the frequency spectrum of the acoustic emission changes. In the acoustic emission sensing method [41], a stationary acoustic transducer remote from the weld can be used to measure the emission. Also for laser welding, a non-contact pressure wave sensor is applied.

But the relationship between the acoustic emissions and the weld penetration depth is not fully understood and some micro-structural features may also influence the performance. So acoustic emission monitoring is an instructive trial in this area, which can function independently of welding position, process and joint type.

- Thermal sensing technique

Thermal sensing technique assumes that if the thermal gradient around the weld is constant, then the weld pool penetration is constant. And in this method the temperature may be measured using a contact thermocouple or an infrared pyrometer or a camera [42].

Although thermal sensing is the most widely applied technology in practical use and can also provide seam tracking, these systems are particularly sensitive to variations in the surface condition and the emissivity of the material. The accuracy of camera-based systems is reduced by contributions from the arc light and this can be greatly overcome by the use of filters.

- Weld pool oscillation sensing

In pulsed welding processes, the surface of the pool vibrates. Some researches show that the oscillation frequency is dependent on the weld pool size, and is higher in partial penetration than full penetration. And the oscillation frequency can be further monitored by measuring the fluctuations of either the arc voltage or the arc light reflection. Thus the weld pool oscillation sensing method was proposed [43].

The accuracy of the method is reduced as the travel speed increases and by power source ripple, the presence of dirt, slag or oxide at the back of the weld pool and the addition of filler wire to the weld pool. So weld pool oscillation frequency monitoring by optical systems can only be used for full penetration butt welds, and requires the back surface of the weld to be free of oxide and contamination.

CHAPTER 3

MACHINE VISION SYSTEM DESIGN

The observation of weld pool surface is a key to monitoring the quality of the weld process. In our designed machine vision system, the specular surface property of the weld pool and the coherent and unidirectional property of the structured laser light are explored to observe the weld pool surface indirectly. In this chapter, firstly the proposed machine vision system is presented in detail. Then the observation results by using different projection laser patterns are shown. The clearly captured reflected images verify the accuracy of the approach and provide reliable data for the weld pool reconstruction. At last, the applicability of the designed system is discussed.

3.1 System Design

The proposed machine vision system diagram for sensing weld pool surface is shown in Figure 3-1 [44] [45]. As can be seen, a universal coordinate system (X-Y-Z) is established in the system. The welding process used here is gas tungsten arc welding (GTAW) without filler metal, and the torch is on the Z axis. To observe the three-dimensional shape of a weld pool surface, a 20 mW illumination laser at wavelength of 685nm with variable focus is used to generate structured light pattern (multiple-lines or dot-matrix). Dot-matrix laser pattern is projected in Figure 3-1. The laser lines or dots are projected onto the weld pool surface under the torch electrode in YOZ plane at a certain angle, covering the whole possible weld pool area. During the welding process, the molten weld pool surface is just like a mirror and has good reflection property. In order to intercept the reflected laser pattern from the weld pool surface, an imaging plane is fixed parallel to the OXZ plane at a known distance from the electrode (axis Z). In the meantime, a high-speed camera is used to record the reflected images on the imaging plane. To minimize the influence of the arc, the camera is fitted with a band pass filter of 20 nm bandwidth centered at wavelength of 685nm.

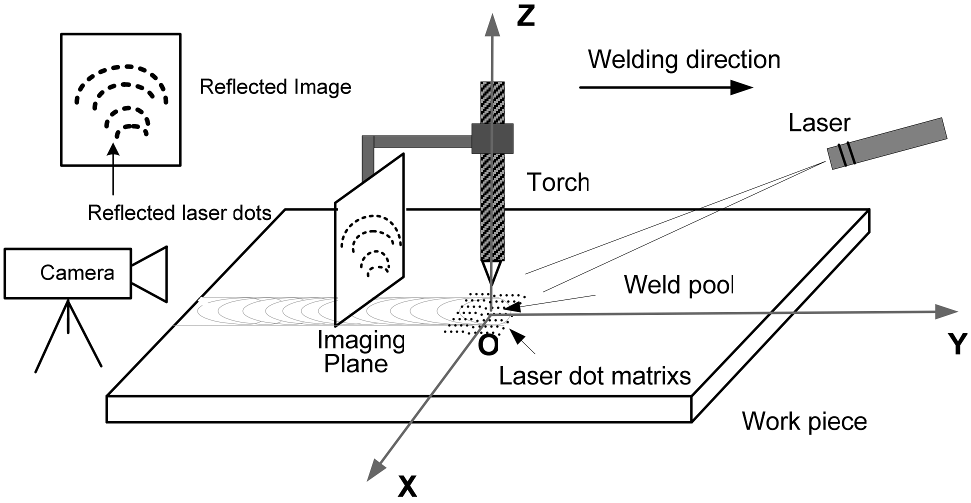

Figure 3-1, System principle diagram

As aforementioned, the bright arc and specular weld pool surface are the two major difficulties for previous vision-based sensing methods discussed in Chapter 2. However from Figure 3-1 it can be seen the reflection of weld pool surface instead of pool surface itself is imaged in the designed system. Thus this indirect approach provides a new solution to observe and measure weld pool surface. There are mainly two advantages in the proposed machine vision measurement system. First one is to change the specular weld pool surface from an observation difficulty to an advantage by exploiting the difference between propagation in illumination laser and arc plasma. The second is the governing law in the system is simply the reflection law and the computation of the weld pool surface can be straightforward.

3.1.1 System components

A typical machine vision system consists of several among the following components [46]:

1. One or more digital or analog camera (black-and-white or color) with suitable optics for acquiring images;
2. Lighting;
3. Camera interface for digitizing images (widely known as a "frame grabber");
4. A processor (often a PC or embedded processor, such as a DSP);

5. Computer software to process images and to detect relevant features;
6. A synchronizing sensor for part detection (often an optical or magnetic sensor) to trigger image acquisition and processing;
7. Input/Output hardware (e.g. digital I/O) or communication links (e.g. network connection or RS-232) to report results;
8. Some form of actuators used to sort or reject defective parts.

In our proposed machine vision system, most of the components listed above are included. The whole system implementation scheme is shown in Figure 3-2. During the welding process, the reflected images captured by the sensing system are sent to a PC to be processed using developed image processing and reconstruction algorithms. After weld pool surface reconstruction, its three-dimensional parameters are extracted and analyzed, which can be further used as a basis to adjust welding current and speed. As can be seen, in fact this is a typical feedback control system, and our research is emphasized on the welding pool surface sensing part and the control part is not included currently. Here some important components of the system are discussed below:

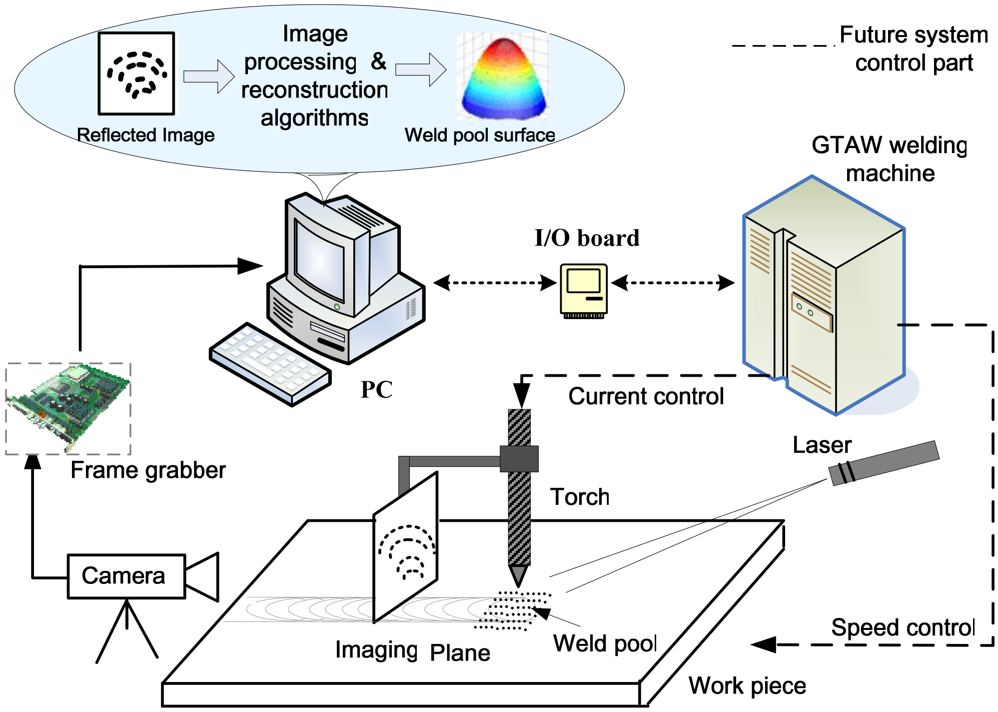

Figure 3-2, System implementation scheme (not include control part)

- Structured light Laser

Structured light is the projection of a light pattern (parallel lines, grid, or more complex shape) at a known angle onto an object. This technique can be very useful for imaging and acquiring dimensional information in machine vision applications. For example, when a sheet-of-light intersects with an object, a bright line of light can be seen on the surface of the object. By viewing this line of light from an angle, the observed distortions in the line can be translated into height variations [47].

In our experimental system, StockerYale's Lasiris™ SNF uniform intensity laser projector is chosen, shown in Figure 3-3. It is especially useful for structured light applications, including machine vision, inspection, and alignment. By using different diffractive lens, different projection patterns can be produced, such as parallel lines, dot matrix, crosshair and single circle etc. In most cases, scanning the object with the light can construct 3D information about the shape of the object. This is the basic principle behind depth perception for 3D machine vision. In our application, there are some special characteristics. The observed object is a dynamic weld pool rather than a solid object, and the reflection of structured light is observed instead of direct viewing the structured light on the object. To measure the three-dimensional weld pool surface more accurately by using reflection law, the dot-matrix projection pattern is preferred in the designed system.

Figure 3-3, Structured light laser [47]

Figure 3-4, High-speed camera

- Imaging plane

The objective of the imaging plane used in the designed system is to intercept the reflected laser light and avoid strong welding arc directly entering camera to disturb observation. The most important is that it provides a plane to show reflected image of projected laser pattern, which can be recorded by a camera.

In Figure 3-1, it can be seen that the laser light reflected from weld pool surface is projected to the back side of the imaging plane and a high-speed camera is used to capture the laser light on its front side. In order to ensure the visibility of the reflected laser pattern from the front side, a piece of 4”-by-4” square glass attached with a grid paper is designed as the imaging plane in the system. The paper on the imaging plane is marked with coordinate axes (system), which can be used to localize the position of the reflected laser light for the precise measurement. Actually there are more reasons of using glass as an imaging plane in addition to its transparency. One is the glass can prevent the paper from burning by the high-temperature of welding arc. The other reason is to reflect away some strong arc from imaging plane.

- High-speed camera

Camera is the core component in the machine vision system. Though most machine vision systems rely on black-and-white cameras, the use of color cameras is becoming more common. It is also increasingly common for machine vision systems to include digital camera equipment for direct connection rather than a camera and separate frame grabber, thus reducing signal degradation. Another kind of camera, called “smart” camera, with built-in embedded processors are capturing an increasing share of the machine vision market. The use of an embedded processor eliminates the need for a frame grabber card and external computer, thus reducing cost and complexity of the system while providing dedicated processing power to each camera.

In the proposed system, an Olympus *i-SPEED* high-speed monochrome camera, known as a kind of smart camera, with a band-pass filter (lens) is placed about 1~2 meters away from the imaging plane to capture the reflected laser light on it, which is shown in Figure 3-4. Since the camera is focused on the imaging plane, the whole 4”-by-4” plane can be clearly recorded by the camera. Since the 20 nm band-pass filter is centered at 685 nm (the wavelength of the laser), the camera can view the reflected laser pattern clearly despite of the existence of strong arc, whose spectrum covers widely. The speed of camera ranges from 60 to 33,000 frames per second. Thus the minimal changes of reflected images with a short period can still be captured by it, which is very important to analyze the status change of the weld pool surface and to realize online quality control.

- GTAW welding machine

Gas tungsten arc welding (GTAW) commonly known as tungsten inert gas (TIG) welding is an arc welding process that uses a nonconsumable tungsten electrode to produce the weld [48], shown in Figure 3-5. The weld area is protected from atmospheric contamination by a shielding gas and a filler metal is normally used. GTAW is often used to produce high-quality weld because of its capability in precision control of the fusion process. Here GTAW is used as the test welding process for the designed observation system, and there is no filler metal used. In our system, *PULSE*^{TM} current-constant welding machine is used and the welding current can be adjusted by changing the input control voltage.

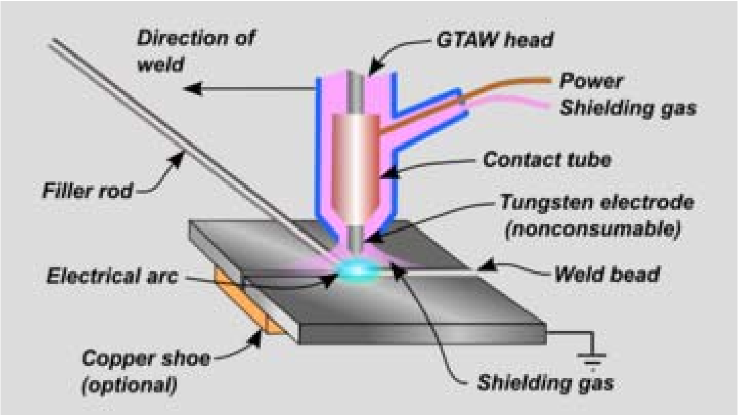

Figure 3-5, General GTAW weld area [48] (no filler rod used in our system)

- PC (and software)

In a typical machine vision system, the camera's image is captured by the frame grabber, which is a digitizing device that converts the output of the camera to digital format and places the image in computer memory so that it may be processed by the machine vision software. The software will typically take several steps to process an image. Often the image is first manipulated to reduce noise or to convert many shades of gray to a simple combination of black and white (binarization). Following the initial simplification, the software will count, measure, and/or identify objects, dimensions, defects or other features in the image. As a final step, the software passes or fails the part according to programmed criteria. In our system, MATLAB programming language with Imaging Processing Toolbox is used to process the captured images and developed corresponding reconstruction algorithm is applied to rebuild the weld pool surface, which can be seen in Figure 3-2.

3.1.2 System parameters

Once the proposed system diagram is finished and components are selected, the real experimental system is set up accordingly. Figure 3-6 shows the established real experimental system (the camera is not included). When configuring the experiments, some of the important system parameters should be decided carefully and jointly since they may directly affect the observation results. In addition to the welding parameters, such as current and speed, some important system (position) parameters are discussed here. They are:

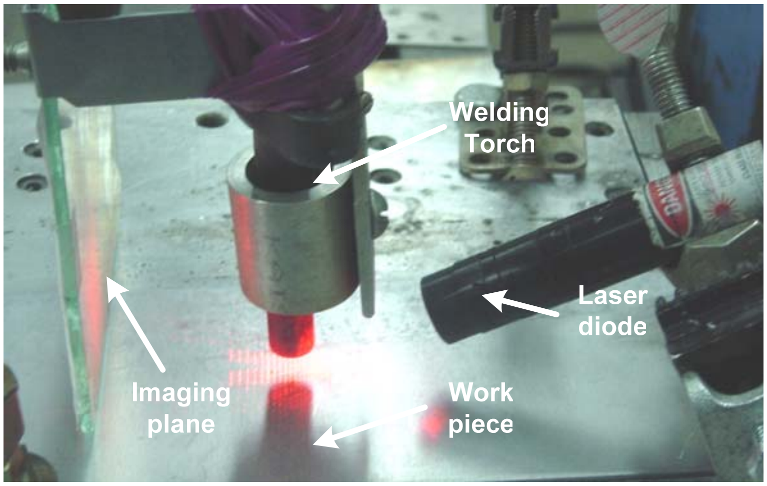

Figure 3-6, Experimental system setup (camera is not included)

- Laser position and projection angle

The position and projection angle of laser diode determined the positions of projected laser pattern (dot-matrix or multiple-line) and the direction of incident rays. Depending on the selected diffractive lens for the laser, different parameters are used to describe the produced pattern. For the multiple-line pattern lens, “Fan Angle” presents the spread angle of the laser to form the lines, which is shown in Figure 3-7, and “Interline Angle” is the angle between two adjacent lines. For the dot-matrix pattern lens, only “Inter-beam Angle” is used to present the angle between two adjacent dots. Combining the angle parameters with the working distance of the laser diode, the scale of the projected pattern can be decided. In our sensing system, the chosen distance of the laser to the work piece should make the projected pattern cover the whole possible area of weld pool (about 8mm*10mm area) and the distance between the lines/dots should be very small (about 0.5mm) in order to measure the weld pool surface precisely.

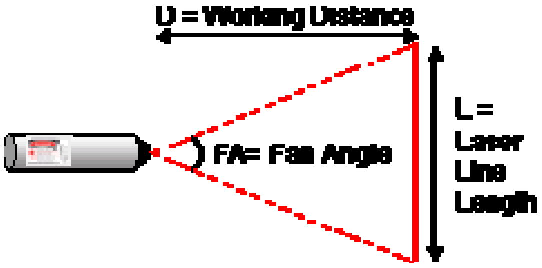

Figure 3-7, Fan angle of the laser diode (for multiple-line pattern) [47]

The laser projection angle is another important parameter, which may affect the reflection direction of the light. If the angle is too large, the reflected lights may be blocked by the torch; if the angle is too small, some of the reflected lights will not be projected onto the imaging plane. Based on the knowledge of small deformation in GTA weld pool and the previous experimental experiences [49], it is found that around 30 degree is good value for the laser incident angle in the experiments. According to above requirements, the laser position and projection angle can be configured. The propose laser calibration method [49] can also be used to precisely measure these parameters, which can be seen in Appendix I.

- Torch position

The position of torch is along the Z axis of the coordinate system as shown in Figure 3-1. The distance between tungsten tip and work piece is about 3~5 mm, which makes less reflected light blocked and makes stable welding arc possible. In order to make system configuration and measurement easy, the center of the projected patterns (center point for dot-matrix pattern and center line for multiple-line pattern) should be projected just below the torch and in the origin of the universal coordinate system.

- Welding direction

Generally welding direction refers to the moving direction of the welding torch during the welding process. In our designed experimental system, the positions of torch, imaging plane and laser diode is unchanged and only the welding platform (work piece) is moving at a desired speed to realize welding process. Thus the moving direction of the platform is opposite to the welding direction. In the established universal coordinate system in Figure 3-1, the welding direction can be along either the positive (shown in figure) or the negative direction of the Y axis. But different welding directions may affect the observation results of the reflected laser pattern.

Figure 3-8 shows the practical situations with different welding directions in the experiments. As can be seen, the head of the formed weld pool is always on the forward side along the welding direction, and its distance to the tungsten electrode is obvious smaller than that of the weld pool tail. Suppose there are four incident rays (A, B, C and D) are projected to the weld pool surface. In Figure 3-8 (a), the projected rays within weld pool surface (A, B and C) can be successfully reflected onto the imaging plane. But in Figure 3-8 (b), the reflection of the incident ray D from the weld pool surface may be blocked by the torch because D is farther to the torch and the height of the tungsten electrode is limited. Thus the welding direction is preferred along the positive direction of Y axis in the designed system as shown in Figure 3-8 (a). Just as discussed above, the 3~5 mm height of tungsten electrode and 30 degree laser projection angle will make the incident ray A that is projected to the head of the weld pool not blocked by the torch. The different results can also be seen in section 3.2.2.

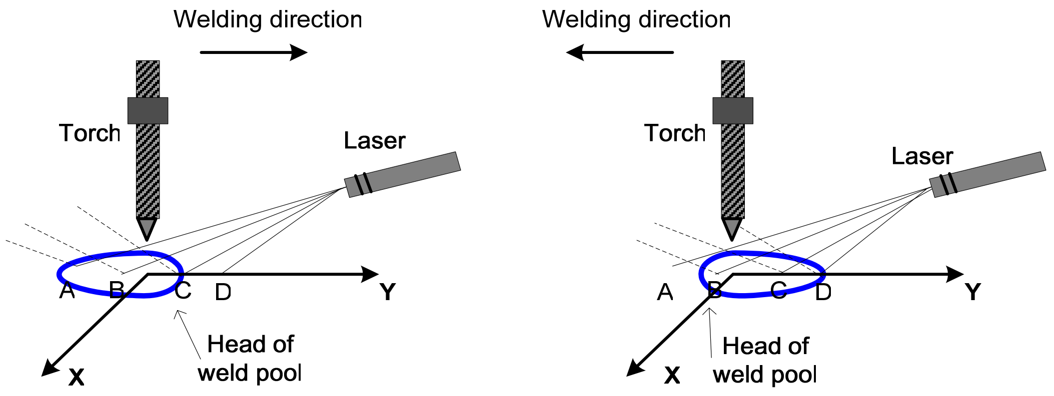

(a) Along positive direction of Y axis (b) Along negative direction of Y axis

Figure 3-8, Different welding directions illustration

- Imaging Plane Position

The distance between the imaging plane and the torch (Z axis) is directly related to the quality of the captured image, such as the size of the reflected laser pattern and the arc intensity in the image (although band-pass filter is used in the camera, it still will impact the visual effect). The nearer the imaging plane is placed, the smaller the reflected image is and the stronger the arc intensity is, and vice versa. Meanwhile the size of the imaging plane (4”X4”) also affects the decision of the imaging plane position. Experimental results shown 45~60 mm is a good range for the distance of imaging plane in the proposed system. Of course, this is also related to the used welding current, for example 65~75 A in our system. The placement of imaging plane should be adjusted in the experiments to make the captured image clear.

- Camera Position and setup

The high-speed camera fitted with 685nm ± 10nm band-pass filter is used in the proposed system in order to capture clear reflected image on the imaging plane. In the experiment the camera should be focused on the imaging plane and the distance between camera and imaging plane is set to make the whole imaging plane just included in the captured image, which is about 1~2 m in practical experiments because of the big size of the high-speed camera. More compact camera can be used if the system is applied in industry.

According to different requirement of recording speed, the frame rate of the camera can be adjusted. Generally high frame rate is preferred for observation of dynamic weld pool surface, but it will also cause the reflected laser pattern eliminated from the image due to the used low-power illumination laser. In our experiments, the frame rate of the high-speed camera is selected in a range from 60 frames per second to 200 fames per second, and the aperture needs to be adjusted accordingly.

3.2 Observation Results

Different structured light patterns (multiple-line and dot-matrix) are tested in the designed machine vision sensing system. For multiple-line pattern experiment, a commercial available 5-line pattern (model SNF-505L(0.23)-685-20-5) is used. For dot-matrix projection pattern, a 19-by-19 dot-matrix pattern (model SNF-519X(0.77)-685-20) is selected since it can cover the whole weld pool surface and the lack of its center point can be easily recognized in the reflected image for locating the dots. The procedures of the experiment and the observation results are presented and discussed. As can be seen, the high-quality reflected images captured by the camera verified the success of this new sensing system.

3.2.1 Multiple-line pattern

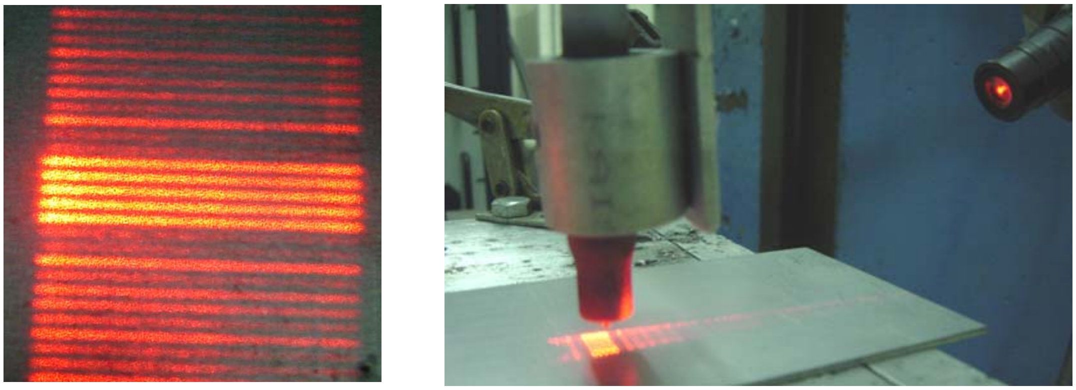

Figure 3-9, Multiple-line pattern and its application in the system

A multiple-line structured light pattern (five-line) is used in the sensing system, which is shown in Figure 3-9. In the figure, some more lines with less intensity appear beside the five bright lines, which are the diffraction fringes produced by the laser diode. The proposed machine vision system has been shown in Figure 3-1. A 20 mW illumination laser at a wavelength of 685 nm with variable focus is used to generate the multiple lines. The fan angle of the laser is 5 degree and the interline angle is 0.23 degree. In one of the experiments, 5-line laser pattern is projected on the weld pool surface under the torch electrode at 27 degree in the OYZ plane. The distance from the laser to the weld pool is approximately 90 mm. An imaging plane is parallel to the OXZ plane at a known distance of 53.6 mm from the axis of the electrode (i.e., axis Z). To minimize the influence of the arc, the camera observes the imaging plane with a band-pass filter of band width 20 nm centered at a wavelength of 685 nm. The welding direction is the negative direction of Y axis, which is opposite direction shown in Figure 3-1. The detailed experiment instructions are attached in Appendix II.

1. Observation results

Although the illumination laser is continuous and has low power (20 mW) in comparison with that of the arc, clear images as shown in Figure 3-10 are obtained in the presence of bright arcs [44]. This is because the system takes advantage of the difference between propagation in the illumination laser and arc plasma. In fact, the arc light intensity decreases with the square of the distance. However due to the coherent and unidirectional property of the laser light waves, the laser’s travel direction remains unchanged and its intensity or power loss over the distance traveled by the laser light is insignificant in comparison with that of the arc. In addition, the specular surface of the weld pool reflects nearly all the intensity of the projected illumination laser lines. Hence, if the imaging plane is placed reasonably far from the torch, the intensity of the laser light falling on it will be much stronger than that of the arc light.

Figure 3-10 shows the reflected images using different work piece with dissimilar reflective characteristic. The clear image in Figure 3-10 (a) was acquired when a piece of mild steel was used, which has less reflection property.

As can be seen, only the distorted laser lines reflected from specular weld pool are shown on it. This kind of image is simple and intuitive, so it is suitable for the weld pool observation in our research.

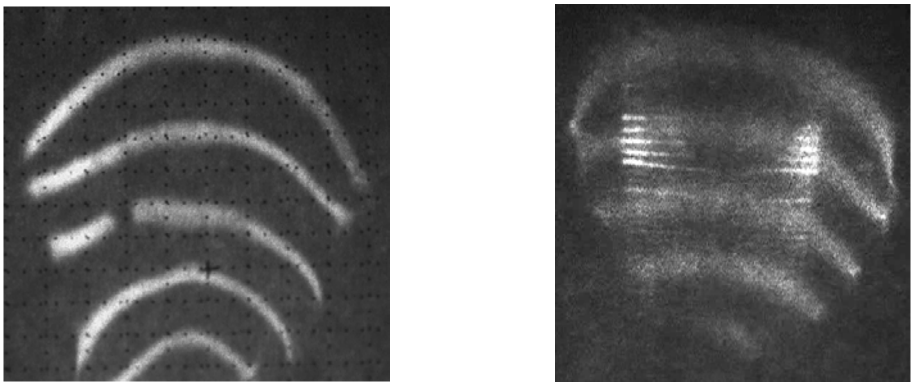

(a) Result using mild steel plate (b) Result using stainless steel plate

Figure 3-10, Reflected images of multiple-line pattern

In addition, the result using a stainless steel plate is presented in Figure 3-10 (b). Except for the deformed lines reflected from the weld pool surface, there are more straight reflected lines in the middle of the image, which are reflected from outside of weld pool due to the high reflective characteristic of the work piece. Compared with Figure 3-10 (a), this overlapped image is more complicated and less clear. But this image provides more information about the weld pool. From the image, we can not only get the information about the 3D shape of the weld pool, but also acquire its 2D shape from the laser lines since they are straightly reflected from outside of the weld pool. This finding is interesting and deserves further study.

2. Observation of welding process

In one of the experiments [45], a 2 mm thick mild steel sheet was used as the work piece. The welding current was kept at 65 A and the welding speed was changed from 2 mm/s to 3 mm/s at point C in Figure 3-11, which shows the welded work piece. From the captured reflected images, the status of the weld pool surface can be analyzed according to different phases during the welding process.

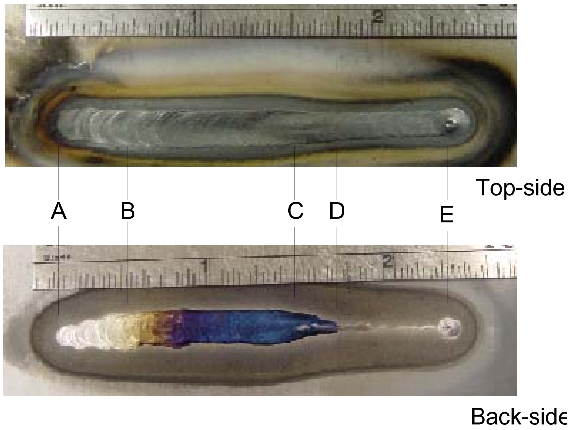

Figure 3-11, Welded work piece

In the beginning segment of the experiment from point A to point B, the weld pool grows to a state of stable full penetration. While the image at point A is a blurred plane without any lines, the image acquired at point B is shown as the first image in Figure 3-12. In the segment B to C in Figure 3-11, the welding process is at a steady state of full penetration at a welding speed 2 mm/s. The patterns of the reflected lines vary only slightly (due to the oscillation of the weld pool surface) as can be seen in Figure 3-12 where the first, second and third images are acquired at point B, in between points B and C, and point C respectively.

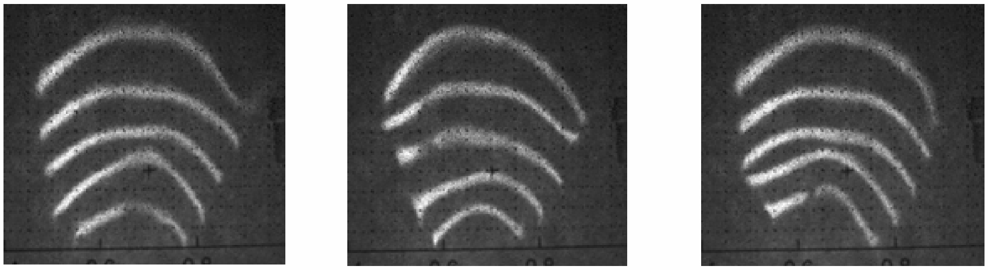

Figure 3-12, Reflected images in Segment BC

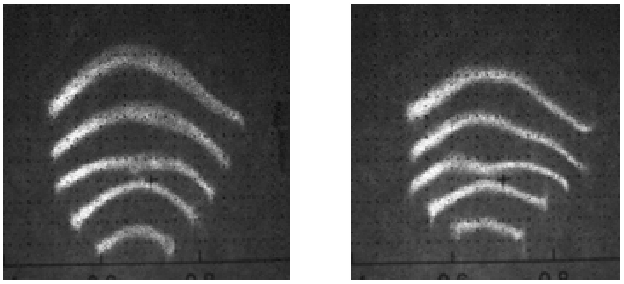

Figure 3-13, Reflected images in Segment CD

After the welding speed is increased to 3 mm/s at point C, the area of the weld pool on the top side (the side aimed at by the torch) of the work piece decreases and the surface changes its shape and becomes shallower or changes from being concave towards being convex. The depth of the weld pool also reduces because of the reduced heat input so that the backside width of the weld pool reduces in segment CD and eventually becomes zero at point D (i.e., the penetration state changes from full to partial or the depth of the weld pool reduces to less than the thickness of the work piece). Hence, segment CD is a transition period. Figure 3-13 shows two images acquired during this transition period. As can be seen, the images during this period become smaller due to the reduced area of the specular (reflection) weld pool surface (see the top side of the welded work piece). However, the surface of the weld pool is also in transition, the decrease of the image size is thus not quite significant as is the area of the weld pool surface.

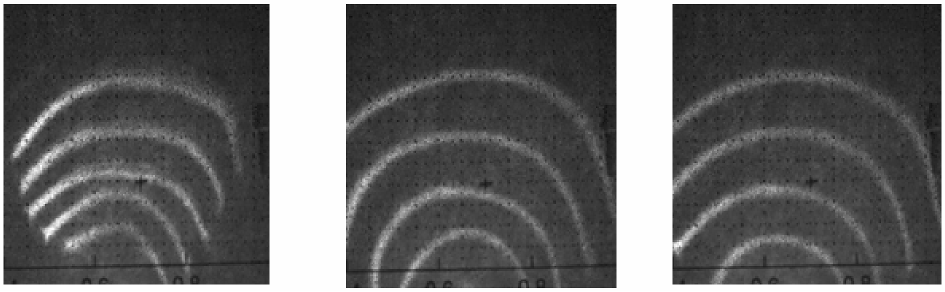

Figure 3-14, Reflected images in Segment DE

At point D through to the end of the weld, the penetration is partial and the weld pool surface on the top side becomes significantly convex. The first image shown in Figure 3-14 was acquired at point D and the other two images were acquired during segment DE. As can be seen, although the area of the specular (reflection) surface becomes smaller, the images are larger than those acquired during the full penetration periods in Figure 3-12. The change of the weld pool surface from being concave or insignificantly convex to being significantly convex is responsible for this phenomenon because the weld pool surface must be convex when the penetration is partial and the weld pool surface must be concave if a significant full penetration is established or the convex degree is insignificant if the full penetration is not significant. In addition, it can also be seen in Figure 3-14 that the number of the laser lines reduces from five to four. This indicates that the size of the weld pool has been reduced and less laser lines are projected to and reflected from the specular weld pool surface.

3.2.2 Dot-matrix pattern

As can be seen above, clear reflected images can be achieved by using multiple-line pattern of structured light, and the images contain 3D information of the weld pool surface. But these images with reflected lines are difficult to be used to reconstruct the weld pool surface based on reflection law. According to the knowledge of optics, the reflection of light ray is easy to be tracked. Thus dot rays are needed for the proposed system to be projected onto the weld pool.

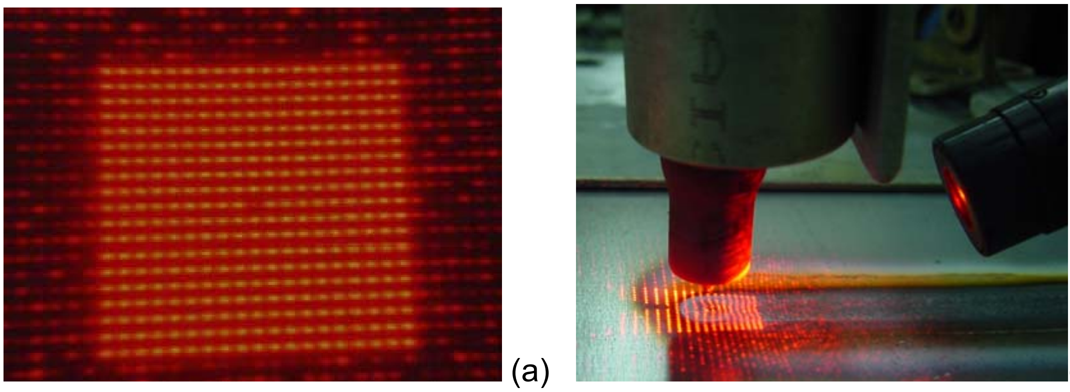
(a) (b)

Figure 3-15, (a) Dot-matrix pattern and (b) its application in the experiment

In this step, many methods were tested in order to produce appropriate dot matrix laser source, such as using printed transparency with vertical lines to blocking multiple-line pattern and putting diffractive grating in front of dot laser. However some problems were encountered by using these approaches. At last, considering the needed dimension of dot matrix and the safe distance between laser diode and tungsten electrode, a SNF laser with a 19-by-19 dot matrix pattern lens is used for our application, whose projection area can cover the whole weld pool area with reasonable close distance between dots (about 0.5-1 mm with 50 mm projection distance). Its inter-beam angle is 0.77 degree. In

Figure 3-15 (a), it can be seen that the center point (at 10th row and 10th column) in the dot matrix is made absent (or can be thought much less bright), which can be used to locate the position of multiple dots as a reference (dot). In the experiment, the dot matrix is projected to the work piece at a certain angle covering the whole possible area of the weld pool surface, just as shown in Figure 3-15 (b).

1. Observation results

In an experiment using dot-matrix projection pattern, 2 mm thick mild steel sheet is used as the work piece. The welding current is kept at 70 Amp, and the welding speed is about 2 mm/s. The 19-by-19 laser dot matrix is projected on the weld pool under the torch electrode at 30 degree in the OYZ plane. The distance from the laser to the weld pool is approximately 40 mm. An imaging plane is parallel to the OXZ plane at a known distance of 49 mm from the axis of the electrode (i.e., axis Z). The distance between torch tip and the work piece is about 3mm. In this experiment, the welding direction is also the negative direction of Y axis, which is opposite to the direction shown in Figure 3-1.

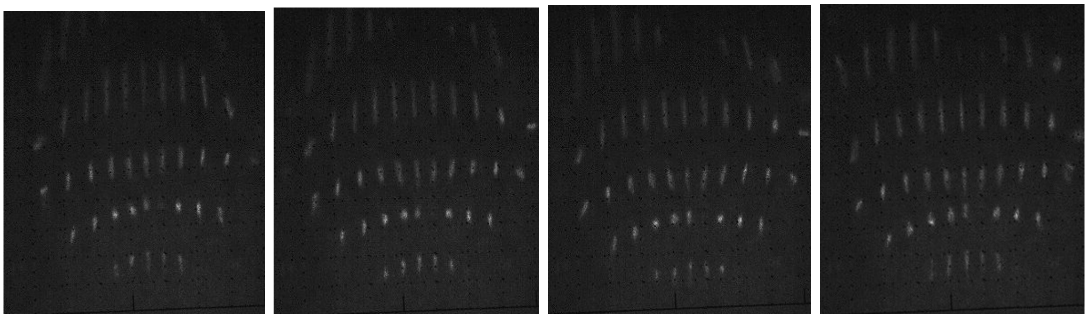

Figure 3-16, Acquired reflected images by using dot-matrix pattern

In Figure 3-16, four images acquired by the camera during the stable period of the experiment are shown. Although the contrast of the images is a little low, the reflected dots can still be seen, which were distorted by the specular weld pool surface. In these images, some reflected dots on the upper row are blocked and the positions of the reflected laser dots change a little, which shows the variation behavior of the weld pool surface under the same welding condition.

Another experiment using 19-by-19 dot matrix is conducted by changing the welding direction to positive Y axis direction. During the experiment, a sheet of 2 mm thick mild steel is used as the work piece and the welding current is kept on 75 A with the constant welding speed of 3 mm per second. The distance between the torch and imaging plane is 50 mm and the projection angle of laser diode is about 31 degree. Figure 3-17 shows four captured images. As can be seen, under nearly the same condition more rows and more dots are reflected onto the imaging plane compared with the results shown in Figure 3-16. The possible reason has been discussed in section 3.1.2. These images are more useful for the accurate reconstruction of weld pool surface, which will be further discussed in Chapter 6 and 7.

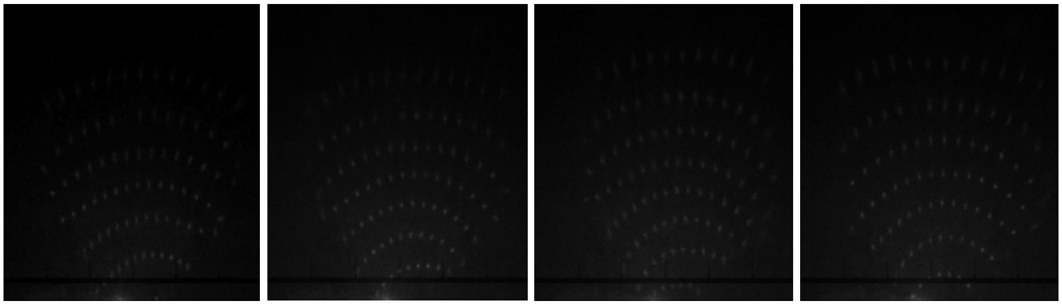

Figure 3-17, Acquired reflected images by change welding direction

2. Center reference point location

In Figure 3-16 and Figure 3-17, the corresponding position of the center reference point can also be easily, and it lies in the 2nd (5th) row from bottom up and between the 5th (5th) and 6th (6th) dots respectively. In Figure 3-18, the corresponding positions of the reference point are shown. With the information of reference point, it can be known which row and column the other dots around the reference dot in the image is reflected from which point in the projected dot matrix. Thus the corresponding relationships between projected dots and the reflected dots on the imaging plane are established, which can be used for reconstructing the weld pool surface.

From above observation results, it can be seen that reflected images of the weld pool surface with the reflection pattern can be acquired using the proposed approach with a low power illumination laser. The clearness of the images assures that they can be processed to accurately extract the laser lines/dots shaped by the specular weld pool surface and thus be used to accurately compute the weld pool surface. The novelty of the proposed approach which takes advantage of the specular surface and the difference between propagation in an illumination laser and arc plasma is responsible for achieving such quality of clear images.

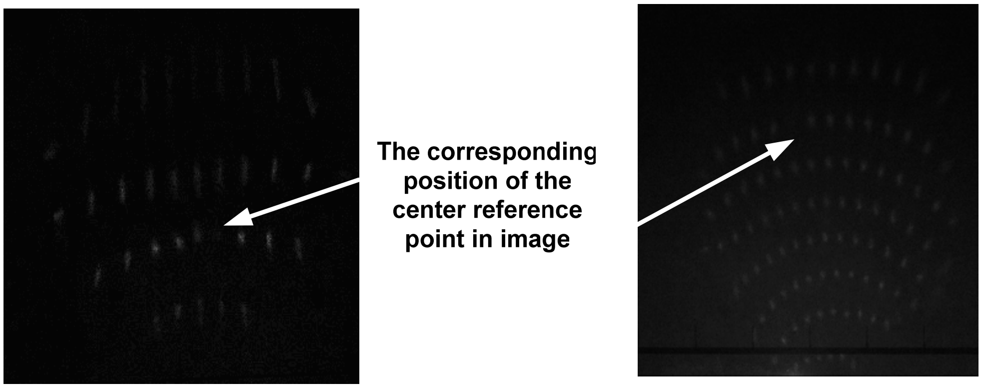

Figure 3-18, Corresponding positions of reference point in the images

However there are also some interferential factors existed in the experiments, which affect the quality of acquired reflected images. The unstable shielding gas and unbalanced electromagnetic field vibrate the arc and make weld pool surface unstable. During practical welding, impurities or oxides existing on the pool surface also block light reflection and make the reflected images unstable [50]. In order to ensure reflected image quality, these bad factors should be minimized, even eliminated.

3.3 System applicability

The designed machine vision system uses the specular surface to overcome the difficulty caused by the bright arc through exploiting the difference between propagation in an illumination laser and arc plasma. The solution of the major difficulties provides an effective method to observe and measure the specular weld surface with a low power illumination laser. This approach is also applicable to other specular surface reconstruction problem, which explains the meaning of the dissertation title "Machine Vision Recognition of Specular Surface for Gas Tungsten Weld Pool". Thus this method may also be suitable for other welding processes, such as gas metal arc welding (GMAW) and laser welding, as long as the reflection of the surface can be captured.

Some additional experiments have been done in order to test the system applicability for gas metal arc welding (GMAW) process. The system diagram, shown in Figure 3-19, is nearly the same as the one for GTAW process. But still there are some differences:

- A one-line laser pattern is used in this experiment in order to make the energy of the 20 mw laser diode is concentrated;
- The distance between torch and imaging plane is shorter. It is about 20 mm rather than 50 mm used in GTAW experiments;
- The projection angle is much larger, for example 70 degree. Since the slope of GMAW weld pool is larger, larger incident angle can make the reflected laser light projected on imaging plane at a reasonable angle.

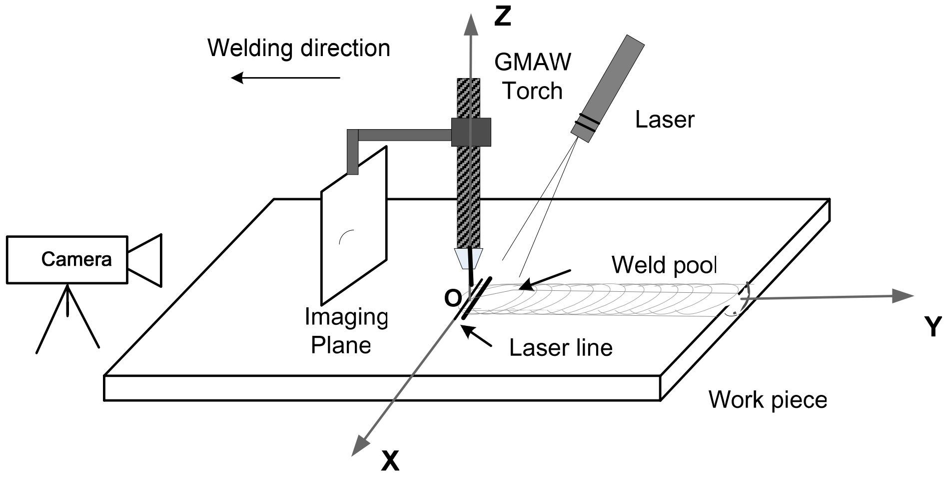

Figure 3-19, System diagram applied in GMAW

In the experiment, pulsed GMAW process is used and the average welding current is 100 A and the welding speed is about 5 mm per second. For the high-speed camera, the frame rate is set to 1500 frames per second and the aperture is 4 (maximum). The work piece is a mild steel plate. Some captured reflected images at pulse 'off' and 'on' periods are shown in Figure 3-20. As can be seen, when pulse is on the image is dominated by the arc light and when it is off the fluctuated laser light reflected from molten weld pool surface is shown. This proved the existence of reflection from weld pool surface in GMAW, and it is possible that the proposed machine vision system is also applicable for GMAW process.

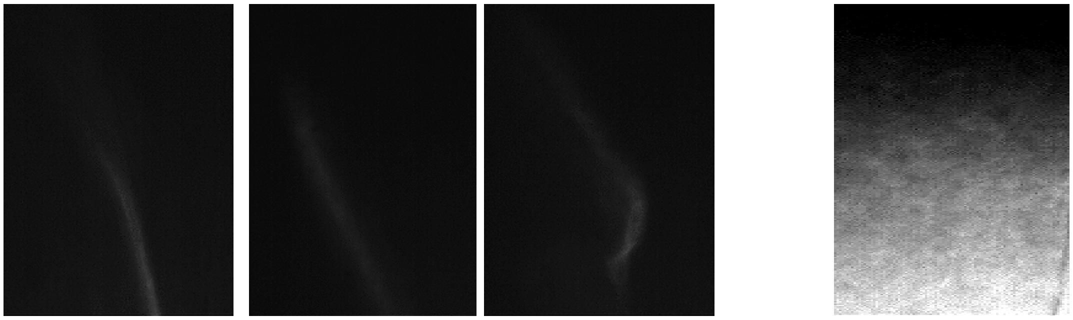

(a). Images in pulse ‘off’ periods (b) Image in pulse ‘on’ period

Figure 3-20, Captured reflected images in GMAW experiment

There are some possible ways to improve the observation experiment of GMAW weld pool surface:

- High-power laser diode should be used in order to depress high intensity of welding arc in GMAW process.
- Change the ordinary glass to high-temperature resistant glass for the imaging plane because of its short distance to the welding arc.
- Increase frame rate of the high-speed camera so as to get more stable reflection images.

3.4 Summary

Observation and measurement of a weld pool surface is a key towards the development of next generation intelligent welding machines. However, the bright arc radiation and the specular surface complicate the task. In this chapter, a new machine vision system is proposed to turn the difficulty of the specular surface into an advantage. The governing law is simply the reflection law. Experimental results verified that clear images of the weld pool surface can be acquired using the proposed approach with a low power illumination laser. The clearness of the images assures that they can be processed to accurately extract the laser pattern shaped by the specular weld pool surface and thus be used to accurately compute the weld pool surface. The novelty of the proposed approach which takes advantage of the specular surface and the difference between propagation in an illumination laser and arc plasma is responsible for achieving such quality of clear images. Moreover, more experiments have been done to test the system applicability, especially for GMAW process.

CHAPTER 4

SYSTEM MODELING AND SIMULATION

The description of the proposed machine vision system in Chapter 3 gives us a practical image about the system implementation and experimental results. To better understand the designed system and the principles behind it, system modeling and simulation are thus conducted in this chapter. In the modeling section, the model for specular reflection and the established three coordinate systems are discussed. In simulation section, the correspondence simulations are done in order to investigate the relationships between projected and reflected laser rays. Here the dot-matrix laser pattern is chosen for our study.

4.1 System Modeling

4.1.1 Specular reflection

Weld pool surface reflection plays an important role in the proposed sensing system. In physics, reflection is the change in direction of a wave front at an interface between two dissimilar media so that the wave front returns into the medium from which it originated. Common examples include the reflection of light, sound and water waves. Reflection of light may be specular (mirror-like) or diffuse (not retaining the image, only the energy) depending on the nature of the interface.

When light strikes a rough or granular surface, it bounces off in all directions due to the microscopic irregularities of the interface. This is called diffuse reflection, which is shown in Figure 4-1 (a). Specular reflection is the perfect, mirror-like reflection of light from a surface, in which light from a single incoming direction is reflected into a single outgoing direction. Such behavior is described by the reflection law, which states that the direction of outgoing reflected light and the direction of incoming light make the same angle with respect to the surface normal. The reflection law is commonly stated as $\theta_i = \theta_r$, just as shown in Figure

4-1 (b). In the figure, PO is the incident ray and the OQ is the reflected ray. During the welding process, the molten weld pool surface is just like a mirror and the specular reflection happens when incident laser rays are projected onto it.

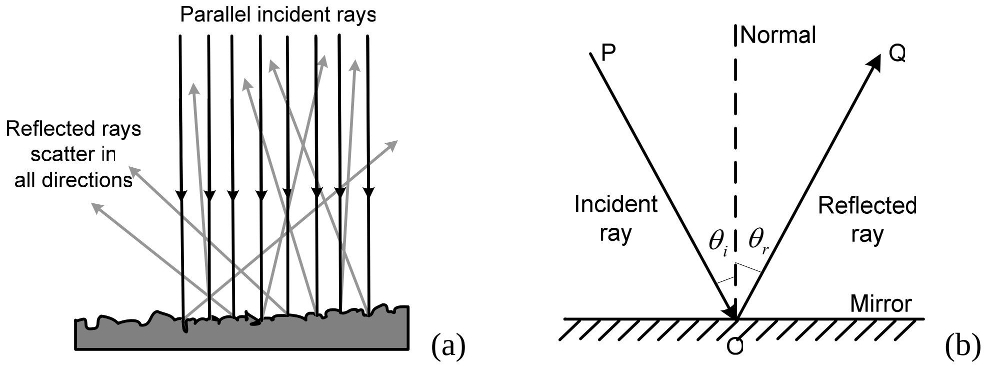

Figure 4-1, Different reflections (a) Diffuse reflection (b) Specular reflection

Even when a surface exhibits only specular reflection with no diffuse reflection, not all of the light is necessarily reflected. Some of the light may be absorbed by the materials or transmitted through the surface. For most interfaces between materials, the fraction of the light that is reflected increases with increasing angle of incidence θ_i. If the light is propagating in a material with a higher index of refraction than the material whose surface it strikes, then total internal reflection may occur, which is called total reflection.

In our proposed system, specular reflection of the incident laser rays happens on the weld pool surface. In order to establish specular reflection model in the system, the geometrical representation of objects, such as 3D lines and surfaces, and the realization of reflection law should be formalized. Here some expressions (models) are discussed as below: (the dot-matrix pattern is used)

- Incident line

For the projected dot matrix rays, the equation of the incident laser ray at row i and column j can be described by its direction vector and the coordinates of the laser diode point, which is shown is Eq.4-1.

$$\begin{cases} x_{i,j} = x_0 + px_{i,j} \cdot t \\ y_{i,j} = y_0 + py_{i,j} \cdot t \\ z_{i,j} = z_0 + pz_{i,j} \cdot t \end{cases} \qquad \text{……. (Eq.4-1)}$$

where (x_0, y_0, z_0) presents the universal coordinates of the laser diode and $(px_{i,j}, py_{i,j}, pz_{i,j})$ is the direction vector of the laser beam at row i and column j. The parameter t is an independent variable.

Since the inter-beam angle (the angle between adjacent laser rays) of the laser diode with dot-matrix pattern is known, the direction vectors of laser beam can be easily derived. At the same time, the position of the laser diode can also be decided by the method of laser calibration, which is shown in Appendix I.

- Normal line

Suppose S is a surface with the equation $z = f(x, y)$ (or $F(x, y, z) = z - f(x, y) = 0$) and $P = (x_p, y_{p,} z_p)$ is a point on S. Then the direction of normal line in point P can be expressed as below:

$$\begin{cases} F_x(x_p, y_p, z_p) = f_x(x_p, y_p) \\ F_y(x_p, y_p, z_p) = f_y(x_p, y_p) \\ F_z(x_p, y_p, z_p) = -1 \end{cases} \quad \ldots\ldots. \text{(Eq.4-2)}$$

With this direction vector and the position of P point, the equation of the normal line can also be expressed as Eq.4-1. If the surface equation is not known and the incident line and its reflected line are known, the normal line is the angle bisector of the angle formed by incident and reflected lines and it can thus be computed.

- Reflected line

If the normal line (or the surface) and the incident ray are known, the reflected line can be calculated based on the reflection law, which states that the incident angle of a light beam is equal to the angle of reflection. Figure 4-2 illustrates the method. Here incident line AO and normal OC are known, and the reflected line OB is unknown.

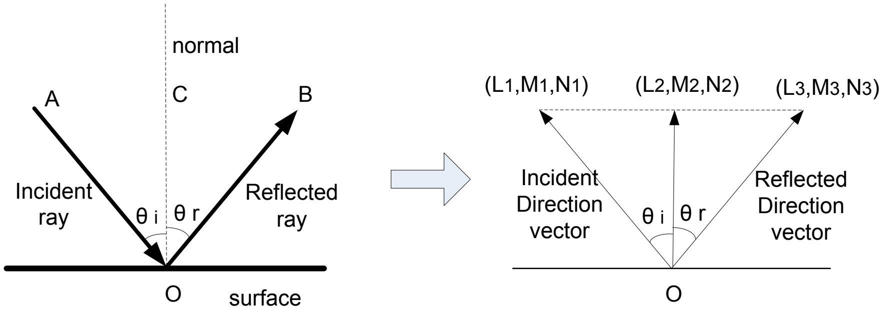

Figure 4-2, Illustration of reflected line computation

Based on the knowledge of geometry, it is know if length of segment AO is equal to the length of OB, then the center point of AB is on the normal. Suppose the direction vector (L_1, M_1, N_1) of incident ray OA and the direction vector (L_3, M_3, N_3) of reflected ray OB are both normalized and their lengths are equal to 1, and the direction vector of normal line OC is (L_2, M_2, N_2).

$$\begin{cases} L_2 \cdot k = (L_1 + L_3)/2 \\ M_2 \cdot k = (M_1 + M_3)/2 \\ N_2 \cdot k = (N_1 + N_3)/2 \\ \sqrt{L_3^{\ 2} + M_3^{\ 2} + N_3^{\ 2}} = 1 \end{cases} \quad \text{……. (Eq.4-3)}$$

where k is a positive variable and (L_2*k, N_2*k, M_2*k) presents the position of point C. Solving above equations gives the direction of the reflected line:

$$\begin{cases} L_3 = 2 \cdot k \cdot L_2 - L_1 \\ M_3 = 2 \cdot k \cdot M_2 - M_1 \\ N_3 = 2 \cdot k \cdot N_2 - N_1 \\ k = (L_1 \cdot L_2 + M_1 \cdot M_2 + N_1 \cdot N_2)/(L_2^{\ 2} + M_2^{\ 2} + N_2^{\ 2}) \end{cases} \quad \text{……. (Eq.4-4)}$$

Since reflected direction vector can be calculated with incident and normal directions, the reflected line can be easily expressed using the direction vector and the reflection point O, just as the incident line. Furthermore if incident and reflected lines are known, the normal can also be computed similarly.

4.1.2 Coordinate systems

1. Three coordinate systems

It is easy to see that locating the objects' positions is a very important part for system modeling, and all the system position parameters discussed in section

3.1.2 can be determined in the universal coordinate system except for the captured reflected dots in the image. Thus two more coordinate systems are introduced in the proposed machine vision system in order to locate the reflected dots on the images. One is the imaging plane coordinate system X'O'Z' and the other is image coordinate system X''O''Y''. Their positions are shown in Figure 4-3.

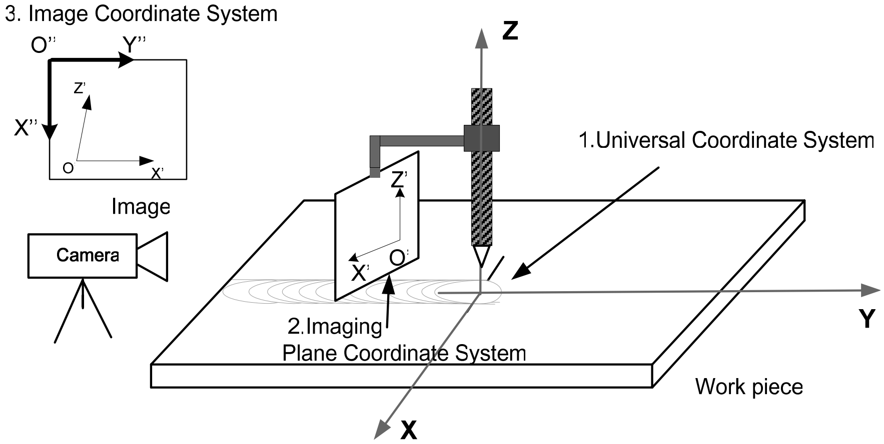

Figure 4-3, Three coordinate systems

In the figure, there are universal coordinate system (UCS), imaging plane coordinate system (IPCS) and image coordinate system (ICS) from right to left.

- Universal coordinate system (XYZ) is used to identify the positions of all the components in the proposed system. The origin O is located on the work piece beneath the electrode tip. Y axis is on the welding direction.
- Image coordinate is used to present the position of each pixel in an image, which complies with the rules of image processing. In image coordinate system (X''O''Y''), X'' presents the row and Y'' presents the column of a pixel in the image.
- Imaging plane coordinate system (X'O'Z') provide a convenient way to locate the reflected laser dots (or lines) on imaging plane from the captured image. Actually it is a bridge to convert ICS to UCS. The position of IPCS in UCS is configured when setting up the proposed observation system. The positions of axes in IPCS are chosen in the left-down corner of imaging plane.

2. The transforms among the coordinate systems

In the designed system, the main objective of coordinate transforms is to get the universal coordinates of reflected dots on the acquired image. Thus its image coordinates should be transformed into universal coordinate. The imaging plane coordinate system is introduced to realize it as a bridge. The transformation processes are shown in Figure 4-4. Firstly the image coordinates are changed into imaging plane coordinates, and then they are transformed into universal coordinates. It should be noted that the units of IPCS used in above two processes are different, but one can be easily converted into the other only by multiplying/dividing the number of millimeter in a designed unit of the axes.

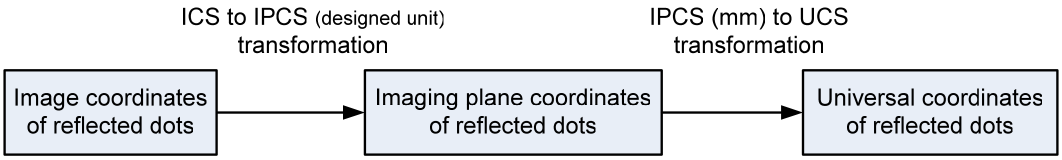

Figure 4-4, Coordinate transformation processes

- IPCS to UCS transformation

In Figure 4-5, the relationship between IPCS and UCS is shown. In the observation system, the imaging plane is placed vertically to Y axis of universal coordinate system at the negative side. In 2D imaging plane coordinate system (IPCS), Z’ axis is parallel to Z axis of UCS and X’ axis is parallel to X axis of UCS. Their units are both millimeter (mm).

Suppose P $\left(X'_P, Z'_P\right)$ is a random point in imaging plane in Figure 4-5. As can be see from the figure, the universal coordinates of point P $\left(X_P, Y_P, Z_P\right)$ can be calculated as:

$$\begin{cases} X_P = X'_P - S \\ Y_P = Y_{ip} \\ Z_P = Z'_P + h \end{cases} \qquad \text{……. (Eq.4-5)}$$

where *h* and *s* are shown in Figure 4-5 and they are distances between IPCS axes and UCS axes. *Yip* presents the Y coordinate of imaging plane in universal coordinate system. These three parameters are all measured (configured) during system configuration stage. Here *h* is small so as to capture all possible reflected structured light. Based on above equations, the coordinate transformation formulas from UCS to IPCS can also be deduced.

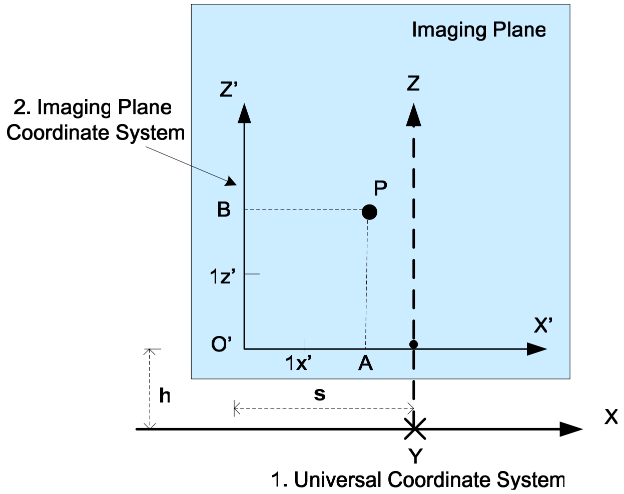

Figure 4-5, Relationship between IPCS (X'O'Z') and UCS (XYZ)

- ICS to IPCS transformation

In Figure 4-6, the relationship between IPCS and ICS is shown. In the acquired image, the imaging plane coordinate axes O'X' and O'Y' are also captured. During the experiments, the camera is placed directly facing the imaging plane. But due to the imprecision of the camera's position, the axes are not exactly vertical in the image unless the camera is placed exactly vertically to imaging plane. In the reflected images, the unit of image coordinate is pixel. The unit of IPCS depends on the design and it can be easily converted into millimeter (mm) by measurement.

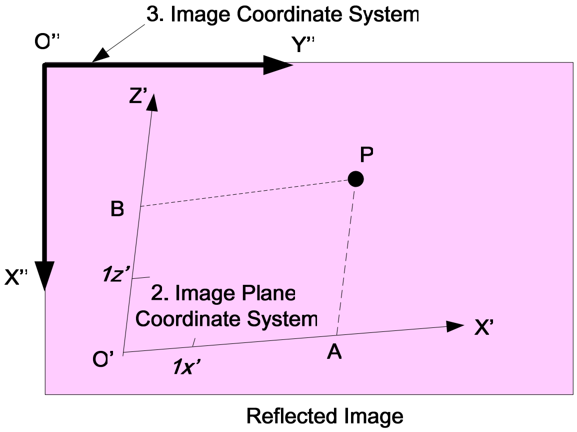

Figure 4-6, Relationship between IPCS (X'O'Z') and ICS (X''O''Y'')

As aforementioned, P is a random point on imaging plane and it is also captured on the acquired image by camera. Thus after the experiment only the image coordinates of point P $\left(X''_P, Y''_P\right)$ are known. In order to find its universal coordinates, its imaging plane coordinates should be calculated firstly. Since all the points on the image are actually from imaging plane, it is easy to find out if we draw two lines through point P parallel to imaging plane axes O'X' and O'Y', the intersection points A $\left(X''_A, Y''_A\right)$ and B $\left(X''_B, Y''_B\right)$can be decided, and the imaging plane coordinates of point P can be computed.

After imaging plane calibration mentioned in Chapter 5, the position information of imaging plane axes O'X' and O'Y' on the image are extracted. Suppose the image coordinates of point O'$\left(X''_{O'}, Y''_{O'}\right)$, point X' $\left(X''_{X'}, Y''_{X'}\right)$ (a point at O'X' axis, for example the unit point 1X' in Figure 4-6) and Z' $\left(X''_{Z'}, Y''_{Z'}\right)$ (a point at O'Z' axis, for example the unit point 1Z' in Figure 4-6) are known, the imaging plane coordinates of any point in image can be calculated. Firstly the unit length of axes O'X' and O'Z' on the image are computed using Eq.4-6. (The distortion of the lens is not considered here.)

$$\begin{cases} U_{X'} = \sqrt{\left(X''_{X'} - X''_{O'}\right)^2 + \left(Y''_{X'} - Y''_{O'}\right)^2} \Big/ l_{X'} \\ U_{Z'} = \sqrt{\left(X''_{Z'} - X''_{O'}\right)^2 + \left(Y''_{Z'} - Y''_{O'}\right)^2} \Big/ l_{Z'} \end{cases} \qquad \text{...... (Eq.4-6)}$$

where $l_{X'}$ and $l_{Z'}$ present the imaging plane coordinates of points X' and Z' on axes O'X' and O'Z' respectively. The IPCS axes can be expressed by two line equations in image coordinate system.

$$\text{Line O'X':} \quad \begin{cases} y = \dfrac{Y''_{X'} - Y''_{O'}}{X''_{X'} - X''_{O'}} \cdot \left(x - X''_{O'}\right) + Y''_{O'}, .if.X''_{X'} \neq X''_{O'} \\ x = X''_{O'}, if.X''_{X'} = X''_{O'} \end{cases} \qquad \text{... (Eq.4-7)}$$

$$\text{Line O'Z':} \quad y = \frac{Y''_{Z'} - Y''_{O'}}{X''_{Z'} - X''_{O'}} \cdot \left(x - X''_{O'}\right) + Y''_{O'} \qquad \text{...... (Eq.4-8)}$$

Then the line equations of PA and PB that are parallel to the coordinate axes are shown in Eq.4-9 and Eq.4-10 respectively.

Line PA: $$y = \frac{Y''_{Z'} - Y''_{O'}}{X''_{Z'} - X''_{O'}} \cdot \left(x - X''_{P}\right) + Y''_{P}$$ …… (Eq.4-9)

Line PB: $$\begin{cases} y = \dfrac{Y''_{X'} - Y''_{O'}}{X''_{X'} - X''_{O'}} \cdot \left(x - X''_{P}\right) + Y''_{P} \text{ ,.} if.X''_{X'} \neq X''_{O'} \\ x = X''_{P} \text{ ,} if.X''_{X'} = X''_{O'} \end{cases}$$ … (Eq.4-10)

By using the Eq.4-7 and 4-9, the image coordinates of intersection point A $\left(X''_{A}, Y''_{A}\right)$ can be solved as Eq.4-11a or Eq.4-11b.

$$\begin{cases} X''_{A} = \left(K_1 \cdot X''_{O'} - K_2 \cdot X''_{P'} + Y''_{P'} - Y''_{O'}\right) / \left(K_1 - K_2\right) \\ Y''_{A} = K_1 \cdot \left(X''_{A} - X''_{O'}\right) + Y''_{O'} \end{cases} .if.X''_{X'} \neq X''_{O'}$$ … (Eq.4-11a)

or $$\begin{cases} X''_{A} = X''_{O'} \\ Y''_{A} = K_1 \cdot \left(X''_{A} - X''_{O'}\right) + Y''_{O'} \end{cases} if.X''_{X'} = X''_{O'}$$ … (Eq.4-11b)

where K_1 and K_2 present the slopes of the axes: $\begin{cases} K_1 = \left(Y''_{X'} - Y''_{O'}\right) / \left(X''_{X'} - X''_{O'}\right) \\ K_2 = \left(Y''_{Z'} - Y''_{O'}\right) / \left(X''_{Z'} - X''_{O'}\right) \end{cases}$

By using the Eq.4-8 and 4-10, the image coordinates of intersection point B $\left(X''_{B}, Y''_{B}\right)$ can be solved as Eq.4-12a or Eq.4-12b.

$$\begin{cases} X''_{B} = \left(K_2 \cdot X''_{O'} - K_1 \cdot X''_{P'} + Y''_{P'} - Y''_{O'}\right) / \left(K_2 - K_1\right) \\ Y''_{B} = K_2 \cdot \left(X''_{B} - X''_{O'}\right) + Y''_{O'} \end{cases} .if.X''_{X'} \neq X''_{O'}$$ ... (Eq.4-12a)

or $$\begin{cases} X''_{B} = X''_{P} \\ Y''_{B} = K_2 \cdot \left(X''_{B} - X''_{O'}\right) + Y''_{O'} \end{cases} if.X''_{X'} = X''_{O'}$$ …… (Eq.4-12b)

Then the imaging plane coordinates of point P $\left(X'_{P}, Z'_{P}\right)$ are computed as Eq.4-13.

$$\begin{cases} X'_{P} = \begin{cases} \sqrt{\left(X''_{A} - X''_{O'}\right)^2 + \left(Y''_{A} - Y''_{O'}\right)^2} \Big/ U_{X'} \text{ ,} if..Y''_{A} \geq Y''_{O'} \\ -\sqrt{\left(X''_{A} - X''_{O'}\right)^2 + \left(Y''_{A} - Y''_{O'}\right)^2} \Big/ U_{X'} \text{ ,.........} Else.......... \end{cases} \\ Z'_{P} = \begin{cases} \sqrt{\left(X''_{B} - X''_{O'}\right)^2 + \left(Y''_{B} - Y''_{O'}\right)^2} \Big/ U_{Z'} \text{ ,} if..X''_{B} < X''_{O'} \\ -\sqrt{\left(X''_{B} - X''_{O'}\right)^2 + \left(Y''_{B} - Y''_{O'}\right)^2} \Big/ U_{Z'} \text{ ,.........} Else.......... \end{cases} \end{cases}$$ …(Eq.4-13)

Thus for a point P on the image, its image coordinates $\left(X''_{P}, Y''_{P}\right)$ can be transformed into imaging plane coordinates $\left(X'_{P}, Z'_{P}\right)$ by using equations Eq.4-

6 ~ Eq.4-13, and then (X'_P, Z'_P) can be further transformed into its universal coordinates using Eq.4-5 to realize the processes shown in Figure 4-4. During the transformation processes, the position information of imaging plane coordinates axes on the captured image should be known, and this is the main task of imaging plane calibration discussed in Chapter 5.

4.2 System Simulation

A computer simulation is a computer program that attempts to simulate an abstract model of a particular system. Through the established mathematical model, computer simulation can also be used to do research for our proposed sensing system and help us to know the system better. From former work, it is known that dot-matrix pattern is more suitable for measurement and the simulation is based on it. In this section, two kinds of system simulations are conducted. One is positioning simulation, and the other is correspondence simulation.

In the proposed system, the height of the electrode can only be adjusted in a limited range (typically 3 ~ 5 mm in GTAW), thus the projected or reflected laser rays would be blocked by the electrode if the position or angle of laser diode is not appropriate. Even if all the laser lights projected onto the weld pool surface are not blocked, whether the reflected rays can be projected onto the imaging plane is still decided by the position and size of the imaging plane. As can be seen, the system parameters are interactional, and the positioning simulation is needed to select/verify proper system parameters

As a part of system simulation, the correspondence simulation is used to find/validate the corresponding relationship between the projected rays and reflected dots on imaging plane under different circumstances, which is useful for weld pool surface reconstruction. Since in the experiments the corresponding position of “center reference point” in the reflected dot matrix can be found, if the relative corresponding relationships of dots are decided, it is easy to know which reflected dot in imaging plane is reflected from which incident ray.

4.2.1 Positioning simulation

4.2.1.1 Positioning analysis

In the positioning simulation, the main issue is how to select appropriate system parameters to avoid projected or reflected laser rays blocked and get all (or most) reflected rays intercepted by the imaging plane. Here in order to simplify the analysis, only the projected and reflected rays on YOZ plane are considered. This simplification is based on the assumptions that the shape of the electrode tip is conical and the weld pool surface is slightly deformed and smooth. There are three cases of the weld pool surface analyzed: flat plane, convex shape and concave shape, which are shown from Figure 4-7 to Figure 4-9. In the figures, H2 (H2’, H2’’) presents the height of the electrode; H3 (H3’, H3’’) presents the height of the laser diode; α is the projection angle of laser diode; L1 (L1’, L1’’) presents the maximal distance from the tail of weld pool surface to the electrode within which the projected rays are not blocked; L2 (L2’, L2’’) the maximal distance from the head of weld pool surface to the electrode within which the reflected rays are not blocked. This means if the head part and tail part lengths (size) of the practical weld pool surface is smaller than L1 (L1’, L1’’) and L2 (L2’, L2’’), the laser rays projected to and reflected from the weld pool surface would not be blocked by the electrode. Below each case is analyzed to calculate L1 (L1’, L1’’) and L2 (L2’, L2’’).

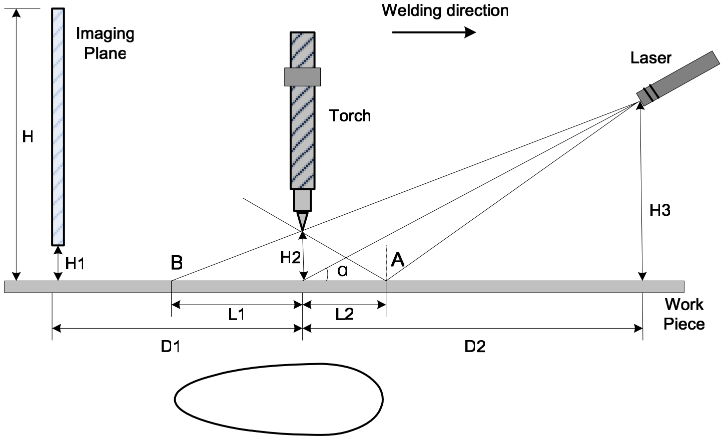

Figure 4-7, Positioning analysis on flat plane

If a flat surface is assumed, it is easy to use reflection law and similar triangles to calculate L1 and L2 as below:

$$\frac{L1}{L1+D2}=\frac{H2}{H3}\ldots\Rightarrow\ldots L1=\frac{H2\cdot D2}{H3-H2} \qquad \ldots\ldots\ldots\ldots\ldots\ldots\ldots \text{(Eq.4-14)}$$

$$\frac{L2}{D2-L2}=\frac{H2}{H3}\ldots\Rightarrow\ldots L2=\frac{H2\cdot D2}{H3+H2} \qquad \ldots\ldots\ldots\ldots\ldots\ldots\ldots \text{(Eq.4-15)}$$

Thus it can be deduced that if the profile of pool surface located within the segmentation AB, the laser rays projected to and reflected from the surface would not be blocked. Furthermore if the imaging plane height H is fixed, in order to capture the reflected ray from point A, the distance of the imaging plane D1 should be at least:

$$\frac{H2}{H}=\frac{L2}{L2+D1}\ldots\Rightarrow\ldots D1=\frac{H\cdot L2-H2\cdot L2}{H2} \qquad \ldots\ldots\ldots\ldots\ldots\ldots\ldots \text{(Eq.4-16)}$$

These values can give us a general idea to decide if the used parameters are suitable for the experiments when the shape of the weld pool is not known. For gas tungsten arc welding, the dimensions of the weld pool surface are typically less than 5 mm in width and 6 mm in length, which can be as a reference for the value of L1 and L2.

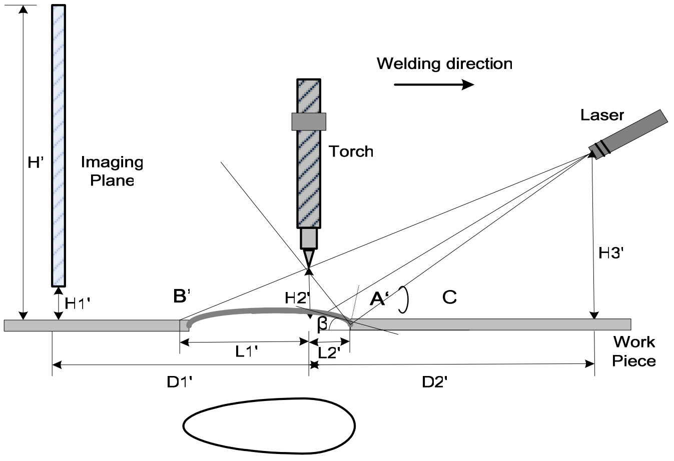

Figure 4-8, Positioning analysis on convex surface

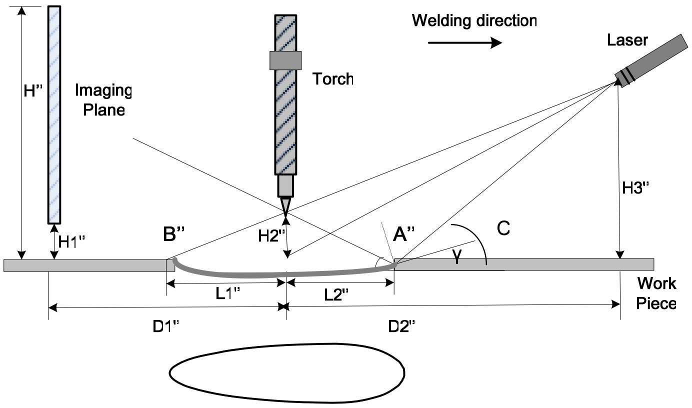

Figure 4-9, Positioning analysis on concave surface

If a convex surface is used as shown in Figure 4-8 and suppose the slope angle at head point A’ of weld pool surface is β, the value of L1’ is equal to L1, and the L2’ can be calculated from below equations. As can be seen, L2’ is smaller than L2.

$$\begin{cases} \dfrac{H2'}{\tan(2\beta + C)} = L2' \\ \dfrac{H3'}{\tan C} = D2' - L2' \end{cases} \qquad \text{…………………. (Eq.4-17)}$$

If a concave surface is used as shown in Figure 4-9 and suppose the slope angle at head point A’ of weld pool surface is ɣ , the value of L1’’ is equal to L1, and the L2’’ can be calculated from below equations. It is easy to see L2’’ is larger than L2.

$$\begin{cases} \dfrac{H2''}{\tan(C - 2\gamma)} = L2'' \\ \dfrac{H3''}{\tan C} = D2'' - L2'' \end{cases} \qquad \text{…………………. (Eq.4-18)}$$

By using above equations, the system parameters can be tested to see if they are selected appropriate to avoid laser dots blocking on the captured reflected images. However, the more direct and reliable way to test the parameters is to do the simulations as shown below.

4.2.1.2 Simulated pool surface

Based on the assumption of small deformation in smooth weld pool surface, part of sphere is used as a simple concave/convex weld pool surface in the simulation, which is shown in Figure 4-10. Here 2**r* is the width (length) of the weld pool surface and *d* is its depth. Some other numerical models of weld pool surface, such as the one in literature [51], can also be used in the simulation.

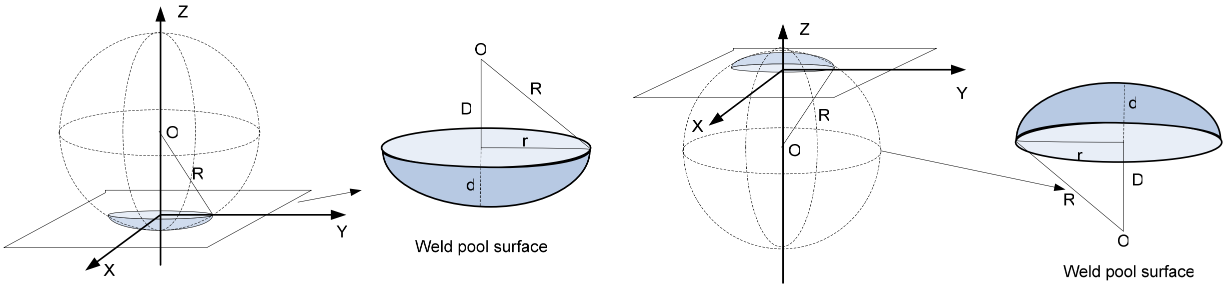

(a) (b)

Figure 4-10, Simulated weld pool surfaces (a) Concave surface (b) Convex surface

4.2.1.3 Simulation results

The simplified positioning analysis in section 4.2.1.1 is on YOZ plane. Here the convex and concave simulated weld pool surfaces shown in Figure 4-10 are used for the positioning simulations. The simulation can be run step by step to determine each parameter individually. The electrode height can be adjusted to the desired value (typically between 3 ~ 5 mm in GTAW). Here firstly the simulation runs to find the best location of the laser, and then the placement of the imaging plane is studied.

1. Position of laser diode

Several trials can be made in the placement of laser to determine the exact coordinates where the laser will not hit the electrode, and the 19-by-19 dot matrix laser pattern will cover the entire surface of the weld pool.

In order to make the distance among the projected dots small (usually 0.5mm), the distance between the laser diode and the origin of universal coordinate system should be firstly decided. According to the parameters of the laser (0.77 inter-beam angle), 30 mm is chosen as the distance from laser diode to the origin beneath the tungsten electrode. Based on this, different projection angles are tested for different size (shape) of weld pool surfaces. The height of the tungsten electrode is set to 0.5 mm.

Table 4-1 and Table 4-2 show the ray blocking situations by using different projection angles and convex/concave simulated surfaces. The projection angle changes from 20 degree to 45 degree, and the size (r/d) of weld pool surface varies. The term ‘r/d’ is used to present the radius (r) and depth/height (d) of the simulated surfaces. The ‘nb’ presents ‘no blocking’, and ‘rb’ presents ‘reflected rays blocking’.

Table 4-1, Blocking testes by using convex surfaces

size angle	**2/0.2**	**2/0.4**	**3/0.3**	**3/0.6**	**4/0.4**	**4/0.8**
20^o	nb	nb	nb	nb	nb	**rb**
25^o	nb	**rb**	nb	**rb**	nb	**rb**
30^o	nb	nb	nb	**rb**	**rb**	**rb**
35^o	nb	**rb**	nb	**rb**	**rb**	**rb**
40^o	nb	**rb**	**rb**	**rb**	**rb**	**rb**
45^o	nb	**rb**	**rb**	**rb**	**rb**	**rb**

Table 4-2, Blocking testes by using concave surfaces

size angle	**2/0.2**	**2/0.4**	**3/0.3**	**3/0.6**	**4/0.4**	**4/0.8**
20^o	nb	nb	nb	nb	nb	nb
25^o	nb	nb	nb	nb	nb	nb
30^o	nb	nb	nb	nb	nb	nb
35^o	nb	nb	nb	nb	nb	nb
40^o	nb	nb	nb	nb	nb	nb
45^o	nb	nb	nb	nb	nb	nb

As can be seen from Table 4-1, the reflected rays are blocked when the projection angle is large and the height of surface is large. It is in agreement with the analysis discussed in section 4.2.1.1. A small projection angle is more possible to avoid laser rays blocking. When the size of pool surface is 2/0.4, the 25 degree of projection angle makes the reflected rays blocked, while 30 degree does not. This can be explained that no laser rays are projected onto the boundary of the surface when projection angle is 30 degree. The blocking of the incident rays does not happen in the simulations since the tungsten is placed high and projection angle is not so large.

It can be seen from Table 4-2, the same concave surfaces and projection angles as Table 4-1 do not cause blocking, and the reason can be seen in section 4.2.1.1.

Similar tests can be done by changing other system parameters, such as the height of tungsten and the distance between laser diode and coordinate origin. It can be seen that these parameters are all limited by some conditions, and they should be chosen jointly to make a reasonable setup to avoid reflected rays blocking. Of course, the reconstruction algorithms developed later should have ability to rebuild the surface even when the blocking of reflected rays happens.

2. Placement of imaging plane

Since in our experiments the imaging plane size is chosen as 4”X4” (about 100 X 100 mm^2), it is important to set the position of the imaging plane appropriately to make all or at least most of the reflected rays intercepted. In Figure 4-11, different reflected images are shown by placing the imaging plane at different positions in the same simulated condition. The simulated surface is convex surface with radius 3 mm and depth 0.3 mm. The projection angle is 30 degree and the projection distance is 30 mm.

From the figure, it can be easily seen all the reflected rays are imaged in the 4”X4” imaging plane when it is placed 30 mm or 50 mm far from the torch, and the distance of 70 mm or 90 mm makes some of the reflected rays projected out of the imaging plane area. In addition, the intensity of the welding arc is another factor to affect the distance parameter. If the distance is short, the intensity of the arc on the image increases, but this would reduce the contrast between laser dots and background noise. Thus in order to make more reflected laser dots to appear clearly on captured images, the imaging plane should be placed properly. The system simulations can help us to achieve this goal.

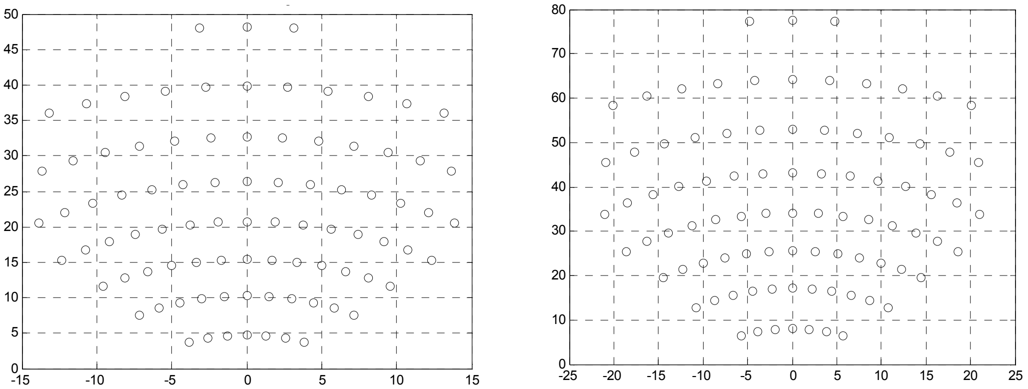

(a) at Y= -30 (mm)

(b) at Y= -50 (mm)

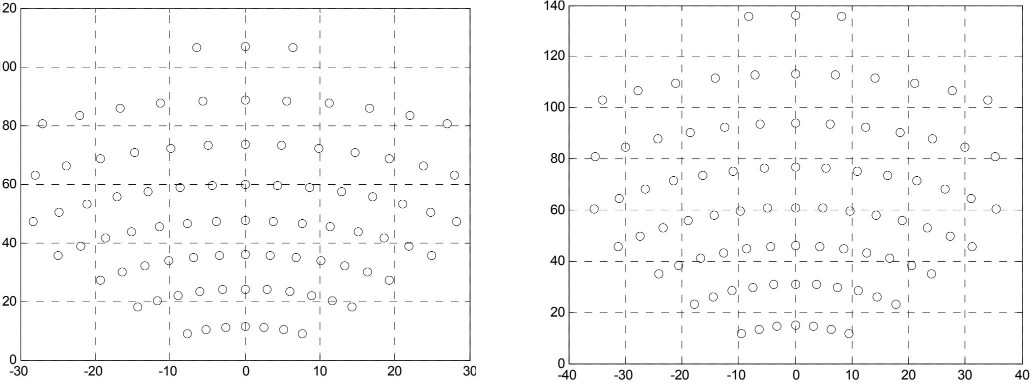

(c) at Y= -70 (mm)

(b) at Y= -90 (mm)

Figure 4-11, Reflected images with different imaging plane placements

4.2.2 Correspondence simulation

As can be seen from Figure 3-16 and Figure 3-17, the similarity of the reflected dots in the captured image makes it difficult to tell which incident rays in the dot matrix they come from. Correspondence simulation is thus conducted in order to find the possible corresponding relationships between projected and reflected laser points.

4.2.2.1 Corresponding relationships

It can be seen that the point position can be recognized by its row and column numbers not only for the projected dot matrix but also for the reflected image. In Figure 4-12, a 7 by 7 projected dot matrix and its reflected image are shown as an illustration example. This example will also be used later in Chapter 6 to illustrate the reconstruction scheme. In Figure 4-12 (a), $p_{i,j}(1 \le i, j \le 7)$ presents the projected point in ith row and jth column. A possible reflected dot pattern similar as the one on the captured image is shown in Figure 4-12 (b). The reflected row and column are distorted by the weld pool surface and $r_{i,j}$ presents the reflected point in ith row and jth column. As can be seen, the number/position of reflected dots depends on the size/shape of reflection surface and different row may have different numbers of reflected dots. For example, there are 3 reflected dots in the first row and 5 in the second row.

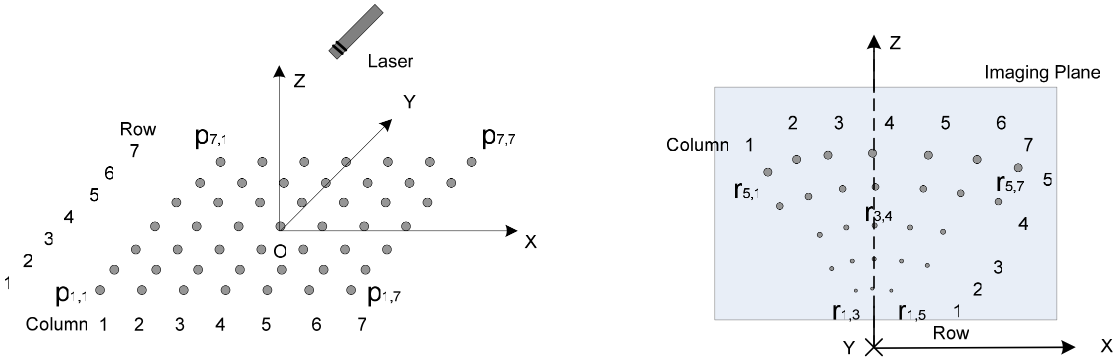

(a) Projected dot matrix (b) A possible reflected dot pattern

Figure 4-12, Projected and reflected dots locating

In the simulation, two kinds of corresponding relationships in the dot-matrix pattern are considered as shown in Figure 4-13. One is the column correspondence, which presents the column relationship of dots in a projected row and its reflected row. The other is the row correspondence, which tells the row relationship of dots in a projected column and its reflected column. They both have three types of mapping according to different shapes of reflection surface: sequential, inverse and disordered. In Figure 4-13 (a), the dots in kth row of projected dot matrix are investigated and the dash lines indicate the column corresponding relationship between projected and reflected points. In Figure 4-13 (b), three types of mapping of column corresponding relationships are shown. As can be seen, the differences among these mappings are caused by different statuses of weld pool surface, such as shallow or deep and concave or convex. In the following simulation, we set up different circumstances and try to find their corresponding relationships.

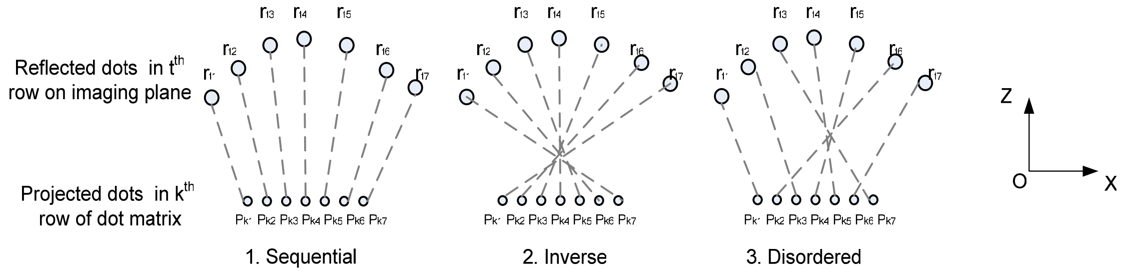

(a) Column corresponding relationship

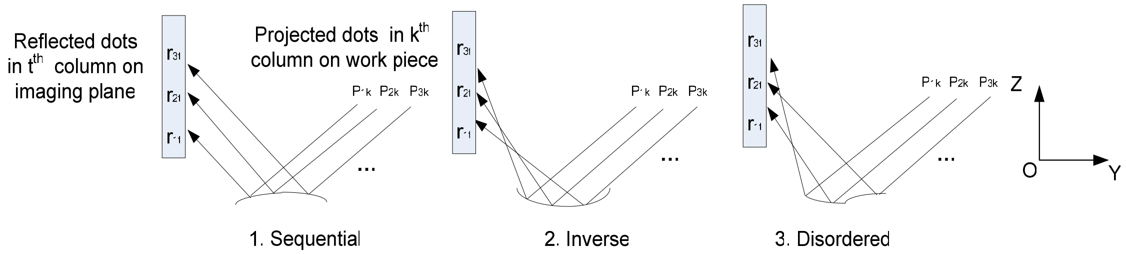

(b) Row corresponding relationship

Figure 4-13, Illustration for two kinds of corresponding relationships

4.2.2.2 Simulation parameters

In the simulation, some related parameters are considered.

- System Parameters

The system parameters obtained from one of the experiments is used. The distance between imaging plane and torch is 50 mm. The Laser projection angle is 31.14 degree and the laser distance to the origin is 31.48 mm. These parameters can also be changed to investigate different circumstances.

- Laser Parameters

Here the 7*7 dot-matrix (instead of 19*19 dot-matrix) pattern of diffractive laser is used as an example to illustrate laser parameters, which is shown in Figure 4-14. In the figure, the laser is projected vertically to the plane W, and the 7*7 dot matrix is in the form of a square.

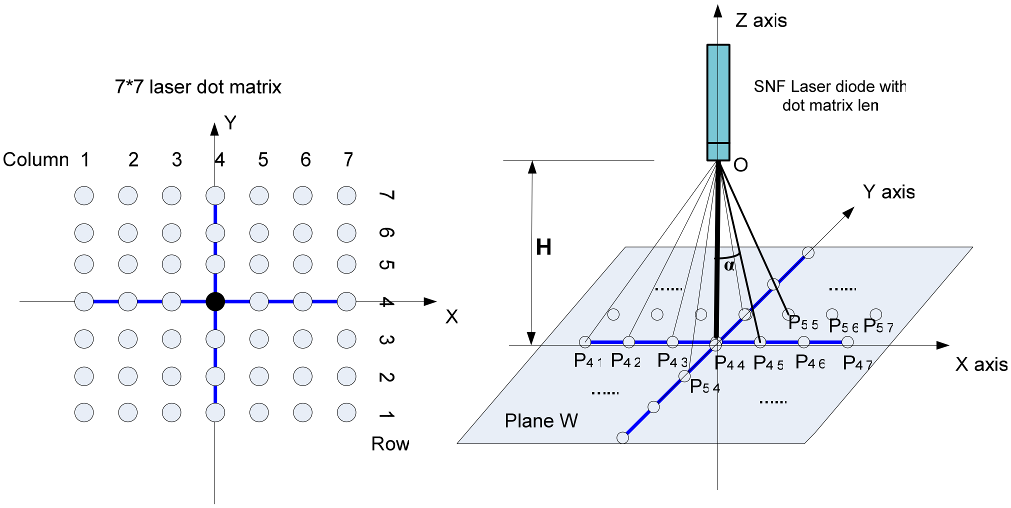

Figure 4-14, Illustration of dot matrix laser

The point $P_{4,4}$ is the center of the projected dot matrix and we can set up a coordinate system as shown in Figure 4-14. The intersection angle of line $OP_{4,4}$ and line $OP_{4,5}$ (angle $P_{4,4}OP_{4,5}$) is the parameter inter-beam angle (α). Inter-beam angle can be firstly used to compute the positions of points located on the main crossed lines in the Figure Then the parallel lines can be drawn through these points to form a grid, and the intersection points are the positions of other points in the projected dot matrix. One important thing should be noticed. From Figure 3-15, it is known the center reference point of dot matrix is not marked (here is point $P_{4,4}$). This characteristic can be used to identify the dots' corresponding relationships.

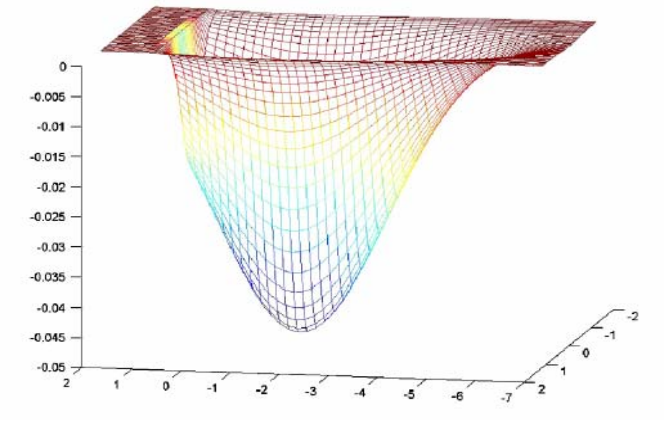

Figure 4-15, 3D shallow weld pool [52]

- Weld Pool Parameters

In literature [52], the laser welding process is investigated using numerical model. The weld pool surface is shallow since its depth is 0.05 mm while its width is 4 mm, shown in Figure 4-15.

Although laser weld pools are in general different from those of a gas tungsten arc, shallow laser weld pools generated by a low power, defocused (large diameter) beam should be similar to those of a gas tungsten arc. Hence, the analytical models derived from laser welding can be used to approximate gas tungsten weld pool surfaces using an energy beam wider than typical laser applications [52].

Table 4-3, Simulation Parameters Design

r **d**	**2mm**	**3mm**	**4mm**	**5mm**
d = r/100				
d = r/50				
d = r/10				
d = r/5				
d = r/2				

In literature [53], weld pool simulation is also done and light flow and feature point tracking technologies are used to do the research. For GTAW welding, the dimensions of the weld pool surface are typically less than 5 mm in width, 6 mm in length, and 0.5 mm in depth if the current is below 150 A as used for precision joining [53]. According to previous work, the simulated pool surfaces shown in Figure 4-10 are also designed as listed in Table 4-3. Firstly, different sizes of weld pool are investigated and the value of ***r*** is changed from 2 mm to 5 mm. Secondly, the depth of the weld pool ***d*** is also changed from *r*/100 to *r*/5, which is associated with the width.

4.2.2.3 Simulation results

The programming language MATLAB is used to do the correspondence simulation. The parameters listed in Table 4-3 are applied to simulate for both concave and convex surface. Here the blocking of reflected laser dots is not considered.

1. Concave simulated surface

Figure 4-16 shows the simulated concave surface with projected dot matrix on the work piece. The results of corresponding relationships using concave surface are shown in Table 4-4.

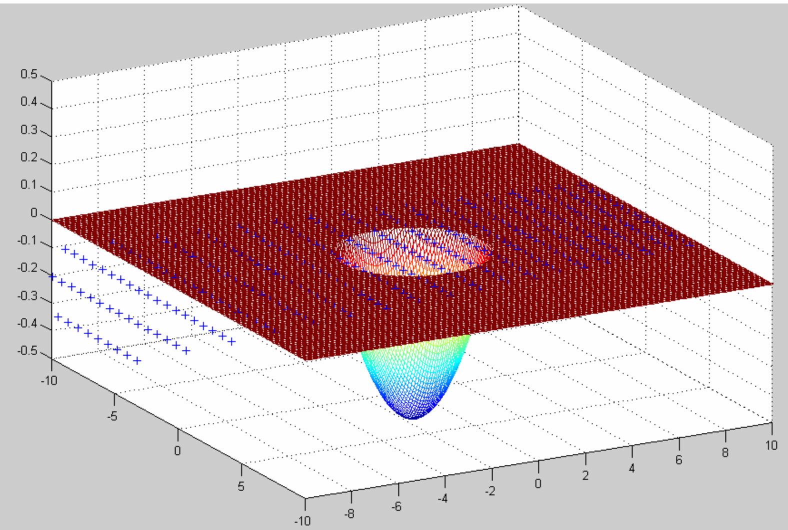

Figure 4-16, Simulated concave weld pool surface

Table 4-4, Correspondence Simulation Result of Concave Surface

r d	2mm	3mm	4mm	5mm	Image shape
d = r/100	S/S	S/S	S/S	S/S	Concave
d = r/50	S/I	S/I	S/S	S/S	Concave
d = r/10	I/I	I/I	I/I*	I/I*	Convex
d = r/5	I/I	I/I	I/I	I/I	Convex
d = r/2	D/D	D/D	D/D	D/D	

* Special cases, the image shape looks like sand timer with two column relationships.

Here the symbol ‘S’ presents ‘Sequential’, ‘I’ presents ‘Inverse’ and ‘D’ presents ‘Disorder’ corresponding relationship for both column and row correspondences. For each item in the table, the first letter presents column corresponding relationship and the second letter presents row correspondence. For example, when the geometric parameters of weld pool r = 3mm and d = r/50 = 0.06mm, the “S/I” in the table shows the column corresponding relationship is “sequential” and the row corresponding relationship is “inverse”. In Table 4-4, the column of image shape shows the shape of the reflected dot matrix on the imaging plane.

As can be seen when r = 3mm and d = r/10 = 0.3mm, the ‘I/I’ shows the dots corresponding relationship is inverse, the lines’ is also inverse and the shape of reflected image is convex, which can be seen from Figure 4-17.

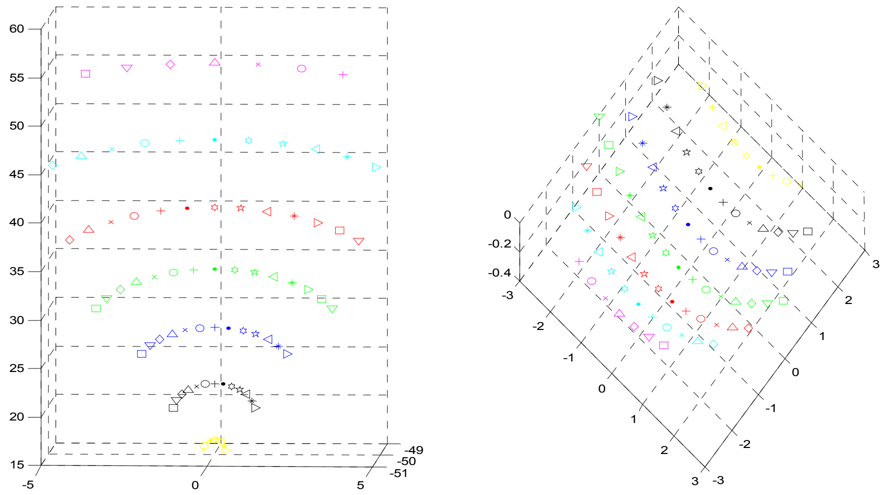

(a) Reflected dots on imaging plane (b) Projected dots on weld pool surface

Figure 4-17, Example of simulation using concave surface

In the simulation, a 19-by-19 dot-matrix pattern is used. In Figure 4-17 (a), the reflected dots on the imaging plane are presented. The view is from its front side, which is the same as the camera record. In Figure 4-17 (b), the projected dots located on the weld pool are shown, which form 5 concave curves on the weld pool surface. The laser is projected from right side (Y>0) with an angle and the used universal coordinate system can be found in Figure 3-1. Here different points in a row are marked with different symbols (triangle, square or cross etc.) and different colors are used for different rows (it can be seen only when Figure 4-17 is printed in color).

In some special cases in the simulations (marked with '*' in Table 4-4), the shape of the reflected dots on the image looks like a sand timer, which is shown in Figure 4-18. There are actually two column corresponding relationships in the image: the 'Inverse' for the upper part of the image and the 'Sequential' for the lower part. This kind of image is not found in the practical experiments. Since the observed images in experiments are similar as the upper part of the image in Figure 4-18, here the column corresponding of the upper part 'Inverse' is used to present that of the whole image, just as shown in Table 4-4.

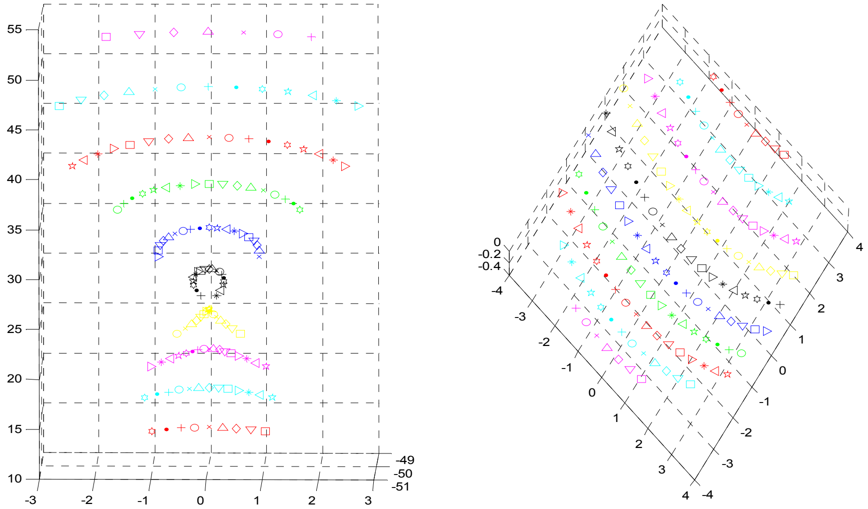

Figure 4-18, Special cases using concave weld pool surface

From the table, it can be seen for concave surface when its depth changes from shallow to deep, the shape of image in imaging plane turns from concave to convex. Through the observation of weld pool in section 3.2, the shapes of reflected images are nearly all convex. Moreover, when the weld pool geometric parameter d = r/5 and d = r/10 (near practical values in GTAW), it is found the column and row correspondence relationships are both 'Inversed', so we should consider it primarily in the reconstruction scheme. But for some cases when depth is very small, the row corresponding relationship is 'Inversed' and the column's is 'Sequential'.

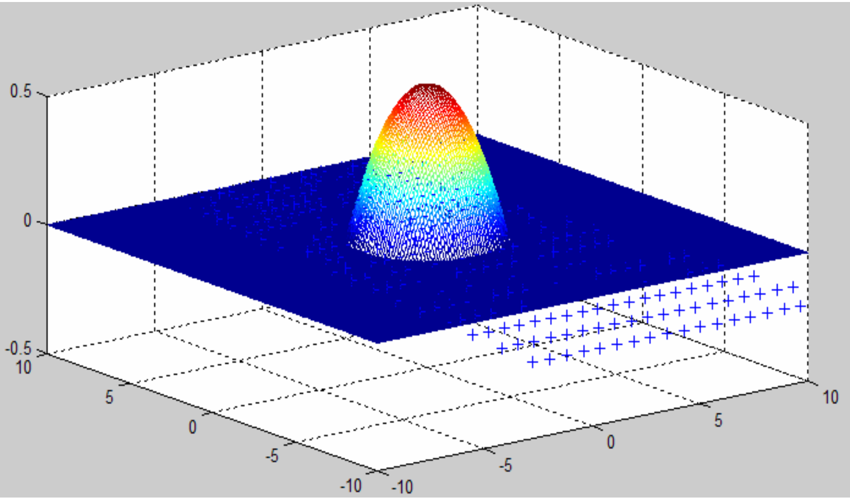

Figure 4-19, Simulated convex weld pool surface

2. Convex simulated surface

Figure 4-19 shows the simulated convex surface with projected dots on the work piece. The results of corresponding relationships are shown in Table 4-5. The meanings of the symbols are the same as Table 4-4.

Table 4-5, Correspondence Simulation Result of Convex Surface

r d	2mm	3mm	4mm	5mm	Image shape
d = r/100	S/S	S/S	S/S	S/S	Convex
d = r/50	S/S	S/S	S/S	S/S	Convex
d = r/10	S/S	S/S	S/S	S/S	Convex
d = r/5	S/S	S/S	S/S	S/S	Convex
d = r/2	D/D	D/D	D/D	D/D	

From above, it can be seen for convex surface the column and row correspondence relationships are nearly all ‘Sequential’ and all the reflected images are convex, so this should be considered for weld pool surface reconstruction. When r = 3mm and d = r/10 = 0.3mm, the column corresponding relationship is ‘Sequential’ and the row corresponding relationship is also ‘Sequential’, which can be see from Figure 4-19.

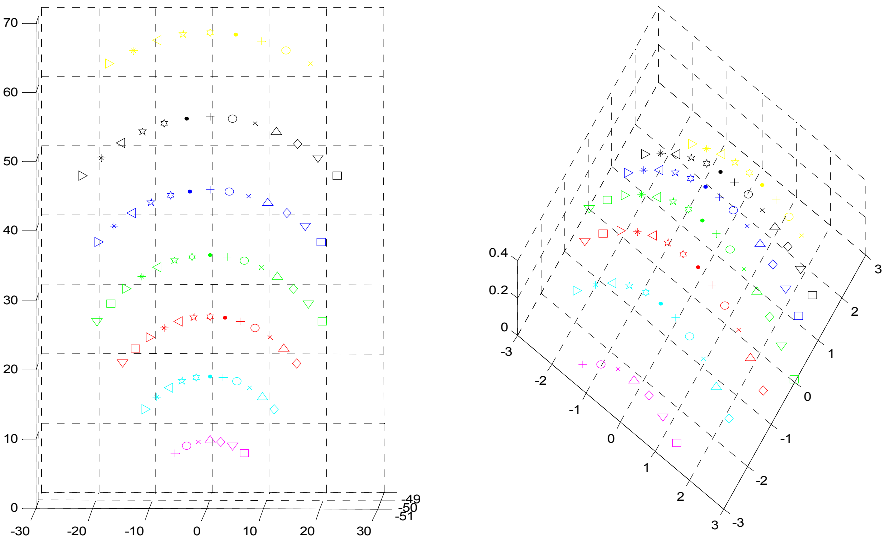

(a) Reflected dots on imaging plane (b) Projected dots on weld pool surface

Figure 4-20, Example of simulation using convex surface

4.3 Summary

System modeling and simulation provide a better way to describe and understand the proposed sensing system. In this chapter, specular reflection modeling describes the main principle behind the system, and the established coordinate system model helps to locate the positions of the reflected laser dots on captured images in the universal coordinate system. In simulation part, positioning simulation can help us to choose proper system position parameters to avoid rays blocking when capturing the reflected laser pattern. As an important part, correspondence simulations are used to find the possible corresponding relationships between projected and reflected laser rays. The simulation results show for most simulated concave surfaces, the shape of the reflected dots in a row is convex and the row and column corresponding relationships are ‘Inverse’. But for some cases when depth is very small, the row corresponding relationship is ‘Inverse’ and the column’s is ‘Sequential’. If the simulated is convex surfaces, the row and column corresponding relationships are all ‘Sequential’ and the shape of the reflected dots in a row is also convex.

CHAPTER 5

PROCESSING OF ACQUIRED IMAGES

Image processing techniques are used in machine vision domain to measure features and recognize patterns. In the proposed measurement system, it is important to process the reflected dot-matrix image so as to get some necessary information for the reconstruction scheme. For the reflected images shown in Figure 3-16 and Figure 3-17, there are two necessary tasks related to image processing. One is imaging plane calibration before experiments, which is to extract imaging plane coordinate system in the captured calibration image. The second task is to extract reflected laser points on reflected image, identify their row-column relationship and find corresponding position of the reference point.

In this chapter, some image processing techniques are applied, such as image segmentation, median filtering, morphological operation and pattern recognition [54] [55] [56]. A survey shows some related work [57] [58] [59] has been done for weld pool image processing.

5.1 Calibration Image Processing

Camera Calibration is the first step when trying to extract three-dimensional (3D) information from a two-dimensional (2D) image taken by that camera. It is a fundamental technique in 3D computer vision area. In our proposed experimental system, the reflected points on the image also need to be located in universal coordinate system, and the reflected points are all on the imaging plane physically. Hence, similar to the task of the camera calibration, “imaging plane calibration” is conducted before the experiments in our study.

In the observation system, the high-speed camera is placed nearly vertically to the imaging plane about 1~2 meters away to record the reflected points on imaging plane. The task of imaging plane calibration is to extract positions of imaging plane coordinate axes on the captured image. The ultimate objective is to realize coordinate transformation from image coordinate to imaging plane coordinate, which has been discussed in section 4.1.2. This means that given a reflected point in captured image its imaging plane coordinate and universal coordinate can be calculated. In this section, a simple imaging plane calibration method and its implementation procedures are discussed.

5.1.1 Design of image plane coordinate system

Three coordinate systems used in the system are discussed in section 4.1.2. As known parameters used in the transformation of three coordinate systems in Figure 4-5, the shift distance *h*, *s* and the distance *Yi* can be measured when system is set up. Also the position of imaging plane coordinate axes should be known on the reflected image. This means the positions of origin O’, the points at Z’ axis and X’ axis (for example unit positions 1z’ and 1x’ in Figure 4-6) should be identified from the acquired image by camera. How to make the feature points easily recognized? It is the task of the design of imaging plane coordinate system (IPCS).

Suitable imaging plane should be designed so that the coordinate system can be easily identified from the acquired calibration image. In Figure 5-1 three possible designs are shown, and they can be used to identify the imaging plane coordinate system. Once the positions of points O’, 1z’, 1x’ (or 2z’, 2x’) are decided in acquired image, the information of imaging plane coordinate system is achieved. Here the design in Figure 5-1 (c) is chosen for our application.

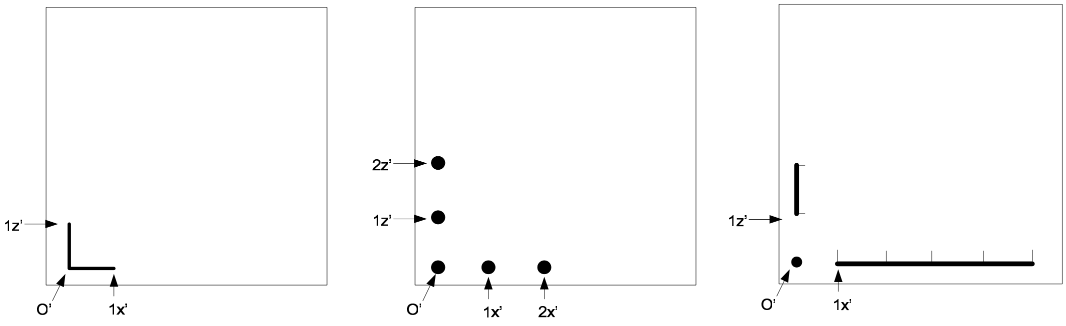

(a) (b) (c)

Figure 5-1, Three possible imaging plane designs

5.1.2 Coordinate system extraction

Once the system is set up, take a picture of the imaging plane with strong illumination light. Here the third coordinate system, shown in Figure 5-1 (c), is chosen in our research for accuracy and simplicity reasons.

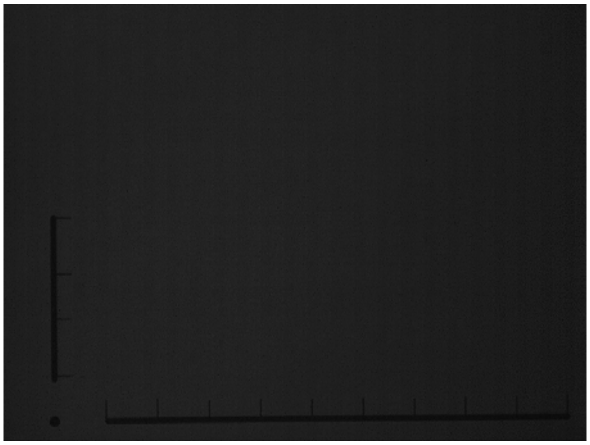

Figure 5-2, Calibration image with imaging plane coordinate axes

Figure 5-2 shows the calibration image of imaging plane with coordinate system. There are 4 units long in Z' axis and 10 units long in X' axis (plus the first unit), and the origin O' is marked with a big dot. The actual length of each unit on the axis is measured in advance. Because the band-pass filter is used and illumination light is not so strong (within the bandwidth), the contrast is not so obvious in the image. But it is good enough to extract positions of coordinate system.

In the process of imaging plane calibration, some image processing techniques are used in order to extract the positions of the original point O' and the axes O'X', O'Z' in the image. The main procedures are listed below:

1. Image segmentation

Segmentation is the process of separating objects from background. It is the building block for all the subsequent processes like shape analysis, object recognition, etc [55]. As one of the ways to perform segmentation, threshold-based techniques are widely used, especially in applications where speed is an important factor.

Here in order to realize real-time image processing, the thresholding technique is used to get the coordinate axes X’O’Z’ out of background. The operation of image segmentation by thresholding can be expressed as:

$$g(x,y)=\begin{cases}1 & if..f(x,y)<T\\ 0 & if..f(x,y)\geq T\end{cases} \qquad \text{...... (Eq.5-1)}$$

where *x* and *y* indicate the location (row and column) of each pixel, $f(x,y)$ presents the intensity value of pixel located at xth row and yth column in the original image, *T* is the selected threshold and $g(x,y)$ presents the intensity value of pixel after segmentation. Then the image becomes binary image after segmentation by using the threshold, which can clearly differentiate the coordinate system and the background.

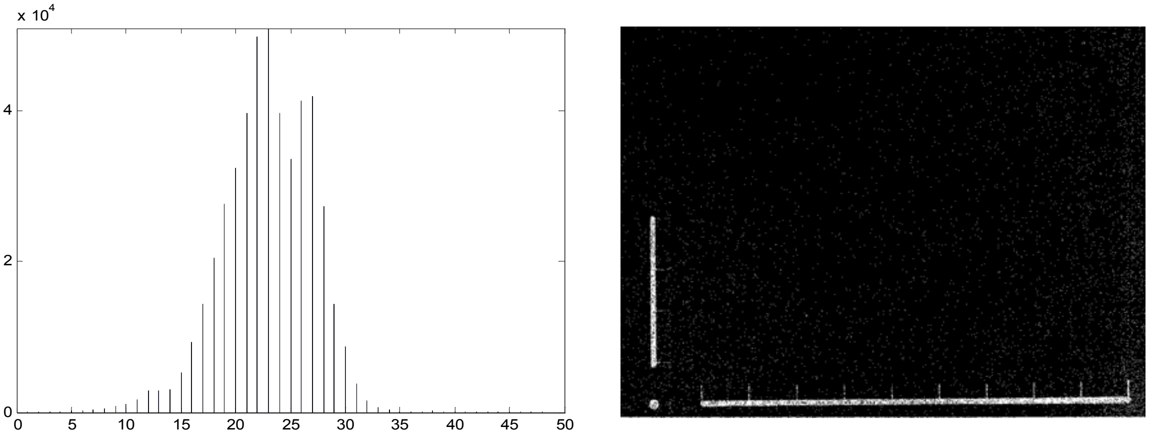

(a) Histogram of Figure 5-2 (b) Result after image segmentation

Figure 5-3, Illustration of image segmentation

Finding a proper threshold T for the image is the key issue for segmentation. In Figure 5-3 (a), a part of the histogram of Figure 5-2 is shown from 0 to 50 grey levels since the axes are drawn in black. It is hard to find the threshold because it is not an obvious histogram of a bimodal image. But we can still see there is a small peak around grey level 12, and we can set T= 14 as the threshold to segment the image. The result binary image after segmentation is shown in Figure 5-3 (b). As can be seen, the axes are extracted in the image, but there are still some scattered noises.

2. Noise deletion

There are several ways of image processing to deal with different kinds of noises, such as median filter for impulse noise and harmonic mean filter for Gaussian noise [54]. It is easy to find the main kind of noise existed in Figure 5-3 (b) is impulse (salt and pepper) noise. The probability density function (PDF) of impulse noise is given by [54]:

$$p(z) = \begin{cases} P_a & for..z = a \\ P_b & for..z = b \\ 0 & otherwise \end{cases} \qquad \text{...... (Eq.5-2)}$$

If neither P_a or P_b is zero, and especially if they are approximately equal, impulse noise value will resemble salt-and–pepper granules randomly distributed over the image. This kind of noise may come from the situations where quick transients take place during imaging since the camera take pictures at high speed (60 frame/sec or more) in the experiments.

Figure 5-4, Result after noise deletion

As a best-known order-statistics filter, median filter is effective to reduce random noise, especially impulse noise. The principle of median filter is to replace the value of a pixel by the median of the gray levels in the neighborhood of that pixel:

$$\hat{f}(x, y) = \underset{(s,t)\in S_{xy}}{median}\{g(s,t)\} \qquad \text{...... (Eq.5-3)}$$

where S_{xy} present the set of coordinates in a rectangular subimage window of size $m \times n$ centered at point (x, y), and $g(s,t)$ present the value of pixel at point (s,t) within the area S_{xy}.

In order to eliminate both the salt and pepper noise and the unit flags on axes, the window size 7×7 is applied for median filter to deal with Figure 5-3 (b), and the result is shown in Figure 5-8. As can be seen, the background noise has been successfully eliminated and only the needed coordinate axes are left.

3. Morphological operations

Mathematical morphology is an effective tool for extracting image components that are useful in the representation and description of region shape [54], especially for binary image. There are many kinds of morphological operations, such as dilation, erosion, thinning, thickening and pruning. Here we mainly use two: dilation and thinning.

(a) Image after dilation (b) Thin the binary image

Figure 5-5, Morphological operations

As can be see from Figure 5-4, it is possible some places at the axes may be broken because of unsuitable size of median filter. In order to keep the continuity of the axes, dilation operation is executed to merge broken parts of the axes. With A and B as sets in Z2, the dilation of A by B, denoted $A \oplus B$, is defined as:

$$A \oplus B = \left\{ z \middle| \left[\left(\hat{B} \right)_Z \cap A \right] \subseteq A \right\} \qquad \text{...... (Eq.5-4)}$$

where set B is commonly referred to as the structuring element in dilation and 3×3 matrix of ones are used for B in our application. The dilation is continued until there are only 3 objects (origin dot and two axes) left in the image by labeling the image [54]. The result of dilation is shown in Figure 5-5 (a).

Another morphological operation performed is thinning because the precise positions of the coordinate system are needed. The thinning of a set A by a structuring element B, denoted $A\otimes B$ can be defined in terms of the hit-or-miss transform [54] as shown in below.

$$A\otimes B = A-\left(A\Theta B\right)=A\cap\left(A\Theta B\right)^{C}$$

The thinning process is continued until no further changes occur, and the thinning result can be seen in Figure 5-5 (b).

4. Position information extraction

After above procedures, the imaging plane coordinate system is extracted, as shown in Figure 5-5 (b). The positions of origin O', axes O'X' and O'Z' in image coordinate system should be computed used for the coordinate system transformation in section 4.1.2.

By labeling the image, we can easily differentiate 3 objects in the image: origin O', axes O'X' and O'Z'. In order to minimize the error, the center positions of the objects are calculated to present their locations.

$$\begin{cases} x_i''=floor\left(\sum_{k=1}^{n_i} x_{i,k}''\Big/ n_i\right) \\ y_i''=floor\left(\sum_{k=1}^{n_i} y_{i,k}''\Big/ n_i\right) \end{cases} \quad i=1,2,3 \qquad \text{...... (Eq.5-5)}$$

where *i* present one of three different objects and *n_i* present the number of pixels in ith object. Function floor(X) is the greatest integers less than or equal to X. (x_1'',y_1''), (x_2'',y_2'') and (x_3'',y_3'') present the image coordinates of origin O', middle points (X' and Z') of axes O'X' and O'Z' respectively.

In the case shown in Figure 5-2 (480*640), the computed positions are O' (580, 54), X' (575, 450) and Z' (407, 53) in image coordinate system. Their imaging plane coordinates are (5.5, 0) and (0, 2.5). So for transformation from

ICS to IPCS in section 4.1.2, all of the needed conditions in Eq.4-6 ~ Eq.4-13 are already known which are shown in Eq.5-6.

$$\begin{cases} X''_{O'} = 580 \\ Y''_{O'} = 54 \\ X''_{X'} = 575 \\ Y''_{X'} = 450 \\ X''_{Z'} = 407 \\ Y''_{Z'} = 53 \\ l_{X'} = 5.5 \\ l_{Z'} = 2.5 \end{cases} \qquad \text{...... (Eq.5-6)}$$

5.2 Reflected image processing

After the imaging plane coordinate system is identified in the calibration image, the parameters for coordinate transformation processes, shown in Figure 4-4, are known. The next step is to process the reflected image to extract the position information of the reflected dots, which is useful for the later weld pool surface reconstruction scheme. The whole flowchart of reflected image processing is shown in Figure 5-6.

First of all, the reflected laser points in the image should be extracted based on their shape and size. Then based on the assumption that the deformation of the weld pool is small in GTAW so that the shape of reflected matrix does not deform severely, the reflected points are analyzed and some image features are determined, such as their row-column relationship and the position of reference point. Then the corresponding relationships discussed in section 4.2.2 can be applied to identify the corresponding projected point for each reflecting point in the image.

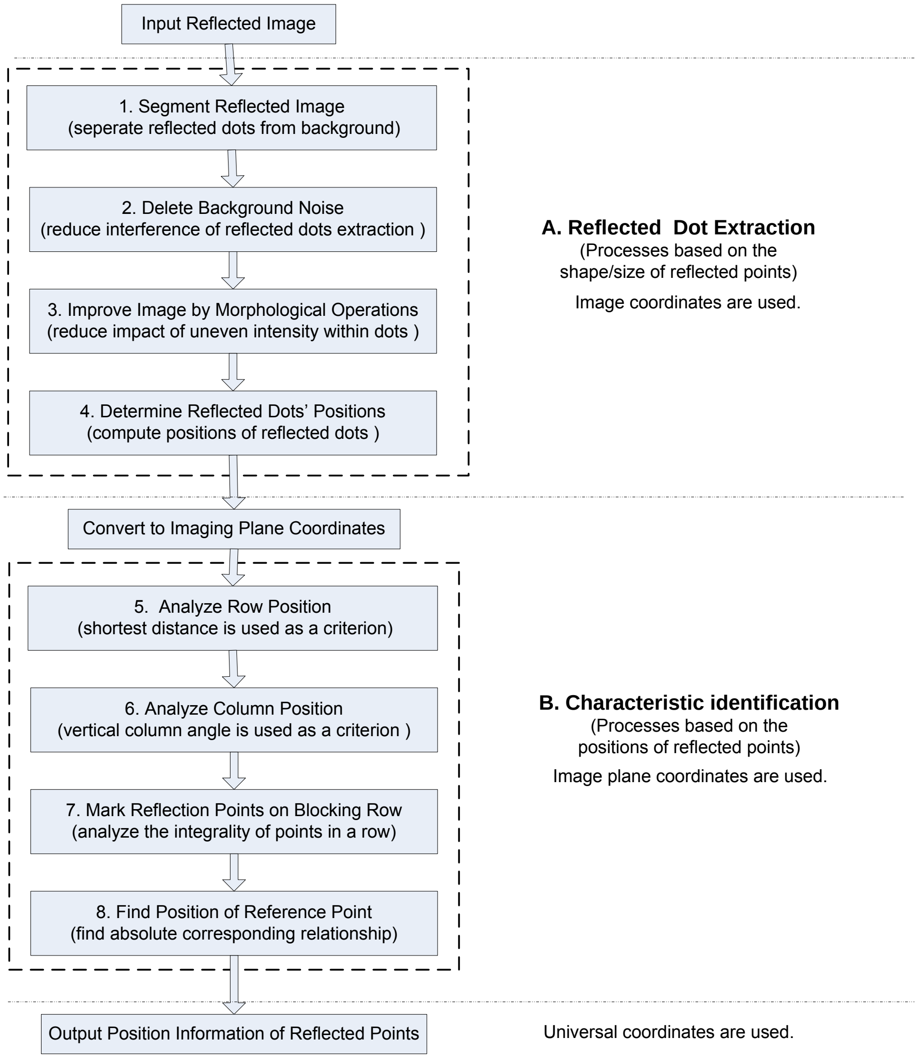

Figure 5-6, Procedures of reflected image processing

5.2.1 Reflected dot extraction

One example of the reflected images acquired by the monochromic camera during experiment is shown in Figure 5-7. In the image, the whole imaging plane is captured and there are some white reflected points in the black background (imaging plane). The grey degree difference (contrast) between them is not so obvious and some noises exist.

In this section, firstly the reflected bright points should be identified using image segmentation skills and their position should be calculated. Then their imaging plane coordinates can be computed using the coordinate transform formulas of Eq.4-6 ~ Eq.4-13 mentioned in section 4.1.2. The main problems in this step include low intensity contrast between reflected dots and background, noise interference and uneven intensity within the dots.

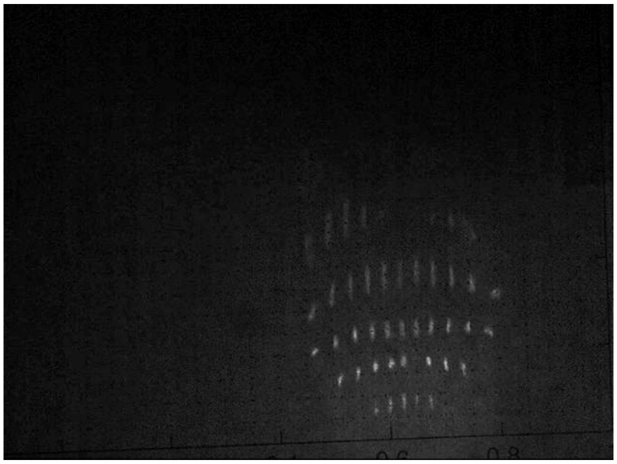

Figure 5-7, Captured reflected dot-matrix image

The main steps of dot extracting algorithm are shown in Figure 5-6 and discussed as below. In this process, image coordinates are used.

1. Reflected image segmentation

Image segmentation methods can be used to separate the reflected light dots from the background and noise. For the reflected image, one can also segment it into “reflected points” and “background” by simply choosing a threshold in brightness [55]. The choice of grey level threshold is important for the success of reflected point extraction.

There are several ways to realize thresholding by using proper threshold, ranging from the trivially simple to the very sophisticated. In our experiment, in order to balance the effect of segmentation and the real-time speed, a local thresholding approach called “block thresholding” is selected, in which the picture is partitioned into rectangular blocks and different thresholds are used on each block [55]. Let R present the entire image region, and R is partitioned into n subregions, R1, R2, R3 ……Rn., such that

$$\bigcup_{i=1}^{n} R_i = R \qquad \text{...... (Eq.5-7)}$$

Since the size of acquired images in the proposed system is 480*640 (pixel), 40*40 is chosen as the size of each block R_i for thresholding which is found to be able to balance speed and output results. For each subregion Ri, a different threshold is Ri is applied to segment the subimage, which is shown in Eq.5-8.

$$f_i(x,y)=\begin{cases}1 & if..R_i(x,y)>T_i \\ 0 & if..R_i(x,y)\le T_i\end{cases} \quad i=1,2,....n \qquad \text{...... (Eq.5-8)}$$

Here a simple strategy is chosen to find the threshold, which is to average the intensity in each block and choose the average intensity $\overline{I}_i$ plus ΔI as the threshold.

$$T_i=\overline{I}_i+\Delta I\ ,\ i=1,2,....n \qquad \text{...... (Eq.5-9)}$$

where ΔI is a small increase of intensity, and 5 is selected for 256 grey levels in our application. In Figure 5-8, the result is shown. After the segmentation, the input image becomes a binary image.

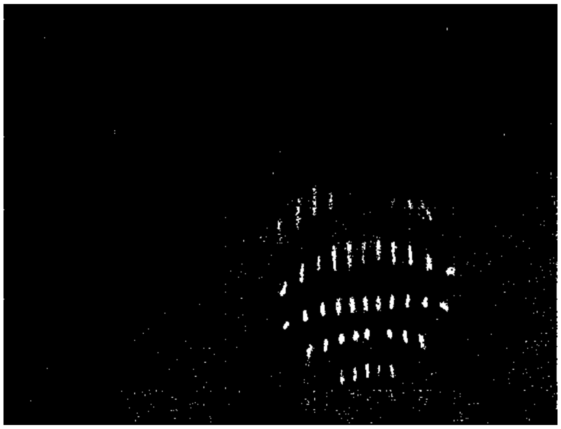

Figure 5-8, Block thresholding result

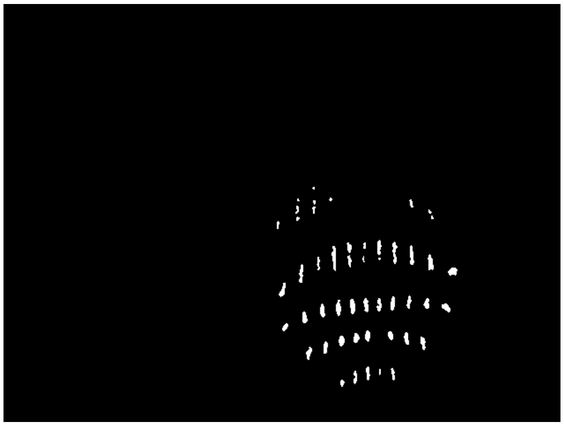

Figure 5-9, Two-level noise deletion result

2. Background noise reduction

There are still some noises in the image after the segmentation. The next step is thus to delete the background noises. Here two-level noise reduction operations are used.

In image processing technology, median filters are particularly effective in the presence of impulse noise, also called salt-and–pepper noise because of its appearance as white and black dots superimposed on an image [56]. Here considering the small size of majority of the noises, 3*3 median filter is chosen for the first level noise deletion.

After using median filter, there are still some relatively large noises (in comparison with the impulse noise) in the image. Hence in the next step, the average size of the dots in Figure 5-8 is calculated:

$$S_a = \left(\sum_{i=1}^{m} S_i \right) \Big/ m \qquad \text{...... (Eq.5-10)}$$

where m is the number of dots in the image and S_i presents the size of the ith dot in the image (unit: pixels). $S_a/6$ is selected based on experimental results as the threshold to delete the dots with smaller size which are considered to be noises. The operation can be expressed as:

$$g(x,y) = \begin{cases} 1 & if..(x,y) \in D_i..and..S_i > (S_a/6),..i = 1,2,...m \\ 0 & if..(x,y) \in D_i..and..S_i < (S_a/6),..i = 1,2,...m \\ f(x,y) & otherwise \end{cases} \qquad \text{...... (Eq.5-11)}$$

where $f(x,y)$ is the intensity of a pixel in the image after using the median filter and D_i presents the area of the ith dot. After this operation the big size noise dots (which left in the image after filtering with the median filter) and interference dots can be eliminated as shown in Figure 5-9.

3. Dots shaping using morphological operations

Due to the uneven intensity within reflected points in image, sometimes one reflected point may have been divided into several parts after segmentation, which can be seen from Figure 5-9. In order to reconnect the separated parts of the dots, some morphological operations should be done. One possible way is to dilate the dots in the image both in vertical and horizontal direction. After analyzing the features of the separated dot parts, the average length L_a and average width W_a of the dots in Figure 5-9 are computed:

$$\begin{cases} L_a = \left(\sum_{i=1}^{n} L_i \right) \Big/ n \\ W_a = \left(\sum_{i=1}^{n} W_i \right) \Big/ n \end{cases} \qquad \text{...... (Eq.5-12)}$$

$$\begin{cases} L_i = \max\{y \mid (x,y) \in D_i\} - \min\{y \mid (x,y) \in D_i\} \\ W_i = \max\{x \mid (x,y) \in D_i\} - \min\{x \mid (x,y) \in D_i\} \end{cases} i = 1,2,...n \quad \text{… (Eq.5-13)}$$

where n is the number of dots in the image shown in Figure 5-9 and D_i presents the area of the i^{th} dot. And La and Wa are used as the length of vertical and horizontal structuring element vectors for dilation. The result of dilations is shown in Figure 5-10. As can be seen, the separated parts of one reflected dot are reunited, which greatly improve the quality of the image.

Figure 5-10, Results of dots dilation

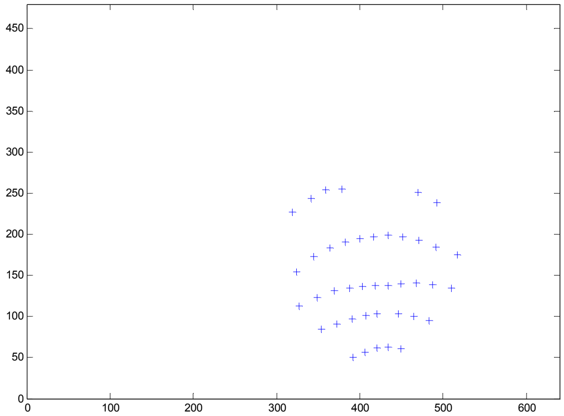

Figure 5-11, Position determination

4. Determination of the reflected points' position

In this step, the center pixel position of each dot is calculated to precisely present its position in the image coordinate system, as shown in Eq.5-14.

$$\begin{cases} x_i = \sum_{k=1}^{n_i} x_{ik} \Big/ n_i \\ y_i = \sum_{k=1}^{n_i} y_{ik} \Big/ n_i \end{cases} ,.....(x_{ik}, y_{ik}) \in D_i and..i = 1,2,...m \quad \text{…… (Eq.5-14)}$$

Here m is the number of dots and ni present the number of pixels in the ith dot. $(x_i \quad y_i)$ presents the calculated position of the ith reflection dot in the image. Figure 5-11 shows the positions of the reflected dots in image coordinate system.

5.2.2 Characteristic identification

Once the reflected laser points are extracted from image and their positions are calculated, the following task is the characteristics identification. One is to decide position relationship of reflected points. The other is to locate the position of the reference point. During these processes, imaging plane coordinates are used in the algorithm, shown in Figure 5-12.

This is a kind of pattern recognition problems, which may be solved by some existing algorithms. In order to simplify the processing procedures for our case, a new dot matching algorithm is developed. The main procedures of position and characteristic identification are discussed below.

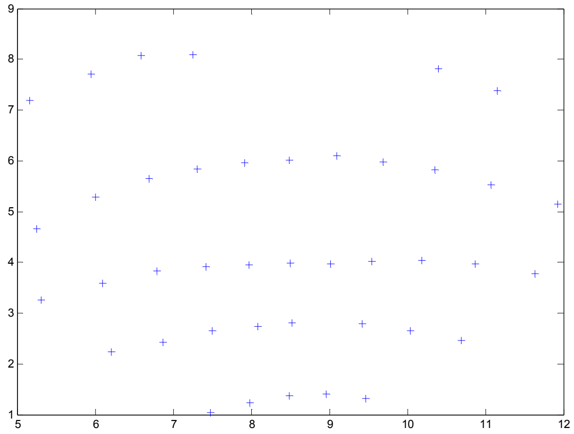

Figure 5-12, Reflected points (imaging plane coordinates)

1. Row position analysis

For a pair of dots, there are mainly two parameters used to describe their relative positions. One is distance, and the other is the angle of their connected line. They are all important for the decision of row/column relationship among the reflected dots. Through analysis, it is found that the distance plays more important role in deciding the row relationship and the angle is more important for column relationship in the reflected images.

The procedures of row searching algorithm are shown in Figure 5-13. Firstly an available reflected point set R is built. Then the rows of reflected points are searched one by one. At first, beginning point of each row is selected, which is located on the most left position within set R. Then its right neighbor in the same row is found by searching for the nearest point. The search of points in the same row is continued until the row angle conditions (row angle is less than 60 degree and change of row angle is less than 90 degree) are not satisfied, which indicates the end of this row. Then begin to search for the next row until all the dots are categorized into particular rows.

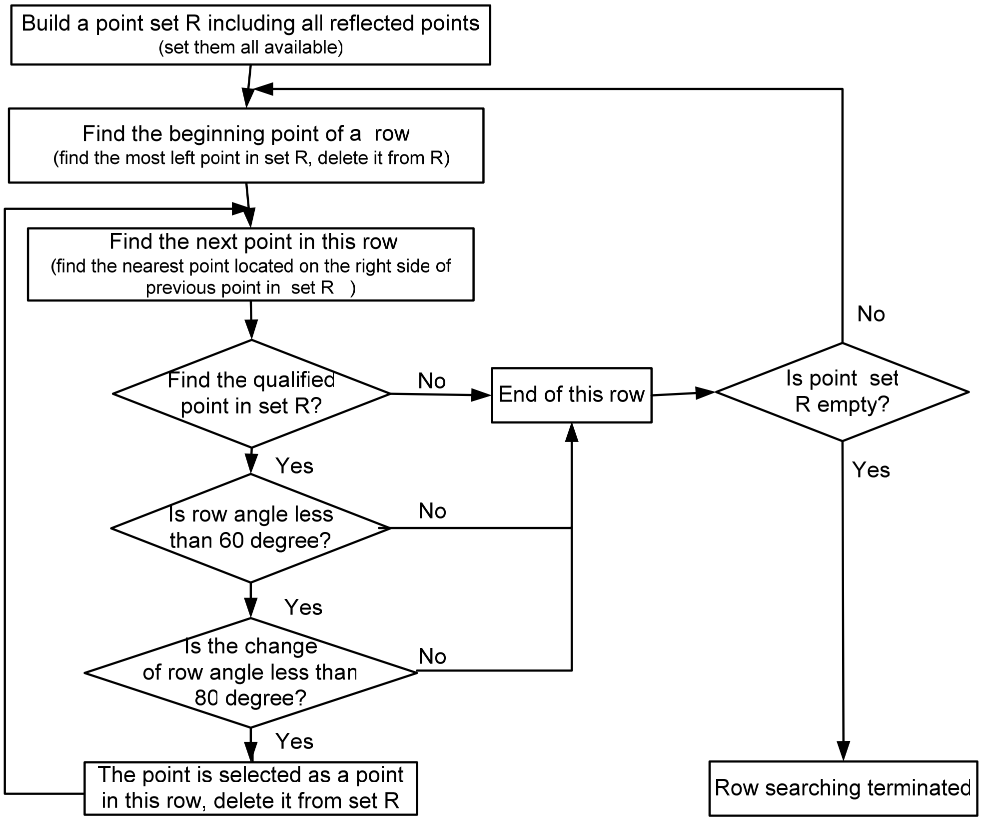

Figure 5-13, Flowchart of row searching

Here the row angle of a dot is defined as the angle of line connected this dot and its left neighbor point and the x-axis of imaging plane coordinate system, which is shown in Figure 5-14. And the beginning point of each row has no row angle, such as point A. As can be seen in Figure 5-15, five rows are found by the row searching algorithm, which verified the accuracy of the method.

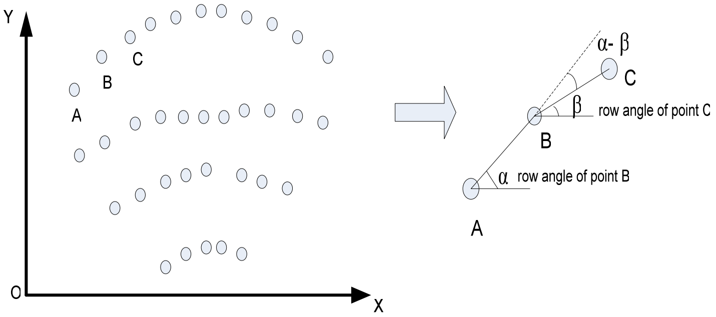

Figure 5-14, Row angle illustration

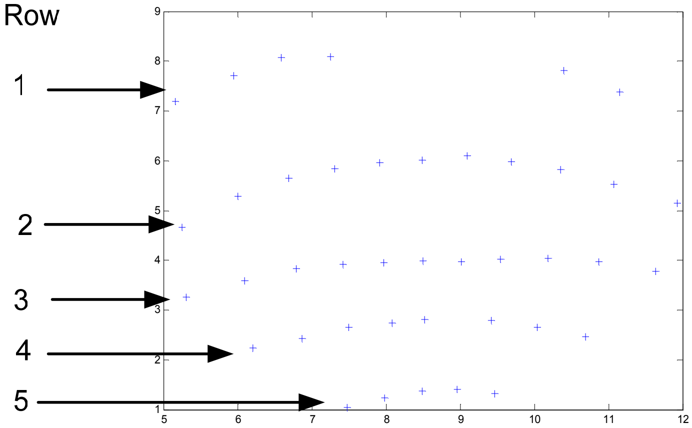

Figure 5-15, Result after row searching

2. Column position analysis

The next step is to decide the column position for each point in the rows. The main idea is to find the row with the most points and assign the column number from left to right. Then using this row as a reference, the column position of the points of its neighbor rows (below or above it) can be decided by column angle. Hence through one by one search, the column positions of points in all rows can be determined. The procedures of column searching algorithm are detailed in Figure 5-16 and are not repeated here.

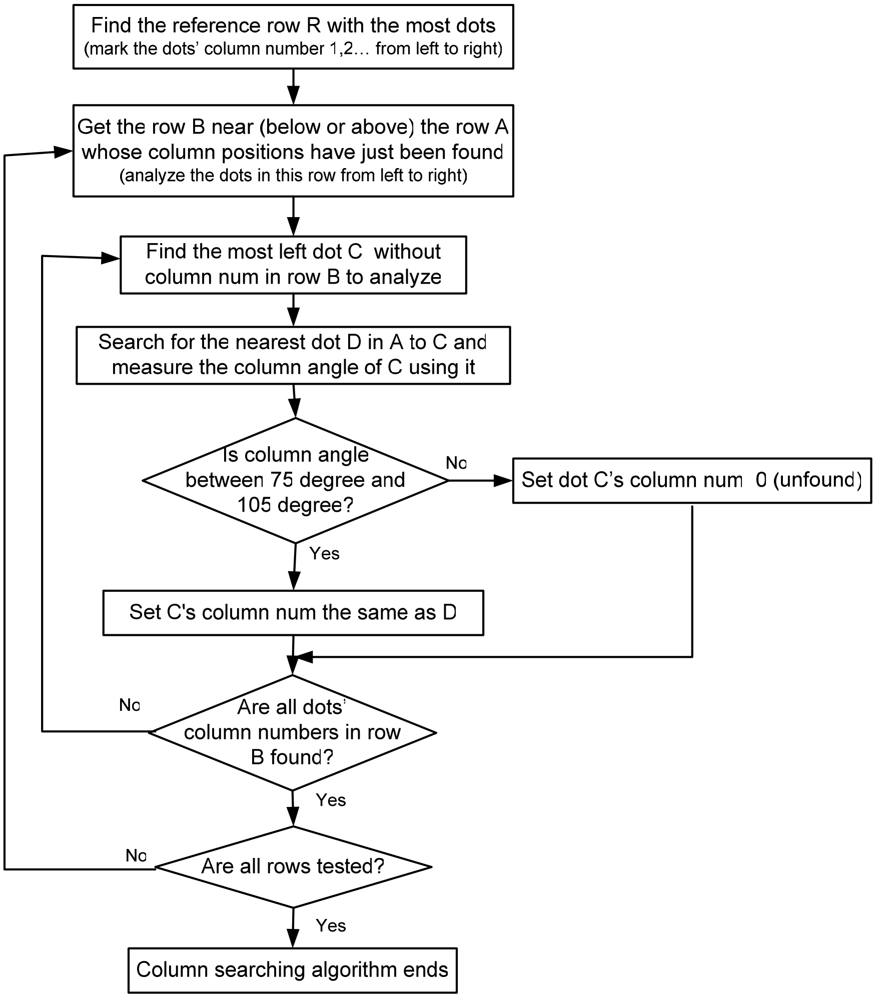

Figure 5-16, Flowchart of column searching

Here the column angle of a dot is defined as the angle formed by the line connecting this dot and a dot in its neighbor row with the x-axis, which is shown in Figure 5-17. The result of column searching is shown in Figure 5-18.

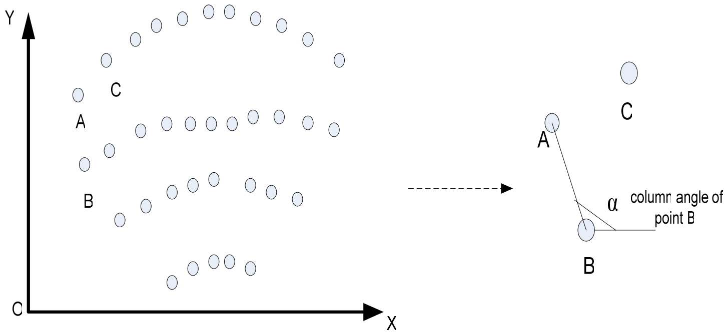

Figure 5-17, Column angle illustration

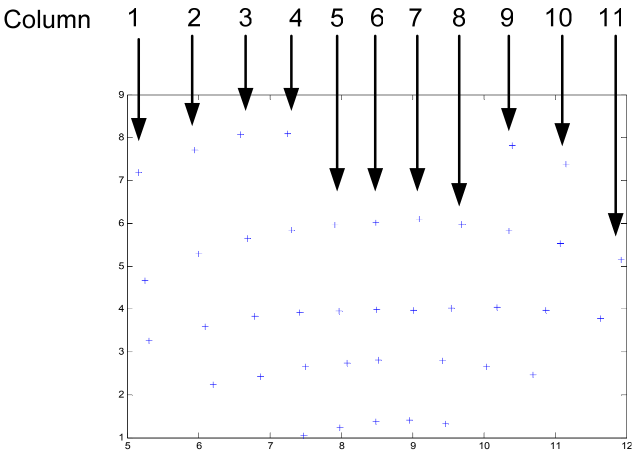

Figure 5-18, Result after column searching

3. Blocked row marking

In the welding process, the torch blocks some reflected laser dots in a row, which should be identified. After the column position of each point is decided, it is easy to judge row integrity. The columns of three middle points in the row with the most points are considered as reference columns. If there is more than 1 point in a row not locating in these columns, this row is marked as blocked row and may not be used for computation of weld pool surface.

4. Reference point determination

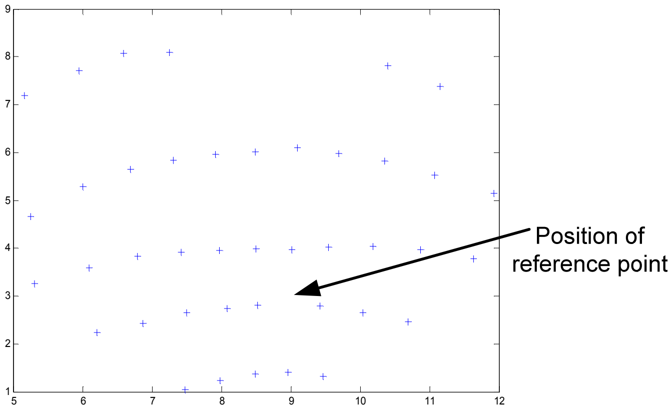

Figure 5-19, Position of reference point

This refers to find the row with one missing center column point. If two or more rows are available, the row with missing point in the center is chosen. The position of the missing point should be corresponding to the center position (10th row and 10th column) in the projection 19*19 dot matrix. Thus the reference point can be found, as shown in Figure 5-19.

5.2.3 Result analysis

After the image processing, the relative row and column position is decided for each reflected laser point, just as shown in Figure 5-20 (a). For example, the points B, C and D belong to 4th row and the points E, C and F locate in 3rd column. The position of reference point can be found in the circled area A, which is corresponding to the 10th row and 10th column absent point in the projected 19*19 dot matrix.

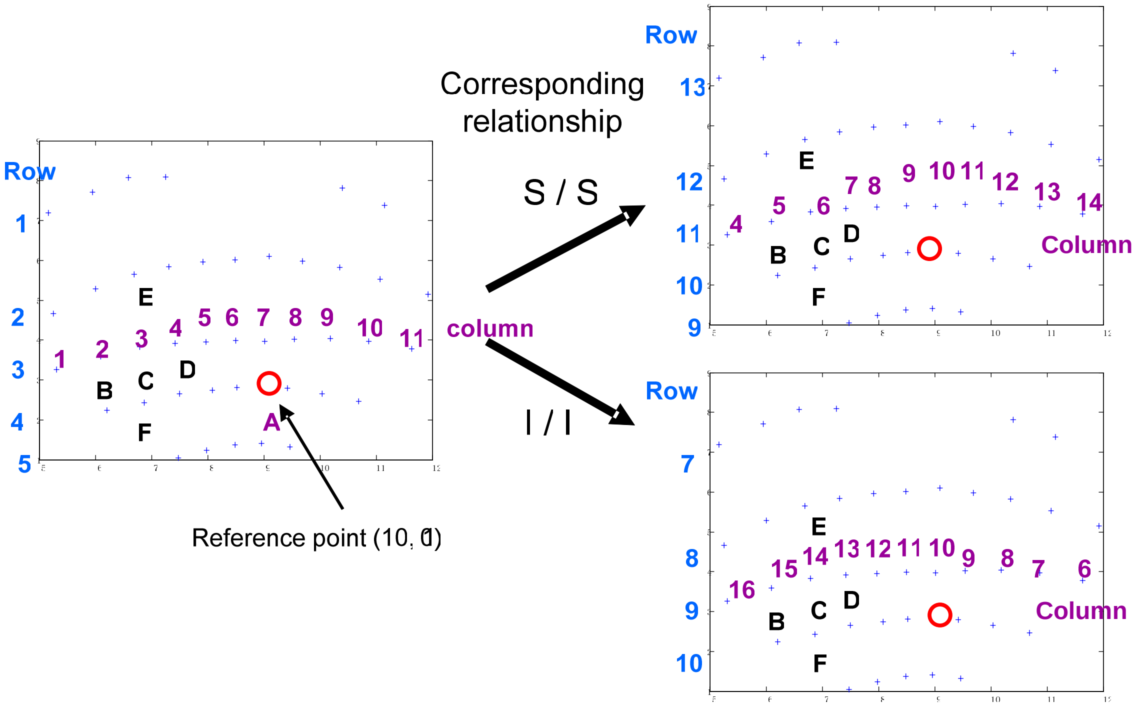

(a). Reflected dots' positions (b) Corresponding projected dots' positions

Figure 5-20, Illustration of correspondence relationship between projected and reflected dots

If the corresponding relationship discussed in section III is known, the absolute reflection position for each reflected point can be further determined, which means one can tell a reflected point is reflected from which point in the projected dot matrix. In Figure 6-16 (b), the different results of absolute positions are shown according to different correspondence relationships. For example, if the dots and lines correspondence relationship are both sequential (S/S), point C is reflected from the projected point at 11th row and 6th column in the 19*19 dot matrix. If the correspondence relationships are both inverse (I/I), it is reflected from the point at 9th row and 14th column. These possible correspondence relationships can be used later in the computation of the weld pool surface.

5.3 Improvement of reflected image processing

In above sections, the image was recorded when welding direction was along negative Y axis of universal coordinate system. From the discussion in section 3.2.2 it can be seen more laser dots can be reflected onto the imaging plane when the welding direction is changed to positive Y axis direction. Figure 5-21 shows the two images taken in different welding directions. As can be seen, the reflected dot-matrix pattern becomes denser in Figure 5-21, which provides more useful information for reconstructing three-dimensional weld pool surface. Meanwhile, this introduces a more challenging problem for the image processing algorithm, especially for the row/column position analysis. Thus improved image processing algorithm is proposed. This work is done with the help of Aparna Janga.

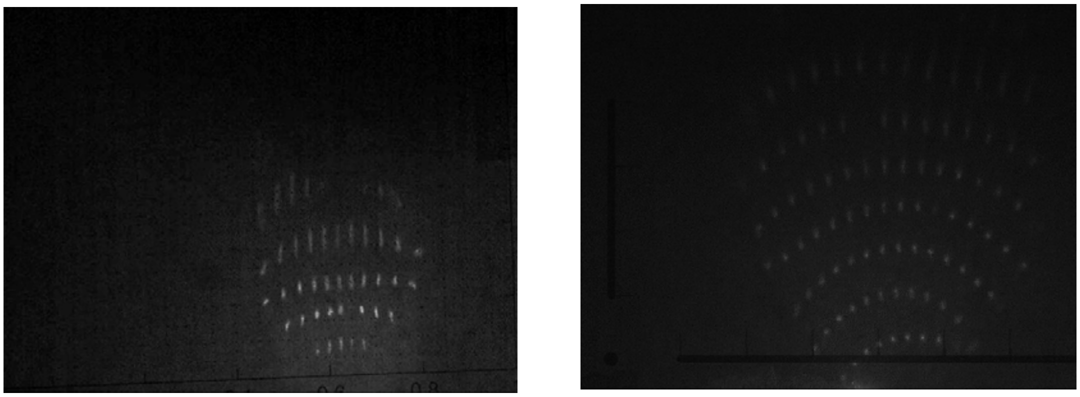

(a) Welding direction along negative Y axis (b) along positive Y axis

Figure 5-21, Captured reflected images along different welding directions

In the improved scheme, the main processing procedures are the same. Firstly the reflected dots are extracted, and then their row/column positions are analyzed. However, different processing methods are applied in each step.

1. Reflected dot extracting

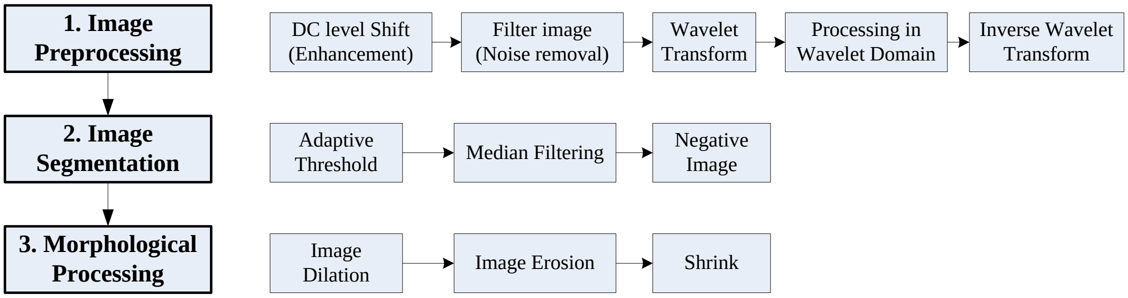

Figure 5-22, Improved reflected dot extraction procedures

During this stage, three processes shown in Figure 5-22 are conducted in order to get the extracted reflected dots in the image. They are image preprocessing, image segmentation and morphological processing, and their detailed steps are also shown in the Figure

The obtained reflected image in Figure 5-21 (b) is firstly DC level shifted, and then is filtered to remove the noise introduced by the camera. After that, wavelet transformation is applied. Further processing is done in wavelet domain and then inverse transform is computed to obtain a clear image. This pre-processing is actually an image enhancement process, and it ensures better performance of subsequent image analysis steps. The result is shown in Figure 5-23.

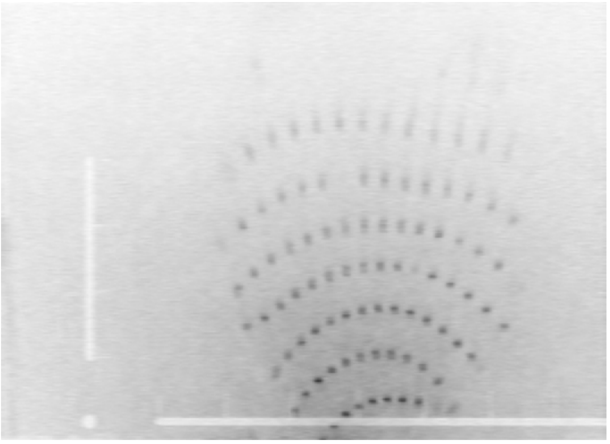

Figure 5-23, Result after image pre-process (enhancement)

The pre-processed image is then segmented to extract the dots. This is done through adaptive thresholding [54] which results in a binary image. The obtained binary image contains salt and pepper noise and needs to be filtered using median filter further. In the third step, morphological operations are conducted. Image dilation followed by erosion will result in a clean image. In the final binary image shown in Figure 5-24, dots may be recognized by pixel values of one (white) and background by pixel value of zero (black).

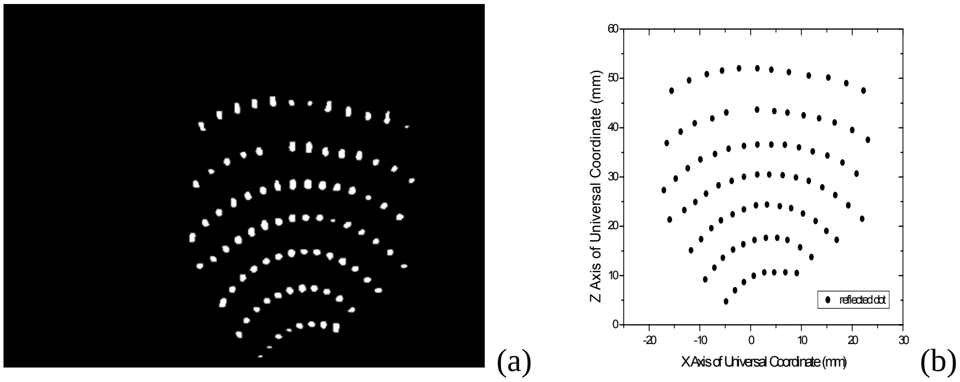

(a) (b)

Figure 5-24, Result of dot extracting

2. Characteristic identification

This stage involves the extraction of row/column information of the reflected dots and decision of center reference point position. The flowchart of the algorithm is illustrated in Figure 5-25.

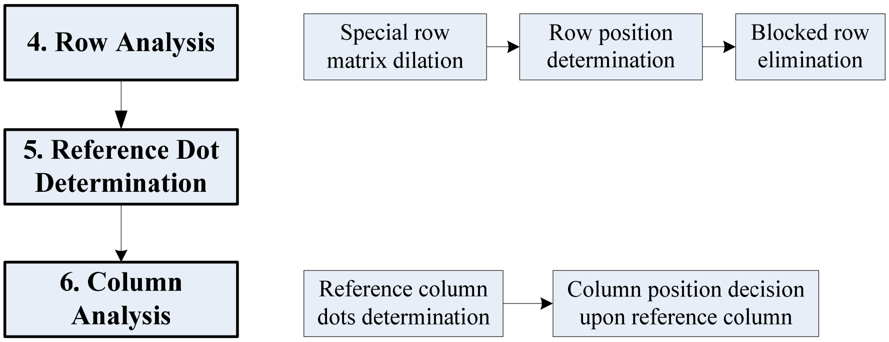

Figure 5-25, Processes of characteristic identification

In the processed reflected image, it can be observed that dots belonging to the same row are located closely while dots belonging to different rows are farther apart. This fact can thus be used to group dots in the same row. Different from proposed algorithm in section 5.2, a special dilation method is applied to form some masks to analyze the row position. It can be seen through the experiments the shape of the reflected dot matrix pattern is mostly convex within captured images. Hence, two specially designed matrixes shown in Figure 5-26 are used to dilate the image so as to connect dots in the same row. Then left half of the image in Figure 5-24 (a) is dilated using the matrix in Figure 5-26 (a) while the other half is dilated using another special matrix in Figure 5-26 (b).

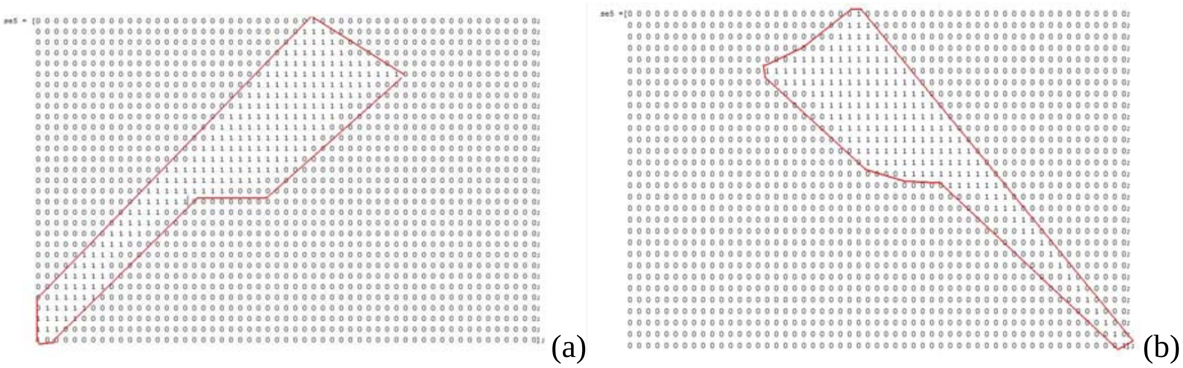

Figure 5-26, Specially designed dilation matrixes

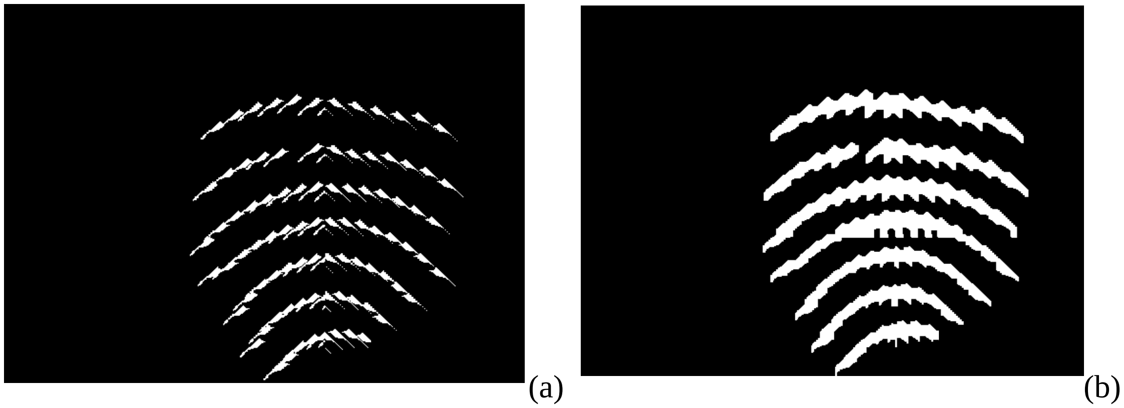

Figure 5-27, Image dilation for row analysis

The dilation result is shown in Figure 5-27 (a), and then it can be further dilated to form the row masks in Figure 5-27 (b). The connected white regions (masks) in the image show the different areas of the rows. Combined Figure 5-27 (b) with the figures in Figure 5-24, the reflected dots located in a row stripe area are classified into one row, and row positions of all reflected points can thus be decided.

Then further studies are conducted based on row analysis in order to detect the position of reference point and the blocked rows. The detected rows are firstly ordered according to the highest point in a row (with maximal Z coordinate). Based on the position information of the most left point in a row, the most right and the highest points in the rows, the two rows with relative small vertical distance are reclassified into one row, and if their horizontal distance is also smaller than 1.5 times average horizontal distance of dots in the row, it is deemed as the row with the (missing) reference point, such as the 5th row in Figure 5-27 (b) from bottom up. Otherwise the row should have a few missing dots and are marked as the blocked rows.

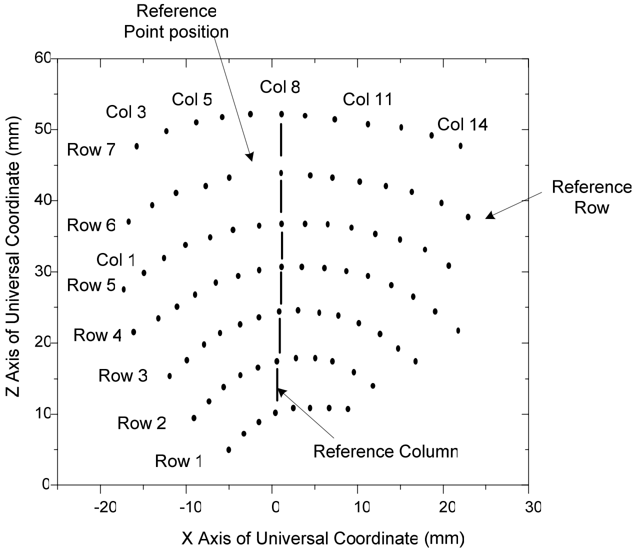

Figure 5-28, Result of characteristic identification

At last, the row with reference point is selected as the reference row and one reflected point in its middle position is chosen to find column positions for all the reflected dots. It can be easily seen in the middle part of the reflected image the position distortions of dots are small, thus the dots belong to the reference column can be decided by using a vertical line, which means in each row the nearest dot to the line is thought to be in the reference column, Once in each row the dot in reference column is determined, the relative column positions of its adjacent dots can all be deduced. Hence, the column positions of all reflected dots are found. The result is shown in Figure 5-28.

3. Result analysis

It can be seen the improved image processing algorithm can effectively process the reflected images with dense reflected dot-matrix pattern.

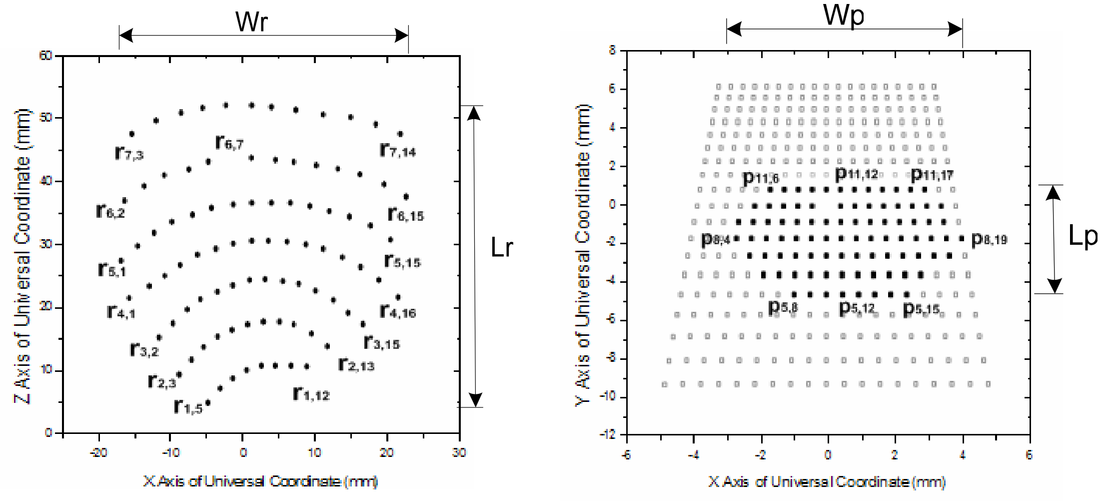

(a) Extracted reflected dots (b) Corresponding projected dots

Figure 5-29, Result analysis of reflected image processing

In Figure 5-29 (a), $R = \{r_{k,t}, (k,t) \in I\}$ presents the set of reflected dots on reflected image I and the subscripts present the row and column positions of the dots in reflected image. There are 7 rows (curves) and 16 columns found in the reflected image. Meanwhile, in Figure 5-29 (b) $P = \{p_{i,j}, (i,j) \in S\}$ presents the set of corresponding projected (reflection) dots on weld pool surface S, and they are marked with solid dots in the projected dot matrix. In Figure 5-29 (a), the corresponding position of the center reference point can be easily found in the position of $r_{6,7}$.

Combined with the corresponding position of reference point ($r_{6,7}$) in captured image each reflected dot on imaging plane can be successfully matched with a projected dot in the matrix by using different corresponding relationships. For instance, if the corresponding relationship is S/S, the matched points pair is

$r_{k,t} \xleftrightarrow{reflection} p_{k+10-6,t+10-7}$ as shown in Figure 5-29 (b); if the corresponding relationship is I/I, the matched points pair is $r_{k,t} \xleftrightarrow{reflection} p_{10+6-k,10+7-t}$. The matched point-ray pairs can be used to reconstruct the weld pool surface.

5.4 Summary

This chapter focuses on the development of algorithms for processing the image of a dot-matrix laser pattern reflected from the weld pool surface in order to obtain the data needed to reconstruct the weld pool surface. The dot-matrix pattern used provides an acceptable method to successfully establish the reflection-projection correspondence needed to reconstruct the weld pool surface. It reduced the image contrast but eased the point matching. In this chapter, the proposed dot extracting algorithms are capable of extracting the reflection points from the image with reduced contrast, and the proposed dot matching algorithms can successfully match the reflection points to their projections points. The processed results provide useful data for the weld pool surface reconstruction scheme. Furthermore, it can be seen that the proposed improved image processing algorithm can also effectively process the reflected images with denser dot-matrix pattern when the welding direction is changed.

CHAPTER 6

INTERPOLATION RECONSTRUCTION SCHEME

After the correspondence relationships are investigated in Chapter 4 and the positions of reflected points are extracted in Chapter 5, the reconstruction schemes can thus be developed based on the achieved information. The objective of the schemes is to rebuild the three-dimensional (3D) weld pool surface according to the reflected dots and the preconfigured system parameters. In this dissertation, two reconstruction schemes, which are called interpolation reconstruction scheme (IRS) and extrapolation reconstruction scheme (ERS), are proposed. In this chapter, interpolation reconstruction scheme is firstly discussed.

6.1 Problem Statement

After acquiring the necessary data and system position parameters for reconstruction, the reconstruction problem can be restated. Every incident ray in the projection laser dot-matrix can be represented by a line equation based on the knowledge of laser position and projection angle. In Figure 6-1, LA is one of the laser rays in the projection dot-matrix and the equation of line LA is known. This ray is reflected by an unknown specular surface S to produce a reflected point R on the imaging plane. Then the objective of reconstruction is to acquire the intersection (reflection) point P of incident line LA and reflected line BR on the surface S. It is apparent that reflection point P can not be calculated precisely because of insufficient constraints. To resolve this issue, an engineering method should be proposed to estimate the position of the reflection point P. Since there is a dot matrix projected on the surface, the positions of a series of reflection dots on the surface also can be optimally estimated, which will be used to reconstruct the surface S as the three-dimensional weld pool surface.

In the experiments using mild steel as work pieces, two important facts have been observed and confirmed. The first is that the dots projected within the weld pool area will be reflected by its specular surface and others located out of the weld pool will not. This means all the dots on the captured image are reflected from the weld pool surface. The second is that the incident laser dot and its reflected dot on the imaging plane can be easily matched by locating the center reference point and finding corresponding relationship as mentioned in Chapter 5.

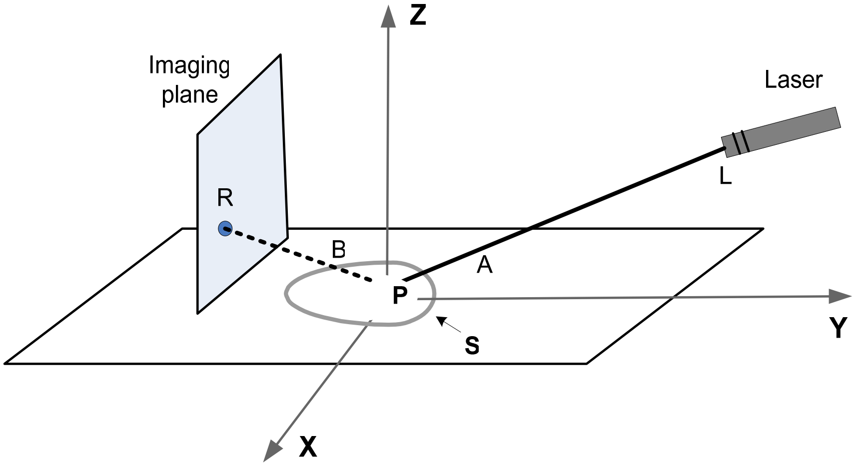

Figure 6-1, Problem illustration

Based on the problem statement and two facts discussed above, an iteration process is proposed as the surface reconstruction method.

(0) Assume a surface as the initial estimate of the weld pool surface;

(1) Use the estimated surface, the reflection points on the surface which reflect the incident rays and the reflection rays can thus be calculated as estimates;

(2) The calculated reflection rays and their matched incident rays can be used to calculate a field of slopes at reflection points based on the reflection law;

(3) The field of slope can be used to calculate a new surface as the updated estimate of the weld pool surface;

(4) Using the updated surface and the incident rays, the new reflected image can be calculated. The differences between the reflected points in the acquired and calculated images can be further mapped into the errors of reflection points on the weld pool surface. If this error meets the preset threshold, the updated surface is accepted as the weld pool surface; otherwise the updated surface is used as a new initial surface to repeat

the iteration process starting from step (1).

In particular, since the depth of the weld pool is much smaller than its width and length for GTAW process [60], it is reasonable to use a flat plane, i.e., Z=0, as the initial estimate of the weld pool surface in step 0. To use the slope field to estimate dots on the weld pool surface, the weld pool surface is assumed to be smooth. With known dots on the weld pool surface, a new surface can be re-estimated/reconstructed using surface fitting, interpolation methods or/and extrapolation methods. Since it is difficult to set up a proper three-dimensional model for weld pool surface, interpolation (and extrapolation) is adopted in the proposed schemes.

As can be seen, the main idea of the method is to find a proper smooth surface, which can produce the reflected image closely to the captured one in the experiment. In addition, in order to get the surface boundary information which can not be gained from reconstructed surface a two-dimensional boundary model is introduced as part of proposed reconstruction schemes and the whole weld pool surface can thus be reconstructed.

Interpolation reconstruction scheme (IRS) discussed in this chapter and extrapolation reconstruction scheme (ERS) in the next chapter are proposed according to above steps.

6.2 Notations and Definitions

In this section, some notations, geometrical glossaries and self-definitions used in this chapter are listed as below:

- Base point (points): The reflection point (points), whose position(s) is (are) assumed and used to calculate the positions of other reflection points as a base, is (are) called base point(s).
- Column plane: For a point $p_{i,j}$ located in the i^th^ row and the j^th^ column of the projected dot matrix, the plane passing through all the dots in the jth column and the dot of laser diode is called the column plane of point $p_{i,j}$.
- Center reference point: The center point in the projected dot matrix of

structured light. For a 19 by 19 dot matrix, it locates in the 10th row and the 10th column. It is not an actual visible point but a reference position, which can be used to find the corresponding relationship between projected and reflected points.

- GTAW: gas tungsten arc welding
- Normal: A normal to a flat surface is a three-dimensional vector which is perpendicular to that surface, and a normal to a non-flat surface at a point P on the surface is a vector which is perpendicular to the tangent plane to that surface at P.
- Reflected dots (points): The dots reflected on the imaging plane.
- Reflected image: The captured image including the reflected dots on the imaging plane.
- Reflection dots (points): The dots projected on the weld pool surface, also called projected dots.
- Row plane: For a point $p_{i,j}$ located in the ith row and the jth column of the projected dot matrix, the plane passing through all the dots in the ith row and the dot of laser diode is called the row plane of point $p_{i,j}$.
- Tangent plane: P is a point on the surface S. If the tangent lines at P to all smooth curves on the surface S passing through P lie on a common plane, then that plane is called the tangent plane to surface S at point P.
- Three-dimensional (3D) slope: The tangent plane of a point P on a surface S is also called the 3D slope of the point P.
- Two-dimensional (2D) slope: P is a point on the surface S and a plane T passing point P intercepts surface S to produce a curve. The tangent line of the curve at P is called the 2D slope of point P on surface S along the plane T.

6.3 Interpolation Reconstruction Scheme

As mentioned above, the interpolation reconstruction scheme is composed of two parts: slope-based surface reconstruction and two-dimensional boundary model. These two parts are discussed in the following sections and the reconstructed results are also shown.

6.3.1 Slope-based Surface Reconstruction Method

Figure 6-2 shows the flow chart for a slope-based reconstruction method proposed to reconstruct/estimate a surface from a given field of slope. It requires system parameters and processed reflected image as well as the corresponding relationship as inputs. As can be seen, the basic idea of the method is using slope information to compute/update the reflection points on pool surface and interpolate the surface based on the updated reflection points. Here two different algorithms have been proposed in interpolation reconstruction scheme (IRS) to compute the updated reflection points from a given slope field. They are edge-points algorithm (EPA) and one-point algorithm (OPA).

Under the assumption of one possible corresponding relationship, the projected (reflection) dot set P on the weld pool surface and its corresponding reflected dot set R on the imaging plane can be decided. As discussed before, they can be presented as $P = \{p_{i,j}, (i, j) \in S\}$ and $R = \{r_{i,j}, (i, j) \in I\}$. Here S and I present the weld pool surface and imaging plane respectively. The steps of the algorithm are described in detail below.

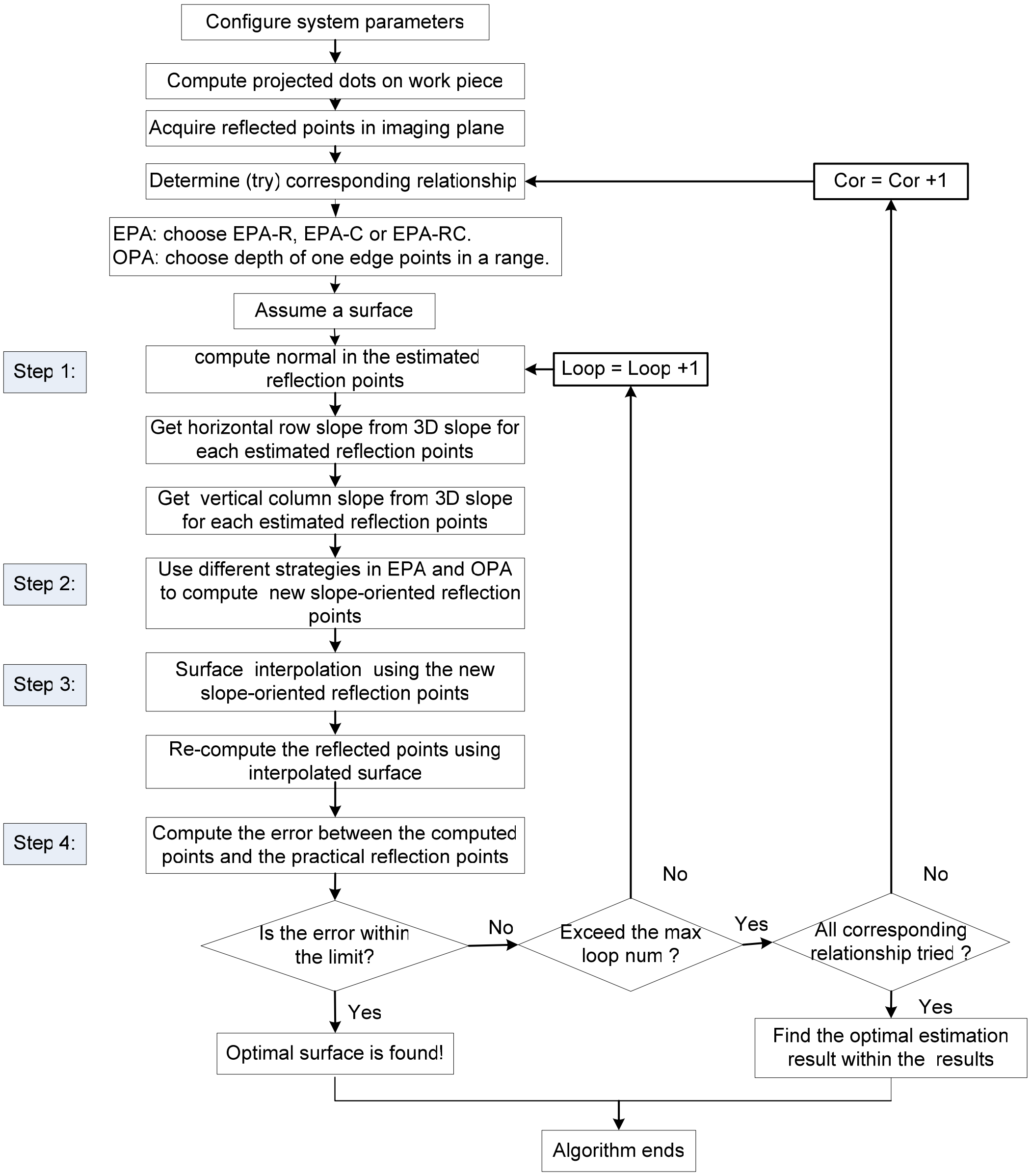

Figure 6-2, Flow chart of slope-based surface reconstruction method in IRS

Step 0: A flat plane (Z=0) is used as the initial estimate of the weld pool surface;

Step 1: Use the assumed surface to compute the slope field;

The estimate of the weld pool surface, or the initial estimate Z=0 plane for the first time, is used to calculate the positions of the estimated reflection dots $p'_{i,j}$ in set P' ($P' = \{p'_{i,j}, (i,j) \in S\}$) and thus all the reflected lines. By using the reflection law, the normal of every reflection point $p'_{i,j}$ on the surface can be computed from the corresponding incident and reflection line equations. Then tangent plane at the reflection dot $p'_{i,j}$ can be computed, which is referred as its 3D slope. This tangent plane intersects with the row plane and the column plane of dot $p'_{i,j}$. The resultant intersection lines are the two tangent lines along the planes and the 3D slope is decomposed into two 2D slopes: horizontal row and vertical column slopes. Thus the slope field of the surface at different reflection points is formed. The definitions of normal, tangent plane, row plane, column plane, 3D slope and 2D slope can be found in Section 6.2.

The 7 by 7 dot matrix in Figure 4-12 is also shown as an example of slope computation in Figure 6-3. Suppose point $p'_{4,4}$ is a point on the assumed surface S of weld pool. Based on the reflection law, it is easy to obtain its normal line and tangent plane K. The 3D slope at point $p'_{4,4}$ can be decomposed into row slope and column slopes, by intersecting its row plane $LP'_{4,1}P'_{4,7}$ and column plane $LP'_{1,4}P'_{7,4}$ with the plane K. As can be seen in Figure 6-3, line AB and CD are the resultant intersections and are thus the two 2D tangent lines. Their slopes in plane $LP'_{4,1}P'_{4,7}$ and $LP'_{1,4}P'_{7,4}$ are the two 2D slopes of point $p'_{4,4}$ in the vertical and horizontal direction respectively.

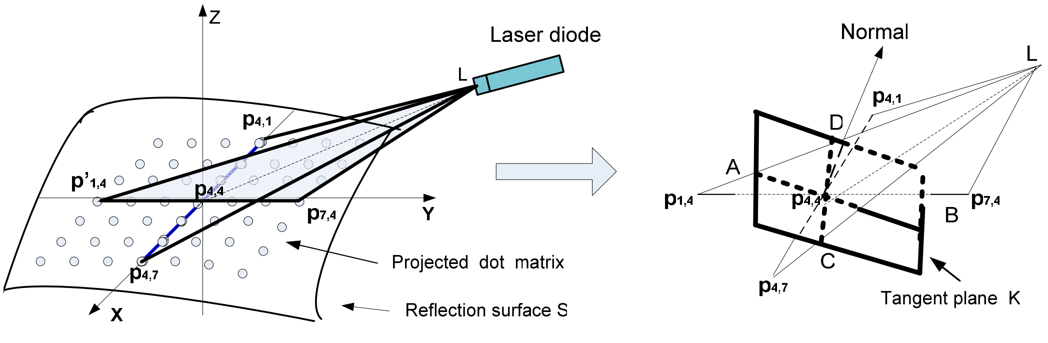

Figure 6-3, 3D slope decomposed into two 2D slopes

Step 2: Compute the new slope-oriented reflection points based on the slope field;

Since the shape of the weld pool surface is shallow, it is reasonable to take the computed slopes at estimated P' as the slopes of the actual reflection points

P on weld pool surface. Since the estimated surface in the first step can not meet the slope requirements to produce the reflected image, the positions of new slope-oriented reflection point set P'' ($P'' = \{p''_{i,j}, (i,j) \in S\}$) is calculated by using these estimates of slopes in the second step.

The position of slope-oriented reflection point $p''_{i,j}$ can be determined by either estimated row slopes in its row plane or column slopes in its column plane. Here the same example in Figure 4-12 is taken and sequential row and column corresponding relationships are assumed. Suppose the reflected image is obtained as Figure 4-12 (b) and the corresponding projected point of reflected point $r_{3,4}$ is $p'_{4,4}$. The row plane/column plane of point $p'_{4,4}$ and the computed 2D slopes of the reflection points in its row/column are presented in Figure 6-4 respectively. As can be seen, different 2D coordinate systems are taken in the row/column plane regarding to the computed row/column slopes.

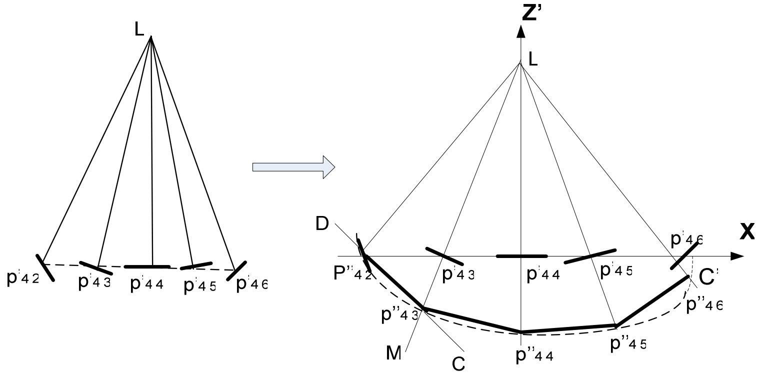

(a) Row plane of point p'44

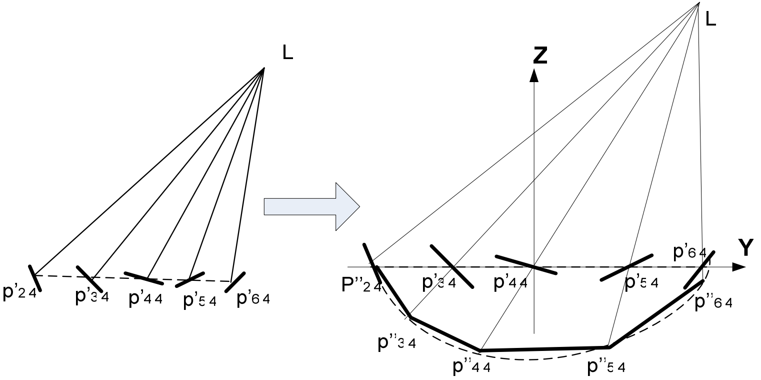

(b) Column plane of point p'44

Figure 6-4, Computation of slope-oriented points

In Figure 6-4 (a), the row slopes of the points in the 4th row on the assumed surface have been computed in the first step. If the weld pool surface is flat, these slopes must be zero. Non-zero slopes indicate that these points on a flat surface should be replaced by better estimates of slope-oriented reflection points located on their incident rays and the new estimates $p''_{i,j}$ should be so determined that they can better meet the constraints given the slopes. To obtain the new slope-oriented points ($p''_{4,3}$, $p''_{4,4}$, $p''_{4,5}$ and $p''_{4,6}$), select the edge point $p''_{4,2}$ as a base point. In order to find the position of $p''_{4,3}$, the directions of line CD should be found firstly, then $p''_{4,3}$ can be got as the intersection points of the incident ray LM and the line CD since the reflection point on weld pool surface must be also on its incident ray. In order to simplify the computation the line direction of adjacent points is set to be the average value of the two points' row slopes under the assumption of the dense projected dot matrix. For instance, the direction of CD can be computed as Eq.6-1.

$$S_{CD} = sign(S_{p'_{4,2}}) \times \left| \left(S_{p'_{4,2}} + S_{p'_{4,3}} \right) / 2 \right| \quad \text{.... (Eq.6-1)}$$

where $S_{p'_{4,2}}$ and $S_{p'_{4,3}}$ present the row slopes of point $p'_{4,2}$ and $p'_{4,3}$, and $sign(S_{p'_{4,2}})$ refers to the sign of row slope of point $p'_{4,2}$. Follow the same procedures, the other slope-oriented reflection points in the same row are computed and the dash curve in Figure 6-4 (a) indicates the possible profile of weld pool surface. In the same way, the column slopes can also be used to compute the new slope-oriented reflection points as shown in Figure 6-4 (b).

As can be seen, the positions of slope-oriented reflection points are measured in relation to the base point or points, such as point $p''_{4,2}$ in Figure 6-4 (a). In order to determine the actual positions in the universal coordinate systems, the absolute position/positions of the base point/points should be decided. Two algorithms, called edge-points algorithm (EPA) and one-point algorithm (OPA), have been developed with different position assumptions. Considering the continuity of the rows, the absent center reference point in the captured image is also added as a reflected point to compute in the proposed algorithms and its position is set as the center of its two adjacent dots in the same row .

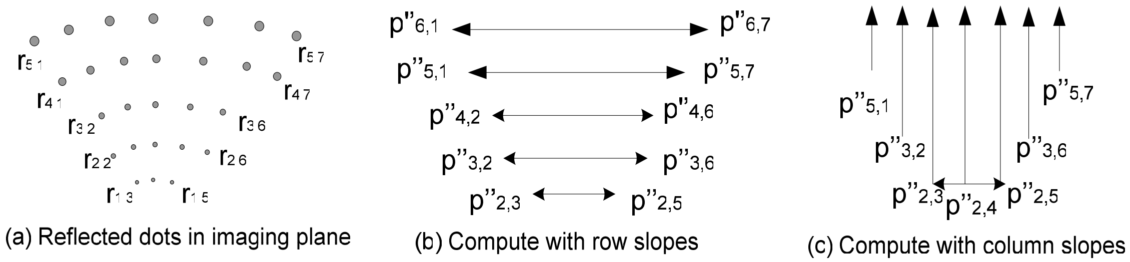

(a) Reflected dots in imaging plane (b) Compute with row slopes (c) Compute with column slopes

Figure 6-5, EPA algorithm illustration

- Edge-points algorithm (EPA)

In EPA, the initial depths of the edge base points on reflection surface are assumed to be zero. Hence, in the first loop of algorithm the depths of several edge points, for example in Figure 6-5 (b) (c) the Z coordinate of edge reflection points $p''_{i,j}$ (except $p''_{2,4}$) corresponding to edge reflected points $r_{i,j}$ in Figure 6-5 (a), are set to be zero. In the followed loops, the computed positions of edge base points in the previous loop are used. Here edge points are referred to the points at the end of each row, which are projected to or reflected from the edge of the weld pool surface. The assumption is based on the experimental observation that the edge reflected points of row are on the imaging plane, but the edge reflected dots of column may be blocked by the torch.

To calculate the positions of slope-oriented points using the slope field, the EPA-R algorithm can be used where R stands for “row”. It uses horizontal row slopes computed in the first step and the positions of edge base points to calculate the positions of other points on the reflection surface, shown in Figure 6-5 (b). Since two end points in each row can be considered edge points and be used as the base points, there are two possible new positions for each reflection point on the row. We use the average value of the positions as the position for the new slope-oriented point. Similarly, the column slopes may also be used and the resultant method is referred to as the EPA-C algorithm where C stands for “Column” as shown in Figure 6-5 (c). In this algorithm, if the base point for the column is not an edge base point, its position should be firstly computed by the horizontal row slopes in the EPA-R, such as the point $p''_{2,4}$. Obviously a third method is to use the average value of above two methods to calculate, which can be referred to as EPA-RC algorithm. In the Section 6.4, these methods will be tested for comparison.

- One-point algorithm (OPA)

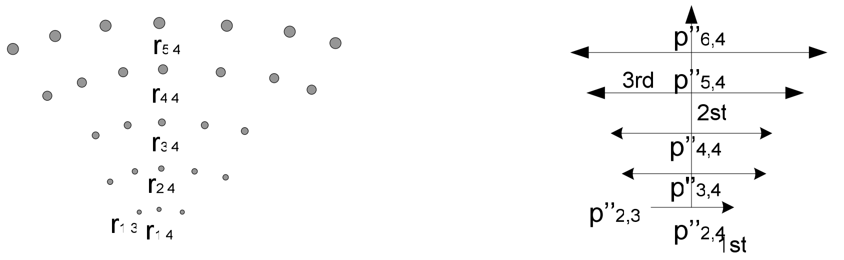

(a) Reflected dots in imaging plane (b) Compute with row and column slopes

Figure 6-6, OPA algorithm illustration

In OPA, the depth of one edge (base) point on reflection surface is assumed a value in a range around zero in each loop, such as from -0.5 mm to 0.5 mm. All the other reflection points are calculated based on it. For example, in Figure 6-6 (b) the depth of the reflection points $p''_{2,3}$ corresponding to $r_{1,3}$ is assumed to be around zero, and the position of slope-oriented reflection points in the same row is calculated using row slopes. Then the position of center point $p''_{2,4}$ and the column slopes are used to compute the positions of other center points in different rows, such as $p''_{3,4}$, $p''_{4,4}$, $p''_{5,4}$ and $p''_{6,4}$. At last, based on the center reflection points, all other reflection points' position can be calculated by using row slopes.

Step 3: Reconstruction of weld pool surface using reflection points;

In the third step, a weld pool surface should be deduced depending on the slope-oriented reflection points P'' computed in the second step. Here a existing triangle-based cubic interpolation method [61] is applied to reconstruct the smooth weld pool surface, which can produce a surface from non-uniformly sampled data in the form of

$$z = f(x, y) \quad \text{…. (Eq.6-2)}$$

Step 4: Compute the error of the interpolated surface.

In the fourth step, with the knowledge of the projected dot matrix and the surface reconstructed from the third step, the reflected points set R' ($R' = \{r'_{i,j}, (i,j) \in I\}$) on the imaging plane can be re-computed and compared with the positions of the reflected points R on the captured image. The differences between the actual and computed reflected points can be calculated. This error can be further mapped to the weld pool surface and denoted as “reflection error”. If the reflection error is within the pre-specified threshold, an acceptable estimate of weld pool surface is found and the reconstruction ends. Otherwise, this estimated surface is used as the new initial surface to continue the first step within pre-set number of loops. If the surface reconstructed converges but the reflection error is greater than the threshold, the surface with the minimum error is chosen.

To define a meaningful error which can describe the difference between the calculated and actual reflection points on weld pool surface, the authors propose two error measurement parameters: average reflection error (ARE) and maximum reflection error (MRE).

$$ARE = \sum_{(i,j)\in I} E_{i,j} \Big/ n, \ldots (i,j) \in I \quad \text{…. (Eq.6-3)}$$

$$MRE = \max\{E_{i,j}, (i,j) \in I\} \quad \text{…. (Eq.6-4)}$$

where I refers to the reflected image and n present the total number of the reflected points on imaging plane. $E_{i,j}$ presents the reflection error of the reflection (projected) point corresponding to reflected point $r_{i,j}$ and it is defined as:

$$E_{i,j} = \sqrt{\left(e^x_{i,j} \cdot \frac{W_p}{W_r}\right)^2 + \left(e^z_{i,j} \cdot \frac{L_p}{L_r}\right)^2} \quad \text{…. (Eq.6-5)}$$

where $e^x_{i,j}$ and $e^z_{i,j}$ are the absolute values of distance between estimated reflected point $r'_{i,j}$ and actual reflected point $r_{i,j}$ along horizontal direction (X axis) and vertical direction (Z axis) respectively.

$$e^x_{i,j} = \left| r'^x_{i,j} - r^x_{i,j} \right|,\ e^z_{i,j} = \left| r'^z_{i,j} - r^z_{i,j} \right|, \text{ where } r'_{i,j} \in R',.r_{i,j} \in R \qquad \text{.... (Eq.6-6)}$$

As shown in Figure 6-7, W_r and L_r present the horizontal and vertical range of the reflected dots, and W_p and L_p present the horizontal (X axis) and vertical (Y axis) range of the corresponding projected dots on the work piece (Z=0). These parameters are formulated as:

$$W_p = \max\left(p^x_{m,n}\right) - \min\left(p^x_{m,n}\right),$$

$$L_p = \max\left(p^y_{m,n}\right) - \min\left(p^y_{m,n}\right), \text{ where } p_{m,n} \in P \qquad \text{... (Eq.6-7)}$$

$$W_r = \max\left(r^x_{i,j}\right) - \min\left(r^x_{i,j}\right),$$

$$L_r = \max\left(r^z_{i,j}\right) - \min\left(r^z_{i,j}\right), \text{ where } r_{i,j} \in R \qquad \text{... (Eq.6-8)}$$

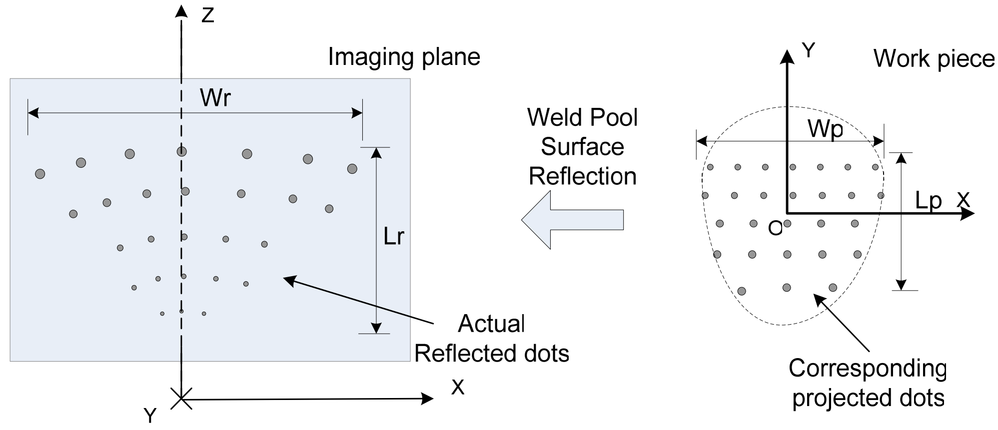

Figure 6-7, Illustration of the design of error measurement parameters

From Eq.6-3 to Eq.6-8, it can be seen that the defined ‘reflection error presents the estimation error of the reflection points on weld pool surface, which is mapped from the error of reflected dots on imaging plane. In Eq.6-5, the first part uses the ratio W_p/W_r to map the horizontal error of reflected dot to that of reflection dot, and in the same way the second term uses L_p/L_r to get the vertical error of reflection dot. Thus it is reasonable to use reflection error to evaluate the error of calculated 3D reflection points on weld pool surface based on 2D difference between computed and actual reflected dots on imaging plane.

6.3.2 Two-dimensional Boundary Modeling

Although the basic shape of the three-dimensional surface can be extracted from the reflected image, the boundary of the weld pool may not be directly determined. It is not guaranteed that each row of laser rays has rays be projected exactly on the boundary. Hence, in addition to the issue how the boundary of the weld pool is mathematically described, it is also an issue how boundary points can be derived from a reflected image. While a few approaches have been proposed to describe weld pool boundaries [62] [63], we here propose a two-dimensional piecewise boundary model which can be derived from the reflected image.

6.3.2.1 Determination of boundary points

As mentioned earlier, in the system the projected dot matrix covers the whole possible weld pool surface region and all the dots located within the scope will be reflected by the specular surface. Hence, it is reasonable to believe that on the reflected images two end points on each curved row are reflected from small neighborhoods of the two sides of the weld pool boundary, and they can be considered as "conservative estimates of edge reflection points", which are presented as $P^e = \{p^e{}_{i,j}, (i, j) \in B\} \subset P$. Here B is referred to the boundary and the subscripts present the row and column number of the edge points.

Further, for the head of the weld pool where the boundary divides the weld pool from unmelted material, the boundary of the weld pool surface is on the X-Y plane (Z=0), i.e., on the work piece surface. For the rear of the weld pool surface in GTAW, it is also reasonable to consider that the weld pool boundary is on the X-Y plane if no filler metal is used and the joint is square joint with no gap as in this study. With this reasonable assumption, once the center reference point and corresponding relationship are found, the positions of the "conservative estimates of edge points" in set P^e can be decided on the work piece. Denote the projection of P^e on the work piece as $(X,Y)|_{P^e}$. These points $(X,Y)|_{P^e}$ on the work piece can be divided into left and right sides regarding to X-Y coordinates, just as shown in Figure 6-8 (a). Here the experimental case in Figure 3-17 is used as an example.

It is apparent that the boundary of weld pool surface is not exactly passing P^e but somewhere outside $(X,Y)|_{P^e}$. To illustrate how to decide the better estimates of boundary points from conservative estimates $(X,Y)|_{P^e}$, Figure 6-8 is used. As can be seen in Figure 6-8 (a), there is a right edge reflection point A $\subset (X,Y)|_{P^e}$ and its right neighbor point B in X axis and an actual "boundary point" Q should be located between A and B. Suppose the position Q (X_q) is a variant evenly distributed in the range (x_a, x_b). According to the knowledge of probability, its mean and variance can be calculated as Eq.6-9.

$$E(X_q) = (x_a + x_b)/2 \ , \ D(X_q) = (x_b - x_a)^2/12 \qquad \text{..... (Eq.6-9)}$$

If one chooses $X_q = k$ ($x_a<k<x_b$), the mean square error (MSE) is

$$MSE = E\left[(X_q - k)^2\right] = 1\Big/(x_b - x_a) \cdot \int_{x_a}^{x_b} (X_q - k)^2 dX_p \qquad \text{..... (Eq.6-10)}$$

In order to make the MSE minimized, the requirement of Eq.6-11 should be met.

$$\frac{\partial MSE}{\partial k} = 0 \qquad \text{..... (Eq.6-11)}$$

From Eq.6-10 and Eq.6-11, the optimal k is calculated as

$$k = (x_a + x_b)/2 = E(X_q) \qquad \text{..... (Eq.6-12)}$$

Hence, the optimal estimation of boundary point Q is the middle point of point A and B. Based on the positions of edge reflection points P^e in X-Y plane, the positions of boundary points are determined, which form point set D as shown in Figure 6-8 (b).

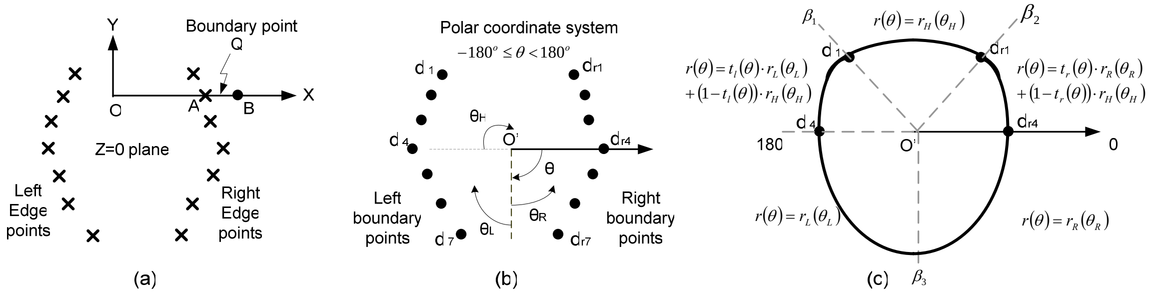

Figure 6-8, Boundary modeling illustration (a) Edge reflection points in universal coordinate system (b) Estimated boundary points in polar coordinate system (c) 2D boundary piecewise model

6.3.2.2 Weld pool boundary fitting

In Figure 6-8 (b) only the positions of the boundary points on two sides of the weld pool are known. Divide the weld pool boundary points in set D into left and right parts. The left points are marked with $d_{l1}, d_{l2}...d_{li}...d_{l7}$ and the right points are marked with $d_{r1}, d_{r2}...d_{ri}...d_{r7}$. A polar coordinate system is set up for the weld pool boundary modeling and the origin point O' is chosen in the middle point of the widest boundary point pairs in a row, such as the pair of d_{l4} and d_{r4} in Figure 6-8 (b). The direction of angle θ in polar coordinate system is clockwise shown in the figure. The universal coordinates of all the boundary points in set D should be converted into established polar coordinates (l, θ) and the angle parameter θ ranges from $-180°$ to $180°$. Then the pool boundary can be modeled by relating the radius l to the angle θ in the polar coordinate system.

In the study, the weld pool boundary is segmented into three parts: left, right and head. The head part is introduced to fit the actual size of weld pool surface and make left and right parts merged smoothly. The following polar coordinate model is used to describe the three parts of the weld pool boundary.

$$r(\theta) = \omega_0 + \sum_{i=1}^{p} \left(\omega_i \cdot \theta^p \right) \qquad \text{..... (Eq.6-13)}$$

where p is the order of the fitted equation. Usually the higher the order is, the more precise the model is. Considering the balance between computation complexity and accuracy, 3rd order is selected in the model.

The available boundary points in set D can be assigned into three sets used for left, right and head segment boundary fitting. They are presented as point set L, R and H.

$$L = \left\{ \left(l_i , \theta_{l_i} \right) \middle| 90^\circ \le \theta_{l_i} \le 180^\circ or -180^\circ < \theta_{l_i} \le -90^\circ, \left(l_i , \theta_{l_i} \right) \in D \right\}$$

$$R = \left\{ \left(r_i , \theta_{r_i} \right) \middle| -90^\circ < \theta_{r_i} < 90^\circ, \left(r_i , \theta_{r_i} \right) \in D \right\}$$

$$H = \left\{ \left(h_i , \theta_{h_i} \right) \middle| -180^\circ \le \theta_{h_i} \le 0^\circ, \left(h_i , \theta_{h_i} \right) \in D \right\} \qquad \text{.... (Eq.6-14)}$$

In order to make model continued in their segments, the angle parameter θ of boundary points in Eq.6-14 are replace by θ_L , θ_R and θ_H respectively for different parts modeling. From Figure 6-8 (b), the relationships between them are derived.

$$\begin{cases} \theta_L = \begin{cases} \theta - 90^\circ ....when..........90^\circ \le \theta \le 180^\circ \\ \theta + 270^\circ ....when...-180^\circ < \theta \le -90^\circ \end{cases} ...in..L \\ \theta_R = 90^\circ - \theta ....in..R \\ \theta_H = \theta + 180^\circ ....in..H \end{cases} \qquad \text{.... (Eq.6-15)}$$

Then the three segments of the weld pool boundary are modeled as shown in Eq.6-16.

$$\begin{cases} r_L\left(\theta_L\right) = \omega_{L0} + \sum_{i=1}^{p} \left(\omega_{Li} \cdot \theta_L{}^{p} \right) = \left(\omega_{L0} \quad \omega_{L1} \quad \omega_{L2} \quad \omega_{L3} \right) * \left(1 \quad \theta_L \quad \theta_L{}^2 \quad \theta_L{}^3 \right)^T \\ r_R\left(\theta_R\right) = \omega_{R0} + \sum_{i=1}^{p} \left(\omega_{Ri} \cdot \theta_R{}^{p} \right) = \left(\omega_{R0} \quad \omega_{R1} \quad \omega_{R2} \quad \omega_{R3} \right) * \left(1 \quad \theta_R \quad \theta_R{}^2 \quad \theta_R{}^3 \right)^T \\ r_H\left(\theta_H\right) = \omega_{H0} + \sum_{i=1}^{p} \left(\omega_{Hi} \cdot \theta_H{}^{p} \right) = \left(\omega_{H0} \quad \omega_{H1} \quad \omega_{H2} \quad \omega_{H3} \right) * \left(1 \quad \theta_H \quad \theta_H{}^2 \quad \theta_H{}^3 \right)^T \end{cases} \quad \text{. (Eq.6-16)}$$

To find the proper coefficients for above model, least square method is chosen to estimate them by applying the boundary points in set L, R and H respectively. The criterions used for determination can be express as:

$$\omega_{Li}(i=0,1,2,3): \min\sum_{j=1}^{N_l}\left(l_j - r_L(\theta_{Lj})\right)^2 = \min\sum_{j=1}^{N_l}\left[l_j - (\omega_{L0} \quad \omega_{L1} \quad \omega_{L2} \quad \omega_{L3})\cdot\left(1 \quad \theta_{Lj} \quad {\theta_{Lj}}^2 \quad {\theta_{Lj}}^3\right)^T\right]^2$$

$$\omega_{Ri}(i=0,1,2,3): \min\sum_{j=1}^{N_r}\left(r_j - r_R(\theta_{Rj})\right)^2 = \min\sum_{j=1}^{N_r}\left[r_j - (\omega_{R0} \quad \omega_{R1} \quad \omega_{R2} \quad \omega_{R3})\cdot\left(1 \quad \theta_{Rj} \quad {\theta_{Rj}}^2 \quad {\theta_{Rj}}^3\right)^T\right]^2$$

$$\omega_{Hi}(i=0,1,2,3): \min\sum_{j=1}^{N_h}\left(h_j - r_H(\theta_{Lj})\right)^2 = \min\sum_{j=1}^{N_h}\left[h_j - (\omega_{H0} \quad \omega_{H1} \quad \omega_{H2} \quad \omega_{H3})\cdot\left(1 \quad \theta_{Hj} \quad {\theta_{Hj}}^2 \quad {\theta_{Hj}}^3\right)^T\right]^2$$

.... (Eq.6-17)

where N_l, N_r and N_h are the number of points in set L, R and H. By using the standard least square method the parameters ω_{Li}, ω_{Ri} and $\omega_{Hi}(1 \le i \le 3)$ can be solved.

After solving Eq.6-17, the equations for three segments of the weld pool boundary are gained, but they are not smoothly connected. Therefore in the proposed 2D piecewise boundary model, the boundary is further divided into five parts by adding two transition areas between head segment and the other two segments, which is shown in Figure 6-8 (c). Then the whole boundary of the weld pool $r(\theta)$ is calculated using the following equations:

$$r(\theta) = r_H(\theta_H) = r_H(\theta + 180°) \qquad \beta_1 \le \theta \le \beta_2$$

$$r(\theta) = t_l(\theta)\cdot r_L(\theta_L) + (1 - t_l(\theta))\cdot r_H(\theta_H) = t_l(\theta)\cdot r_L(\theta + 270°) + (1 - t_l(\theta))\cdot r_H(\theta + 180°)$$

$$-180 < \theta < \beta_1$$

$$r(\theta) = r_L(\theta_L) = r_L(\theta - 90°) \qquad \beta_3 \le \theta \le 180$$

$$r(\theta) = t_r(\theta)\cdot r_R(\theta_R) + (1 - t_r(\theta))\cdot r_H(\theta_H) = t_r(\theta)\cdot r_R(90° - \theta) + (1 - t_r(\theta))\cdot r_H(\theta + 180°)$$

$$\beta_2 < \theta < 0$$

$$r(\theta) = r_R(\theta_R) = r_R(90° - \theta) \qquad 0 \le \theta < \beta_3$$

……. (Eq.6-18)

where $t_l(\theta)$ and $t_r(\theta)$ are the weights, which are defined as:

$$t_l(\theta) = (\beta_1 - \theta)/(\beta_1 + 180°) \qquad -180 < \theta < \beta_1$$

$$t_r(\theta) = 1 - \theta/\beta_2 \qquad \beta_2 < \theta < 0$$

……. (Eq.6-19)

where β_1, β_2, $0°$, $180°$ and β_3 are the boundaries for the segments. β_1 is define as the largest angle of the boundary point among $\left(-180^\circ,-90^\circ\right)$ in set L; β_2 is define as the smallest angle of the point in set R; and β_3 is the intersection angle of left segment $r_L\left(\theta_L\right)$ and right segment $r_R\left(\theta_R\right)$, which is the rear angle of the weld pool.

6.4 Results and Discussion

MATLAB is used to implement the proposed interpolation reconstruction scheme (IRS). Proposed slope-based surface reconstruction algorithms rebuild the middle weld pool surface area which reflects the projected laser dots onto the imaging plane, and the established two-dimensional boundary model helps us to find the weld pool boundary. Combined with information of the middle part and boundary part, the whole weld pool surface can be reconstructed by interpolation again. That means the optimal estimated reflection points and the modeled boundary points can be used together to do interpolations so as to reconstruction the whole weld pool surface.

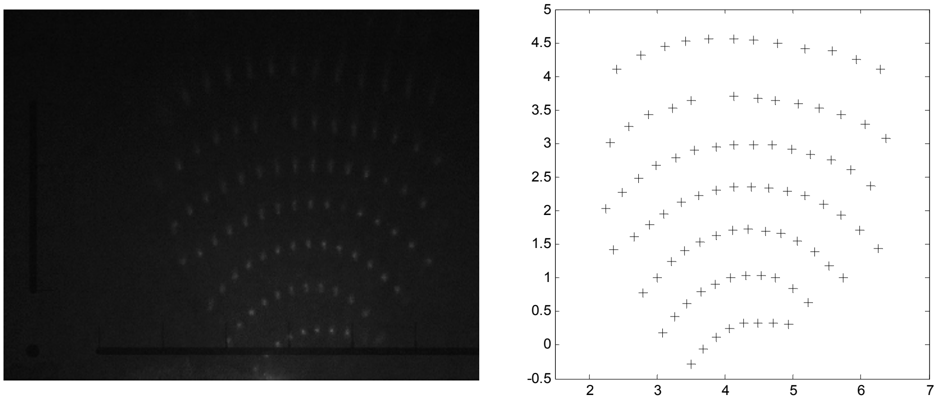

(a) Original reflected image (b) Extracted reflected dots

Figure 6-9, Reflected Image Processing

A reflected image captured during the experiment is used to test the slope-based reconstruction method, which is shown in Figure 6-9 (a). The reflected dots extracted using image processing algorithms are shown in Figure 6-9 (b). Two algorithms (EPA and OPA) in interpolation reconstruction scheme (IRS) are tested in our study using the reflected image above, and their results are shown.

It can be seen from Figure 6-2 the purpose of setting the error threshold in step 4 is to expedite the algorithm, thus it is not used in the experiments here in order to find the optimal result within pre-set loops.

6.4.1 EPA algorithm result

Since the actual shape of weld pool surface can not be measured directly, the error of the reconstructed surface is measured by the two indirect error measurement parameters proposed in Section 6.3.1: average reflection error (ARE) and maximum reflection error (MRE). For the reflected image in Figure 6-9 (a), some related dimension parameters in Eq.6-3 are calculated as below:

$W_r = 40.1749\,\mathrm{mm}$, $L_r = 47.2475\,\mathrm{mm}$;

$W_p = 6.1537mm$, $L_p = 4.5240mm$ (for I/I and S/I corresponding relationships);

$W_p = 6.6688mm$, $L_p = 5.4117mm$ (for S/S corresponding relationship).

As can be seen, the value of W_p and L_p change a little for different row corresponding relationships. These results are the same for OPA algorithm.

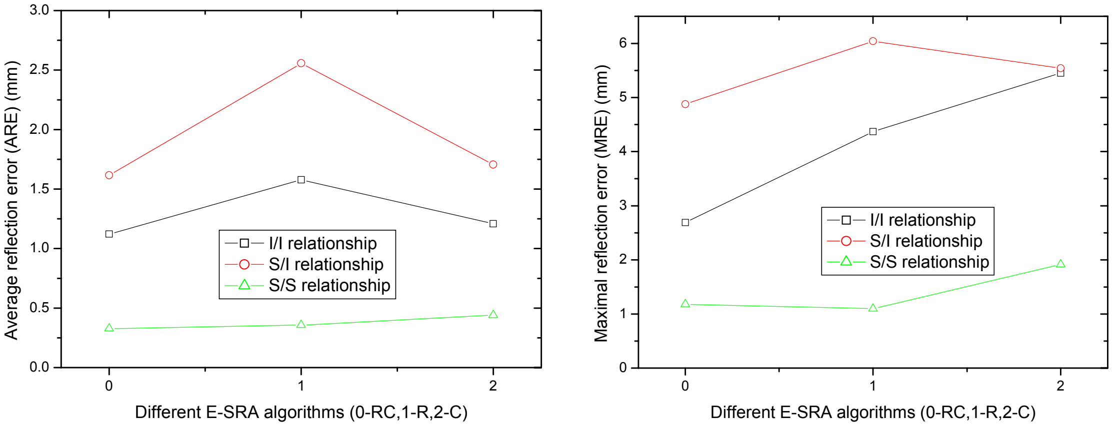

Figure 6-10, Results of EPA algorithms (a) Average Reflection Error (left) (b) Maximal Reflection Error (right).

Figure 6-10 shows the experimental results of the EPA algorithms under different situations and here 100 loops are tried for each situation. The horizontal axis presents different methods used to compute the reflection points: 0 for EPA-RC, 1 for EPA-R and 2 for EPA-C. Three possible corresponding relationships discussed in section 4.2.2.3 are all considered in order to improve the veracity and compatibility of the algorithms. Here the symbol ‘S’ presents sequential and ‘I’ presents inverse, and the first letter in front of ‘/’ presents column corresponding relationship and the second after ‘/’ presents row corresponding relationship.

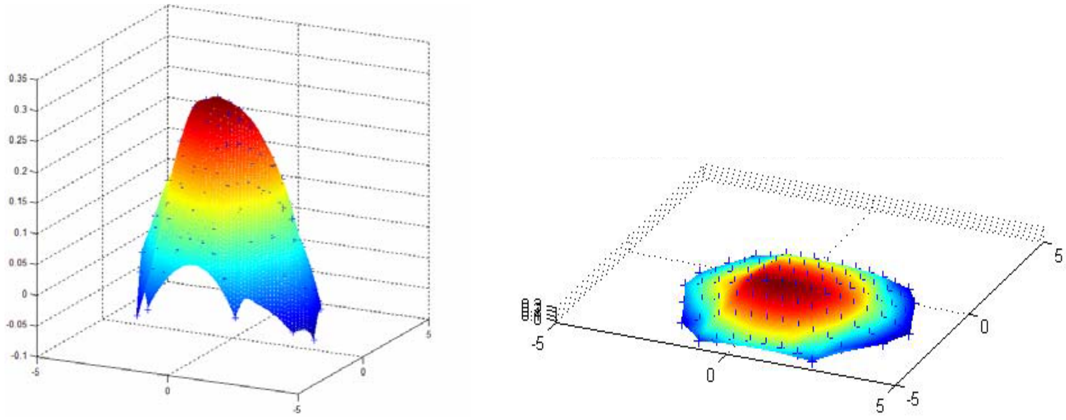

(a) Close view (Z axis is amplified) (b) View with equal axes

Figure 6-11, Optimal weld pool surface reconstructed by EPA algorithms

As can be seen in Figure 6-10, EPA algorithms can effectively differentiate different corresponding relationships and the S/S corresponding relationship can achieve better result. Comparing among different ways to use the slopes in Figure 6-10 (a), the performance of EPA-RC is a little better than the other two and the minimal average reflection error (ARE) is 0.3271 mm. The minimal MRE 1.0976 mm is achieved by EPA-R. Here the ARE is considered as the primary standard to get the interpolated optimal weld pool surface, which is shown in Figure 6-11. It is a deformed convex surface and the most part of weld pool surface is reconstructed by the algorithm.

In Figure 6-12, the positions of actual reflection points and computed reflected points using interpolated surface by EPA algorithm are shown. As can be seen, their difference or the error is not small and especially large in neighborhood of the edge. It should be noticed that the absent center reference point in the captured image is also shown as a reflected point, and its position is set at the center of its adjacent dots in the same row.

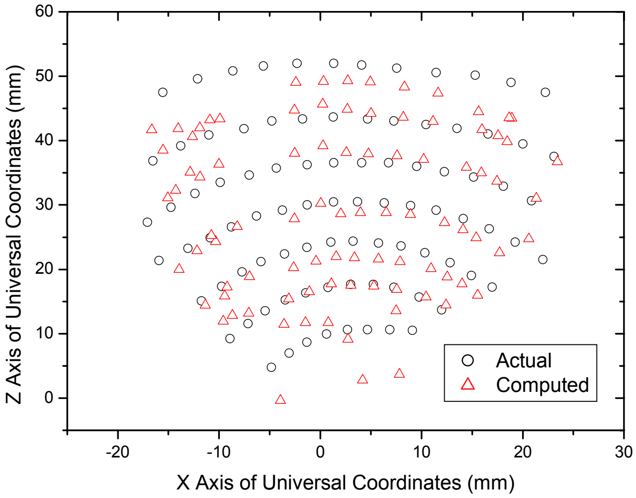

Figure 6-12, Computed and actual reflection points compare on imaging plane (EPA)

6.4.2 OPA algorithm result

In OPA algorithm, the depth (height) of one edge (base) reflection point on work piece plane, which is corresponding to the point in left-down corner on the image, is set and its X-Y coordinates are decided accordingly on the incident ray. Then the other reflection points are calculated based on it. Figure 6-13 shows the minimal average reflection error (ARE) and maximum reflection error (MRE) of OPA algorithm under different situations and 100 loops are tried for each situation. The height of the base edge point is changed from -0.5mm to 0.5mm, which is reasonable for practical applications.

In Figure 6-13 the performances of different corresponding relationships can be easily differentiated and S/S corresponding relationship makes better result, which also proved the validity of OPA algorithm. For average reflection error (ARE), the minimal value 0.1691 mm is achieved when the height is 0 mm with S/S relationship. In Figure 6-13 (a), there is only a little difference among the results under different assumptions, and this may be caused by the small difference between assumed depths (only 0.1 mm). Figure 6-13 (b) also verifies the S/S relationship has the better performance for maximal reflection error (MRE), and the minimal MRE is 0.8671 mm when height is -0.2 mm.

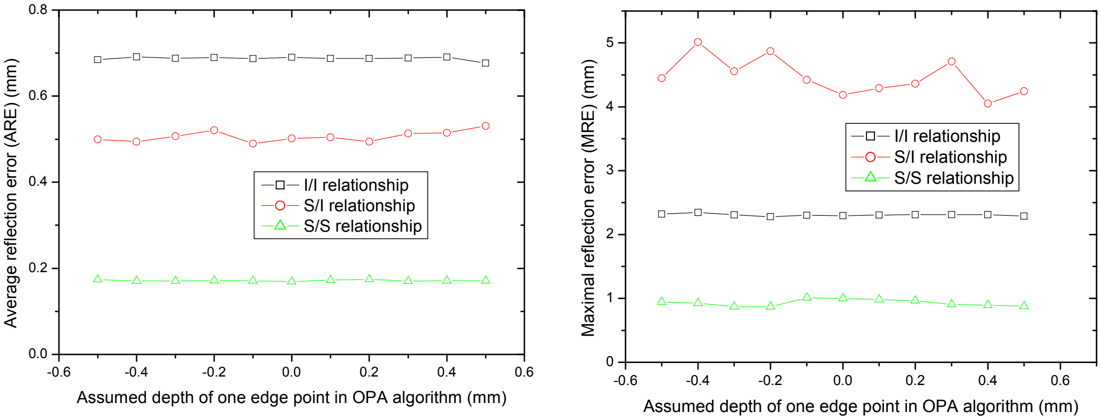

Figure 6-13, Results of OPA algorithm (a) Average Reflection Error (left) (b) Maximal Reflection Error (right)

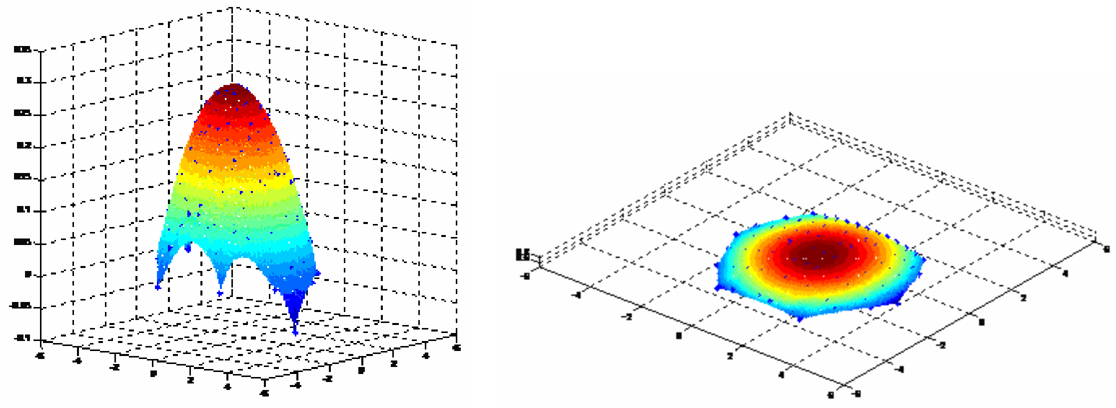

(a) Close view (Z axis is amplified) (b) View with equal axes

Figure 6-14, Optimal interpolated weld pool surface reconstructed by OPA algorithm

Here ARE is taken as the primary standard, and the optimal interpolated weld pool surface with marked reflection points is shown in Figure 6-14. As can be seen, the reconstructed surface is a shallow smooth convex surface and is rebuild in most part.

In Figure 6-15, the positions of actual reflection points and computed reflected points using optimal interpolated surface are shown. The difference between them is small in the middle part, but larger for the edge points because the slopes of the edge points are not precise enough for interpolation method.

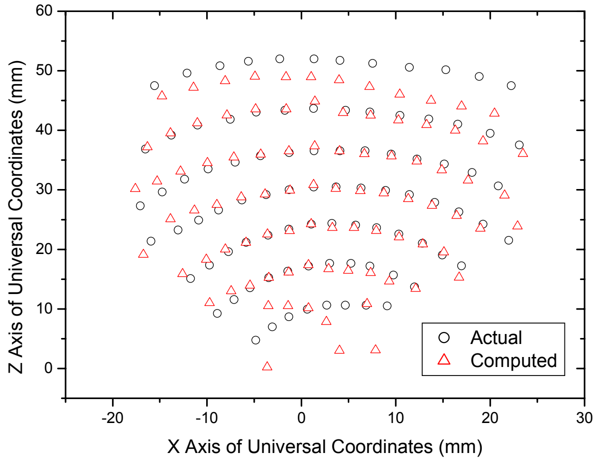

Figure 6-15, Computed and actual reflection points compare (OPA)

Moreover the average reflection error of inside points (ARE-I) in the middle part and maximum reflection error of inside points (MRE-I) are also defined and evaluated in Figure 6-16 by eliminating the influence of the edge points' large errors caused by the interpolation method. In this example, the edge points refer to the reflection points corresponding to the reflected points in the 1st and 7th row and on both ends of each row in Figure 6-15. The optimal interpolated weld pool surface is also achieved by using S/S corresponding relationship with depth 0 and the same result is shown in Figure 6-14. As can be seen, the minimal average reflection error of inside points (ARE-I) is 0.0786 mm, which is much less than the minimal ARE for all the reflected points in Figure 6-13 (a). The minimal MRE-I 0.2169 mm is also much less than the result in Figure 6-13 (b).

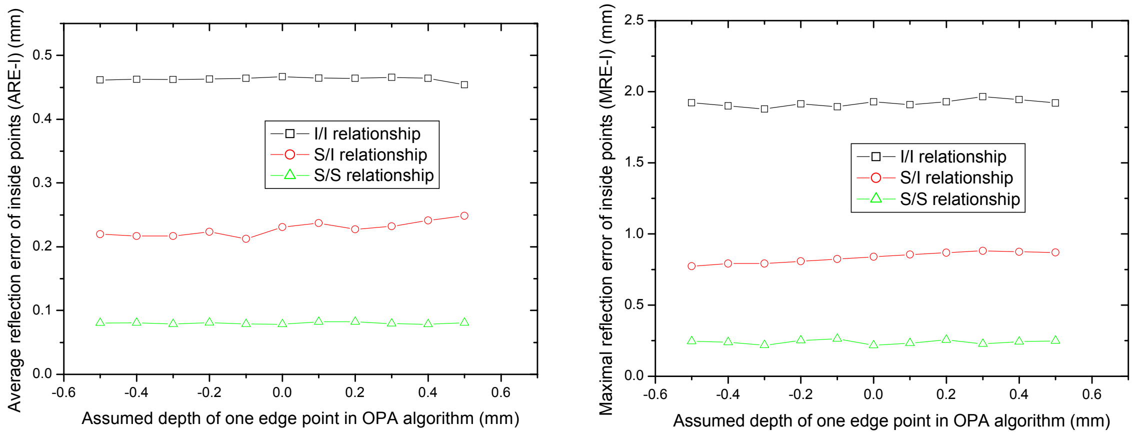

Figure 6-16, Results of OPA algorithm (a) ARE-I (left) (b) MRE-I (right)

6.4.3 Algorithms comparison

Above results show EPA and OPA algorithms in interpolation reconstruction scheme can achieve some similar results in reconstructing the weld pool surface. For the studied reflected image in Figure 6-9, the reconstructed weld pool surfaces by two algorithms are both convex, which agree with the eye direct observation result. The heights of the weld pool surfaces are both around 0.3 mm.

According to the errors of the algorithms, it is obvious OPA algorithm has better performance than EPA. The minimal ARE and MRE of OPA algorithm is smaller and the interpolated weld pool surface is smoother than the results of EPA algorithm. The possible reason is the assumption of one edge point position in OPA algorithm is more reasonable.

6.4.4 Boundary models and reconstructed results

By using slope-based surface reconstruction method, the interpolated optimal weld pool surfaces are reconstructed in Figure 6-11 and Figure 6-14. As can be seen, only the middle area of the weld pool surface covered by the dot matrix is rebuilt. The 2D boundary model described in Section 6.3.2 is thus used to find the boundary of the weld pool surface.

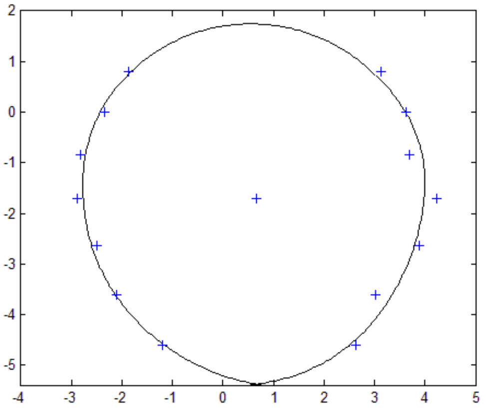

Figure 6-17, Fitted two-dimensional weld pool boundary model (on Z=0 plane)

Based on the results of slope-based reconstruction method, the S/S corresponding relationship and the reflected dots on imaging plane are used to find the boundary points. Figure 6-17 shows the boundary points of the pool surface on work piece (Z=0 plane) and the fitted two-dimensional (2D) boundary by using the proposed modeling method. The center point is the origin of the used polar coordinate system. The shape of the modeled 2D boundary is similar as the ones shown in Figure 1-1. Because the welding speed is slow (3mm per second), the difference between width (6.7313mm) and length (7.1182mm) is small and the 2D shape of weld pool likes a circle, which can be verified by the measurement result after the experiment.

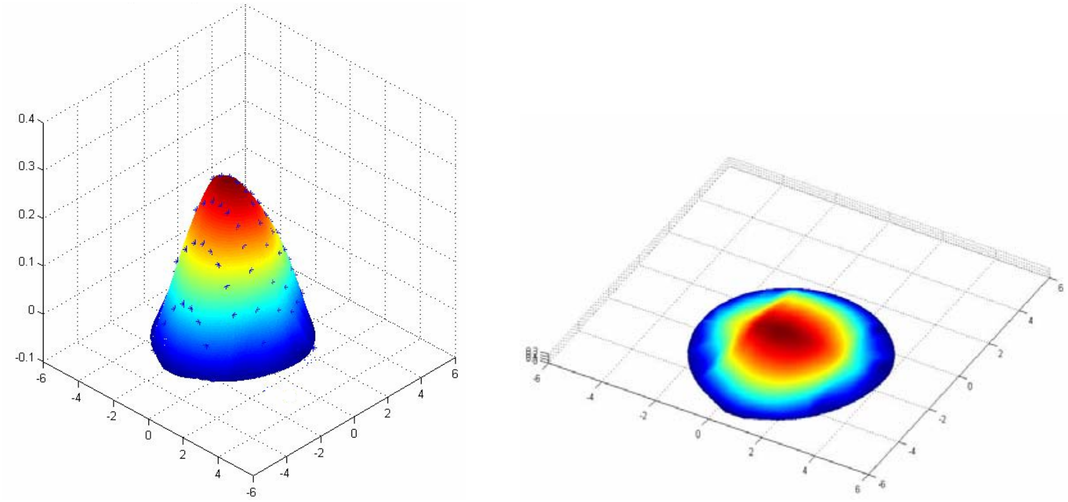

(a) Weld pool surface using EPA algorithm and 2D boundary model

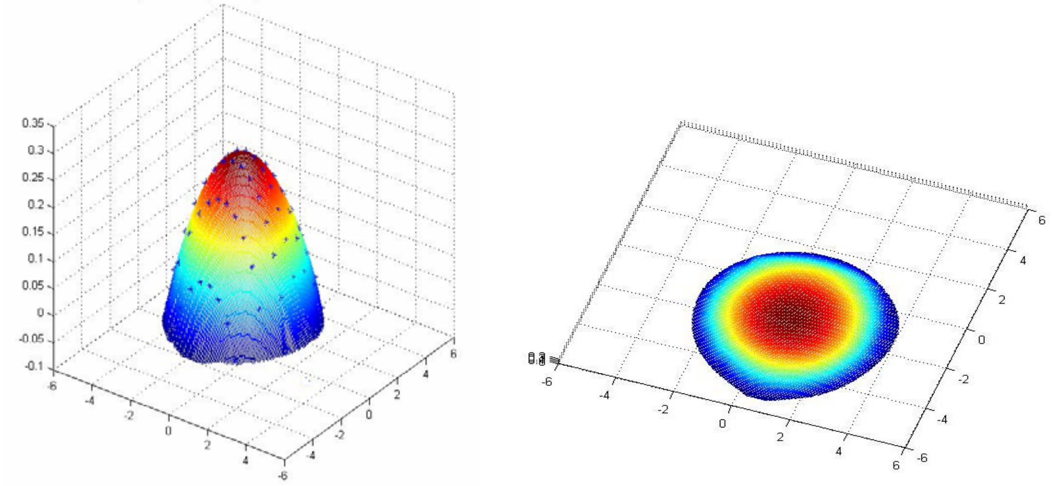

(b) Weld pool surface using OPA algorithm and 2D boundary model

Figure 6-18, Reconstructed whole weld pool surface

In Figure 6-18, the new whole interpolated weld pool surfaces are reconstructed by using both the boundary model and the optimal surfaces computed by EPA and OPA algorithms. As can be seen, the two reconstructed surfaces are similar and they are both convex with near the same height. This is related to the properties of the welded work piece – mild steel. The heights of the surfaces are 0.3067mm and 0.3045mm respectively in Figure 6-18 (a) and (b). The surface using OPA algorithm is smoother than the one using EPA, which meet the practical situation of weld pool surface.

However, in the reconstructed pool surfaces, there is no concave part inside the weld pool surface under the torch, which should appear in practical case because of the arc pressure. The possible explanation is the concave part in the weld pool surface is very small due to the low welding current (75 A) and there is no laser dots projected onto it. As shown in the results, although the optimal results only have small errors, obvious differences of the reflected images still can be seen in Figure 6-12 and Figure 6-15. Since it is a sensing system for small object, there are many factors in each step of the scheme that may bring the errors, such as the measurement, image processing, the surface interpolation and boundary modeling process. The errors in the measurement system are analyzed in Chapter 8.

6.5 Summary

In this chapter, interpolation reconstruction scheme (IRS) is discussed as one of two schemes for reconstructing three-dimensional weld pool surface based on the obtained data. It is found:

- The two algorithms (OPA and EPA) in IRS can effectively use slope field information to compute the reflection points based on the assumptions of different edge points' positions and interpolate the weld pool surface using these points. Some error evaluation parameters related to the difference between captured and computed reflected dots' positions are proposed to find the optimal result. The depth information of the weld pool surface can be acquired by the algorithms.
- In IRS, experiments show OPA algorithm has better performance than EPA algorithms. It has smaller errors and produce smoother weld pool surface. This is because of its more reasonable assumption.

- The proposed 2D boundary model uses the reliable boundary points to fit three different parts of weld pool surface boundary in polar coordinate system. The synthesized boundary successfully describes the 2D shape of the weld pool and provides important complementary information for rebuild the whole weld pool surface. The width and length parameters can also be extracted by the modeling method.

CHAPTER 7

EXTRAPOLATION RECONSTRUCTION SCHEME

Interpolated reconstruction scheme (IRS) provides an effective way to rebuild the weld pool surface, but there are still some places that can be improved. In IRS, the position of the two-dimensional weld pool boundary is assumed to be on Z=0 plane, which is not so reasonable especially for the rear part of the weld pool surface. Thus extrapolated reconstruction scheme (ERS) is proposed to improve the IRS. In this chapter, ERS is discussed and compared with IRS. According to the results in Chapter 6, OPA algorithm in IRS has better performance. Thus it is applied in this chapter as the representative of IRS and ERS is also developed based on it. Here OPA algorithm based IRS is simply called IRS.

7.1 Extrapolation Reconstruction Scheme

At this step, the results from the previous steps are provided by two discrete sets of points ($R = \{r_{k,t}, (k,t) \in I\}$, $P = \{p_{i,j}, (i,j) \in S\}$) and their corresponding match relationships. Now the task is to derive the three-dimensional weld pool surface from these matched discrete point sets based on the governing reflection law. It is apparent that the issue is not to apply the reflection law to calculate the reflection of incident rays. Instead, the issue is to see what three-dimensional surface may generate a set of reflected points which are close enough to the given $R = \{r_{k,t}, (k,t) \in I\}$. The issue is thus an inverse problem of the reflection law and analytical solution appears not exist.

To resolve this issue, an engineering method is needed and we thus propose two schemes, interpolation and extrapolation reconstruction schemes (IRS and ERS), to find an optimally estimated three-dimensional surface. The ERS differs from the IRS mainly in the way for determination of the surface boundary. While the IRS fits a two-dimensional model as the boundary of the weld pool surface, the ERS uses the model based cylinder to intersect with the optimally estimated three-dimensional surface to find boundary. The details of the schemes proposed are presented below and the flowchart of ERS and IRS can be seen in Figure 7-1. In the following discussion, the steps marked with '*' are similar with the steps of interpolation reconstruction scheme and they are not described in detail. In addition, these steps are described using the image processing result in Figure 5-29 as an example.

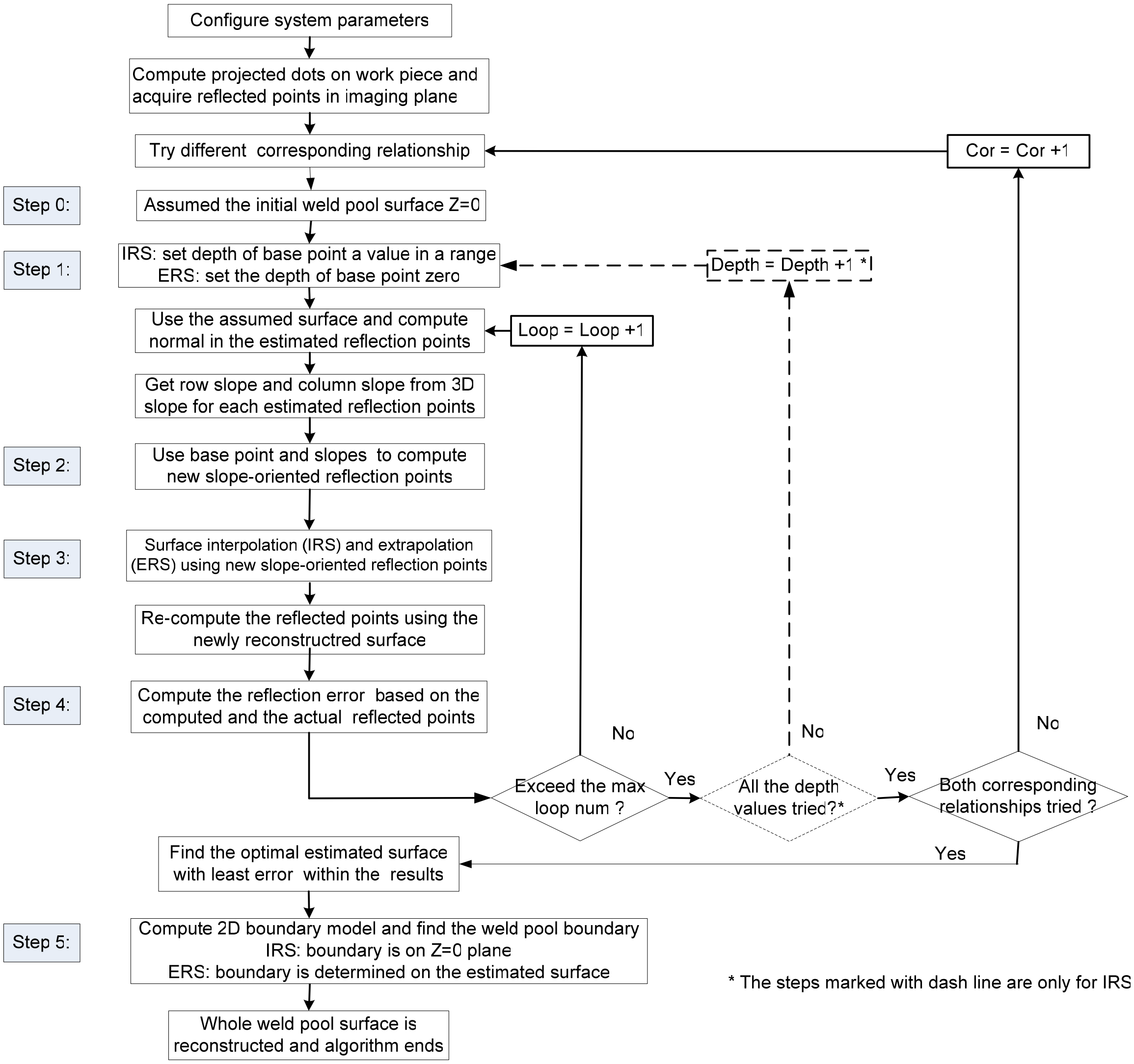

Figure 7-1, Flowchart of interpolation and extrapolation reconstruction schemes

Step 0: A flat plane (Z=0) is used as the initial estimate of the weld pool surface; (*)

Step 1: Use the assumed surface to compute the slope field; (*)

In ERS, the tested corresponding relationships are decided according to the shape of reflected image. If the shape is convex, I/I and S/S relationships are tested; if the shape is concave, S/I and S/S relationships are tested. This change can simplify the scheme and it is based on the results of system simulation discussed in section 4.2.2.

Step 2: Compute the new slope-oriented reflection points based on the slope field;

It is obvious that the estimated surface in the first step can not meet the slope requirements to produce the reflected image, and in the second step the positions of new slope-oriented reflection point set P'' ($P''=\{p''_{i,j},(i,j)\in S\}$) is calculated to approach the actual weld pool surface by using these estimates of slopes.

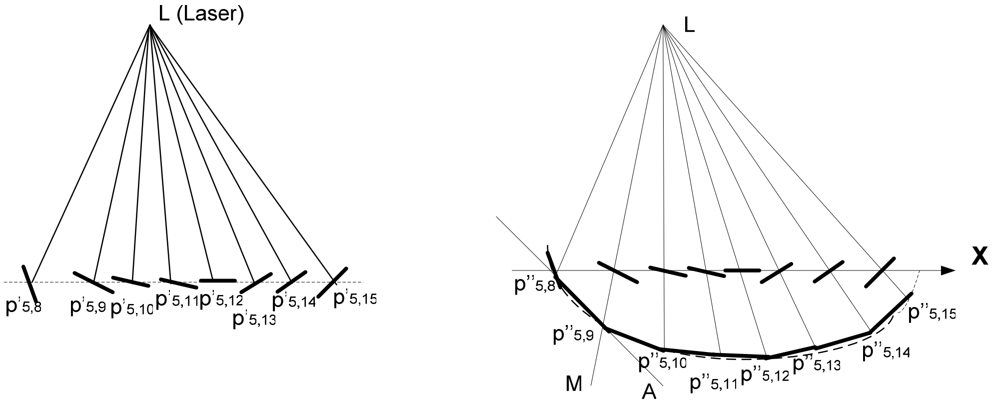

(a) Row slopes on 5th row plane (b) Computation of new reflection points

Figure 7-2, Computation of new slope-oriented reflection points based on base point in IRS

- Assumption of base point

In IRS and ERS, the positions of slope-oriented reflection points are all calculated in relation to a base point among the reflection points, whose position in universal coordinate system is assumed. In IRS, the reflection point corresponding to the left-down reflected dot $r_{1,5}$ in Figure 5-29 (a) is chosen as base point, and dot $p_{5,8}$ ($p'_{5,8}$ or $p''_{5,8}$) is the base point for S/S corresponding relationship. In IRS, the height of the base point is sequentially selected in a range, such as (-0.5 mm, 0.5 mm). While in ERS, the base point is chosen according to different corresponding relationships so as to make it on the left head part of the weld pool surface. For instance, in Figure 5-29 (b) $p_{11,6}$ ($p'_{11,6}$ or $p''_{11,6}$) is the base point for S/S corresponding relationship in ERS. In the meantime, the height of the base point can be reasonably assumed to be zero instead of searching in a range since the base point is on the head boundary of the weld pool surface.

- Computation of new slope-oriented reflection points

After the base point is selected, all the other reflection points on pool surface can be calculated based on it. There are three computation processes in ERS and IRS, which are shown in Figure 7-3.

Firstly the new slope-oriented reflection (projected) dots on the same row as the base point are computed using their row slopes. As shown in Figure 7-2, the new reflection points at 5th row are computed by using their row slopes in IRS. Since the position of base point $p''_{5,8}$ is decided, the adjacent dot $p''_{5,9}$ can be located as the intersection point of projected ray *LM* and line $p''_{5,8}A$, and the slope of line $p''_{5,8}A$ can be calculated as:

$$S_{p''_{5,8}A} = sign\left(S_{p''_{5,8}}\right) \cdot \left| \left(S_{p''_{5,8}} + S_{p''_{5,9}}\right) / 2 \right| \quad \text{.... (Eq.7-1)}$$

where the function sign() means the positive or negative sign of the slope and $S_{p''_{5,8}}$ and $S_{p''_{5,9}}$ refer to the row slopes of the reflection point of $p''_{5,8}$ and $p''_{5,9}$. Follow the same procedures all the other reflection points in 5th row can be calculated as shown in Figure 7-2 (b).

Then based on the middle point of the row with base point, the middle points at the same column but different rows can be calculated by using column slopes. For example, since in ERS the position of middle point $p''_{5,12}$ ($p''_{11,12}$) is known, it can be used as a base point to calculate the other updated middle reflection points at 11th column using column slopes just as done in previous step.

At last, row slopes are used to obtain the positions of all the other new reflection points based on the positions of the middle points. Thus the positions of all updated reflection dots are calculated by using the computed slope field.

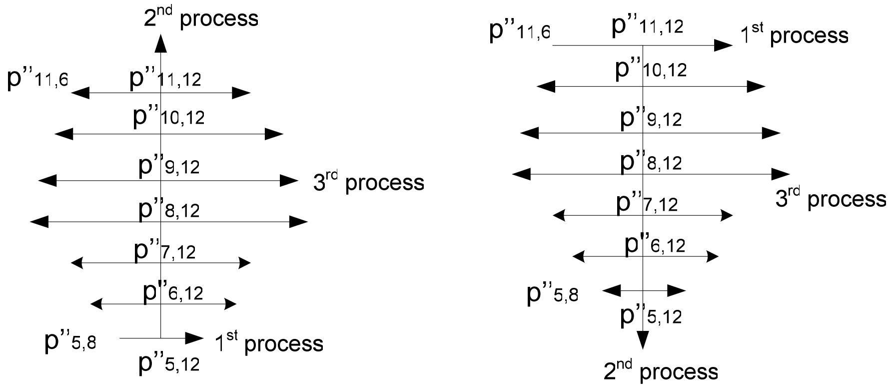

(a) For IRS (b) For ERS

Figure 7-3, Steps of computing new reflection points

Step 3: Reconstruction of weld pool surface using new reflection points;

In the third step, a weld pool surface should be deduced depending on the reflection points P'' computed in the second step. Here a method [64] which can realize both interpolation and extrapolation to form smooth surface is applied in ERS. It can produce a surface from non-uniformly sampled data in the form of

$z = f(x, y)$ …. (Eq.7-2)

In IRS, the area of reconstructed surface is limited by the reflection points while in ERS the area of the reconstructed surface is not, which makes their ways to determine boundary different.

Step 4: Compute the error of the reconstructed surface; (*)

Step 5: Calculate 2D surface model and use it to find the weld pool boundary.

In this step, a two-dimensional piece-wise boundary model $r(\theta)$ of weld pool surface in a polar coordinate system is developed to determine the boundary of the three-dimensional weld pool surface, which has been discussed in Section 6.3.2. In IRS, the computed 2D boundary model in Z=0 plane is assumed to be weld pool surface boundary. However in ERS since the reconstructed weld pool surface is extrapolated, it is possible to find the more reasonable boundary based on the proposed model. The established 2D boundary model on Z=0 plane can be used to determine the X and Y coordinates of the pool surface boundary and the corresponding boundary points can be decided on the optimally estimated surface. At last, the newly found boundary points together with the optimal reflection points are used by interpolation method to get the new whole weld pool surface.

7.2 Reconstruction Results

In this section, the reflected image shown in Figure 7-4 (a) is used to study the two reconstruction schemes (IRS and ERS) and Figure 7-4 (b) shows the extracted reflected dots. The results of the two schemes are compared and discussed.

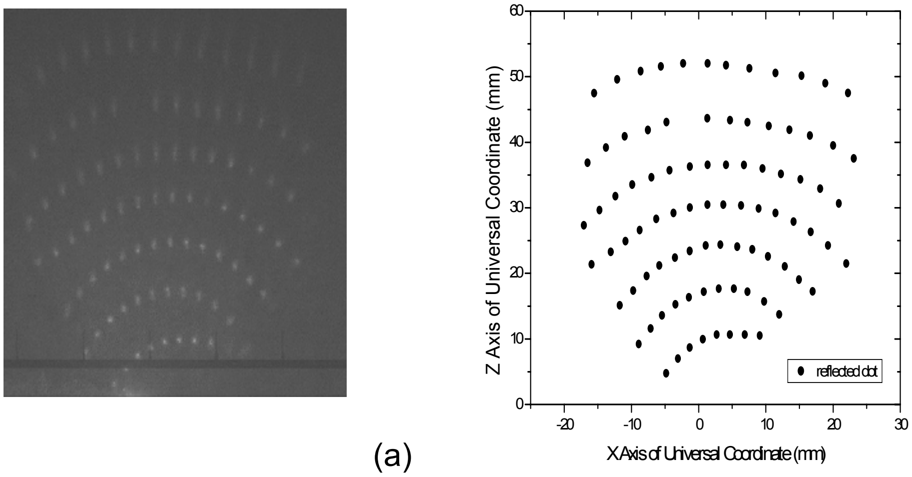

(a) (b)

Figure 7-4, One reflected image (a) and its processing result (b)

By using extrapolation reconstruction scheme (ERS), the computed minimal average reflection error (ARE) is 0.1234 mm, which is a little smaller than the result of IRS 0.1691 mm. In IRS, the smallest ARE is achieved when the height of the base point is 0. The optimal surfaces and the reflection points are shown in Figure 7-5 and their corresponding relationship are all S/S. It can be seen the area of optimally interpolated surface reconstructed by using IRS is limited by the reflection points, but the extrapolated result of ERS is not.

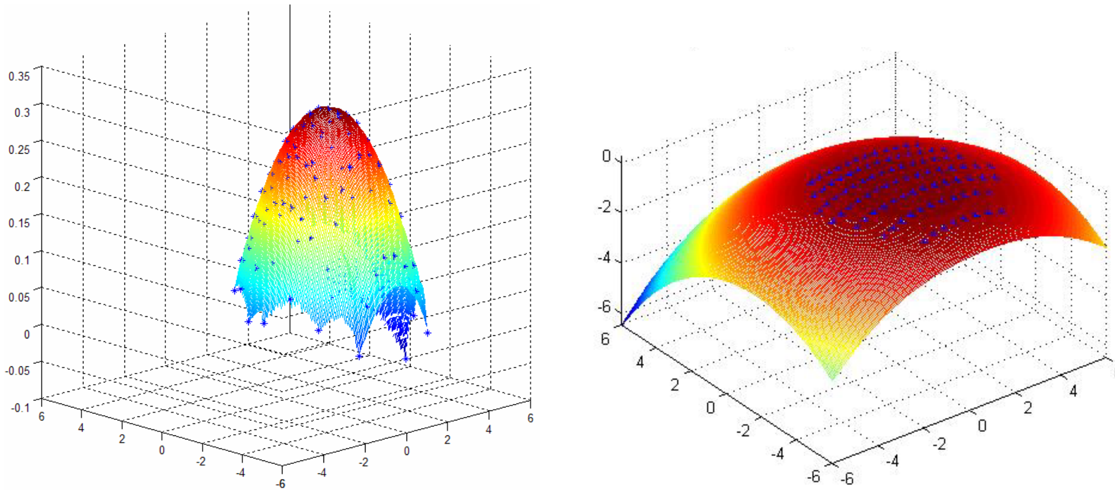

(a) The interpolation result of IRS (b) The extrapolation result of ERS

Figure 7-5, Optimal estimated weld pool surface

In Figure 7-6, the positions of actual reflection points and computed reflected points using optimally estimated surface are shown for the two schemes. These two results are similar, but for the matching extent of edge points the performance of ERS is better since extrapolation works better than interpolation for the slope estimation at edge points. One thing should be noted here. The absent dot $r_{6,7}$ corresponding to center reference point in Figure 5-29 (a) is still considered as a reflected point in the schemes, and its position is assumed in the middle of its adjacent two dots in the same row of Figure 7-6.

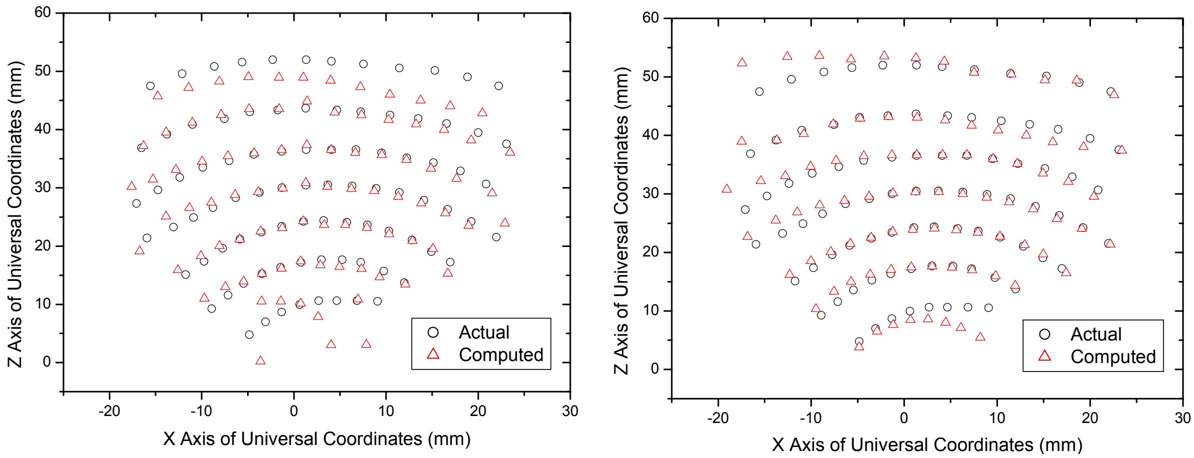

(a) Result of IRS (b) Result of ERS

Figure 7-6, Computed and actual reflected points compare using different schemes

Based on the results of interpolation or extrapolation reconstruction methods and the Sequential/Sequential (S/S) corresponding relationship, the fitted two-dimensional (2D) boundary (at Z=0 plane) is used to find the boundary points. The computed model is shown in Figure 7-7. The point in the center is the origin of the used polar coordinate system in the model and it also defined as the 'center point of the weld pool'. Because the welding speed is slow (3mm per second), the difference between width (6.7313mm) and length (7.1182mm) is small. Since the welding torch electrode is on the Z axis, it is obvious in Figure 7-7 that distance of the universal coordinate origin to the head of weld pool is smaller than the distance to the tail part.

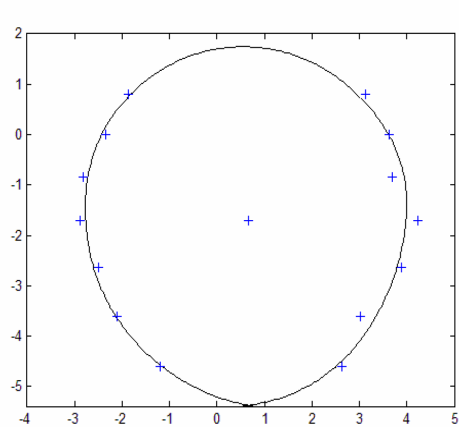

Figure 7-7, Fitted two-dimensional weld pool boundary model (on Z=0 plane)

In Figure 7-8, the new whole weld pool surfaces are reconstructed by using both the boundary model and the optimally estimated surfaces in IRS and ERS. As can be seen, the two reconstructed surface are similar and they are both convex surfaces. This is related to the properties of the welded work piece – mild steel. The heights of the surfaces are 0.3045 mm and 0.2533 mm respectively in Figure 7-8 (a) and (b). The difference is small and it is caused by different methods used to reconstruct the surface in IRS and ERS. As can be seen, difference between their boundaries is obvious due to different ways to compute boundary in IRS and ERS. The result of the extrapolation reconstruction scheme is more reasonable since the boundary is not exactly on Z=0 plane and the rear part of weld pool is lower than the other parts, which meets the practical situation and the result of direct observation. As can be seen, the performance of ERS is better than that of IRS.

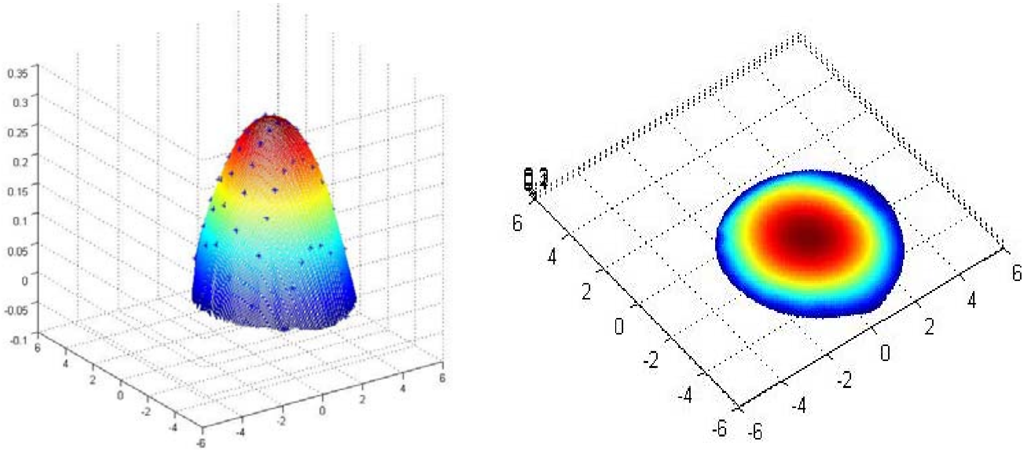

(a) Weld pool surface using interpolation reconstruction scheme (different views)

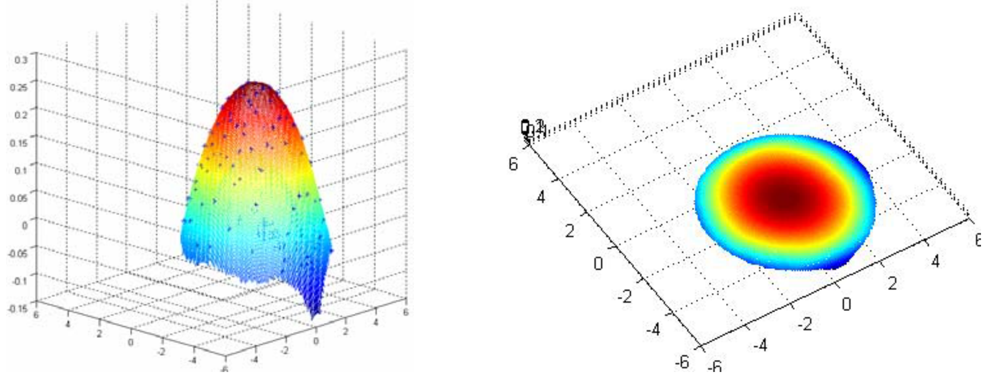

(b) Weld pool surface using extrapolation reconstruction scheme (different views)

Figure 7-8, Results of different reconstruction schemes

7.3 Analysis of Variations in Weld Pool

A series of reflected images are recorded during an experiment using the same nominal constant welding parameters in order to examine if the weld pool surface would maintain exactly unchanged. Figure 7-9 shows 15 reflected images taken in the experiment. During this experiment, a sheet of 2 mm thick mild steel is used as the work piece and the welding current is kept on 75 A with constant welding speed of 3 mm per second. The distance between the torch and imaging plane is 50 mm and the projection angle of laser diode is about 31 degree.

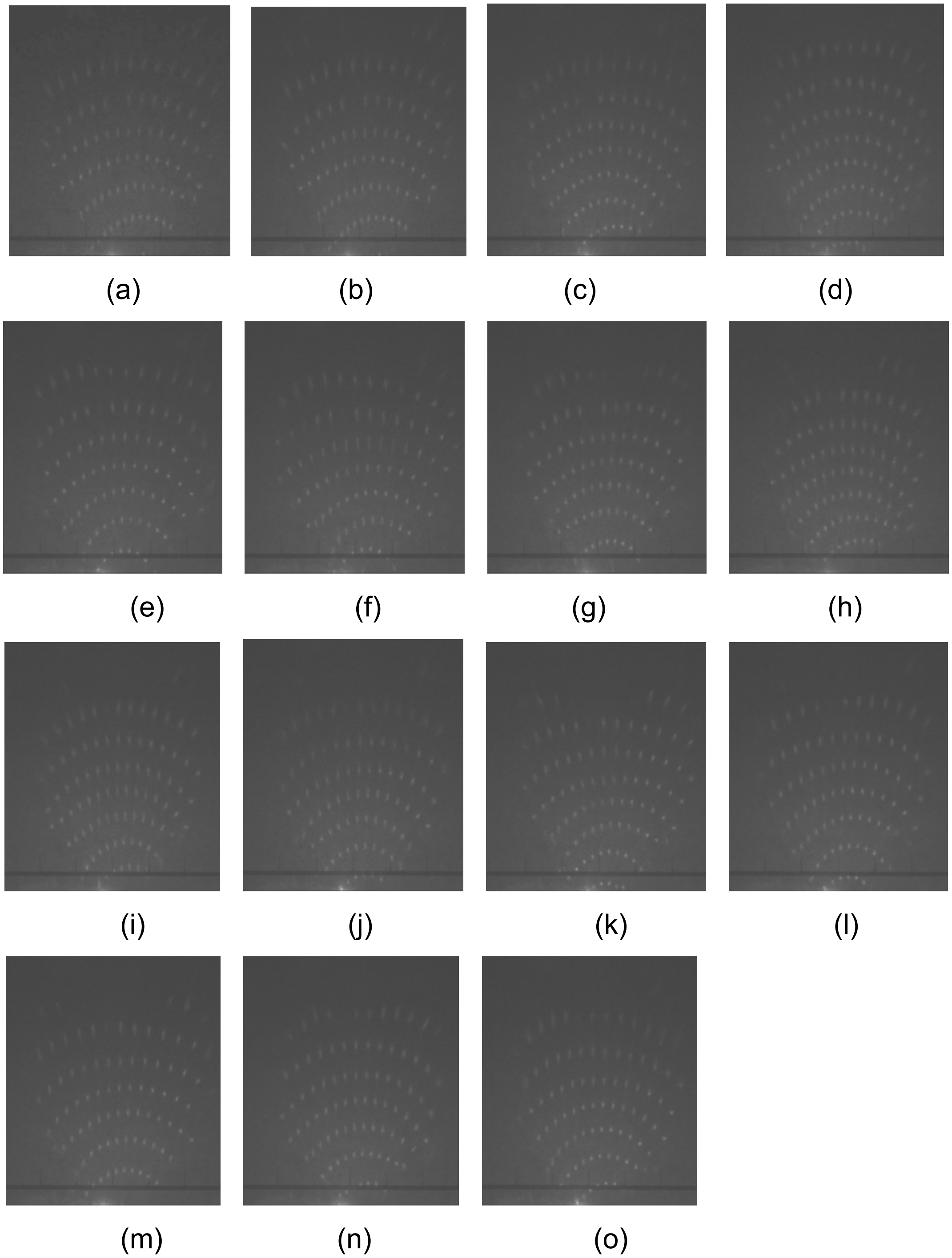

(a) (b) (c) (d)

(e) (f) (g) (h)

(i) (j) (k) (l)

(m) (n) (o)

Figure 7-9, Captured reflected images

From the acquired reflected images, the shape changes of weld pool surface can be seen clearly. The first variation which can be seen from the reflected images is the number of rows of reflected dots, which changes among 6, 7 and 8. This means the length of the weld pool surface is changing. The second change is the corresponding position of the center reference point in the reflected images, which shows the position change of weld pool surface. Even when the number of rows is the same in some images, the number of dots in a row still changes, which reflect the variation of width of weld pool surface. These deductions are based on the facts that projected laser dot matrix covers the whole weld pool surface immovably and only the dots on the pool surface can be reflected onto the imaging plane. The changes of reflected images can directly present the shape variations of weld pool surface in the same welding condition.

In order to further investigate the variation of weld pool quantitatively, the extrapolation reconstruction scheme (ERS) is applied to reconstruct the weld pool surface for each reflected image in Figure 7-9. One thing should be noted here. In our study, some unclear dots located in upper fragmental rows are neglected since some dots in the row are blocked by torch and they are not suitable for the proposed reconstruction schemes, such as the ones in Figure 7-9 (h), (k) and (m).

By using the ERS, the optimal estimates of three-dimensional weld pool surfaces are reconstructed for each reflected image of Figure 7-9 and the computed reflected images by using the optimally estimated surfaces are compared with the actual ones are shown in Figure 7-10.

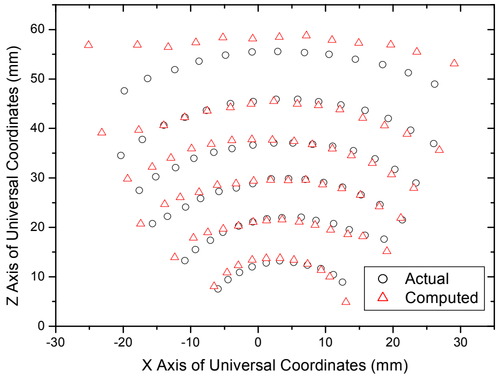
Z Axis of Universal Coordinates (mm)
X Axis of Universal Coordinates (mm)
0
10
20
30
40
50
60
-30
-20
-10
0
10
20
30
Actual
Computed

(a)

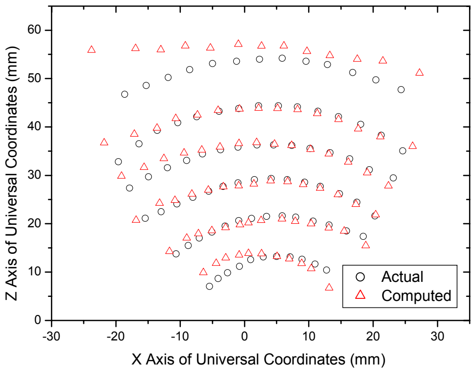
Z Axis of Universal Coordinates (mm)
X Axis of Universal Coordinates (mm)
0
10
20
30
40
50
60
-30
-20
-10
0
10
20
30
Actual
Computed

(b)

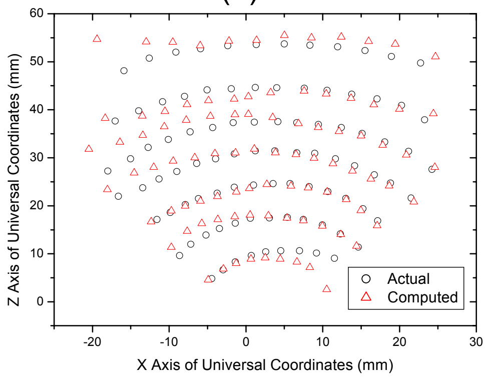
Z Axis of Universal Coordinates (mm)
X Axis of Universal Coordinates (mm)
0
10
20
30
40
50
60
-20
-10
0
10
20
30
Actual
Computed

(c)

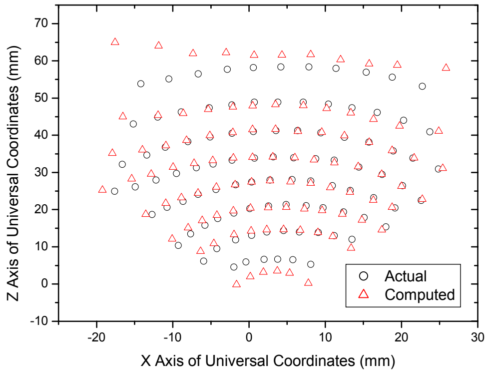
Z Axis of Universal Coordinates (mm)
X Axis of Universal Coordinates (mm)
-10
0
10
20
30
40
50
60
70
-20
-10
0
10
20
30
Actual
Computed

(d)

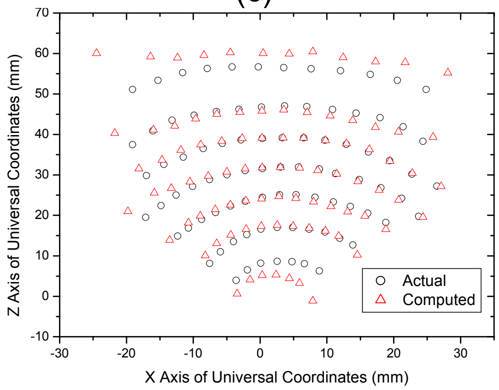
Z Axis of Universal Coordinates (mm)
X Axis of Universal Coordinates (mm)
-10
0
10
20
30
40
50
60
70
-30
-20
-10
0
10
20
30
Actual
Computed

(e)

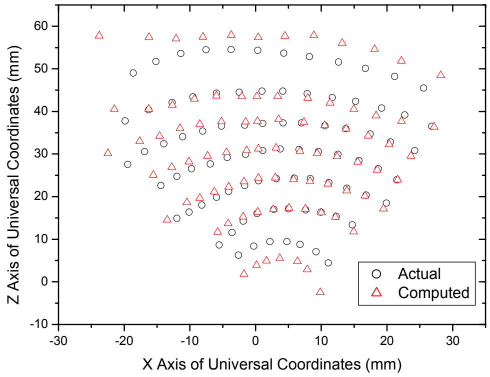
Z Axis of Universal Coordinates (mm)
X Axis of Universal Coordinates (mm)
-10
0
10
20
30
40
50
60
-30
-20
-10
0
10
20
30
Actual
Computed

(f)

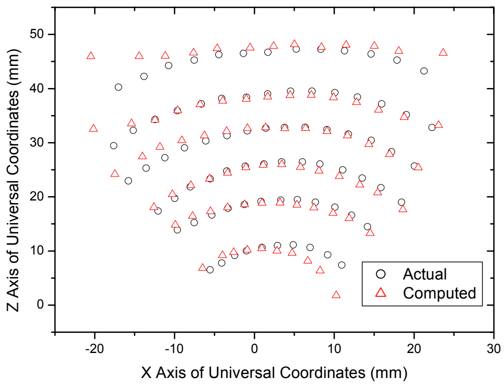
Z Axis of Universal Coordinates (mm)
X Axis of Universal Coordinates (mm)
0
10
20
30
40
50
-20
-10
0
10
20
30
Actual
Computed

(g)

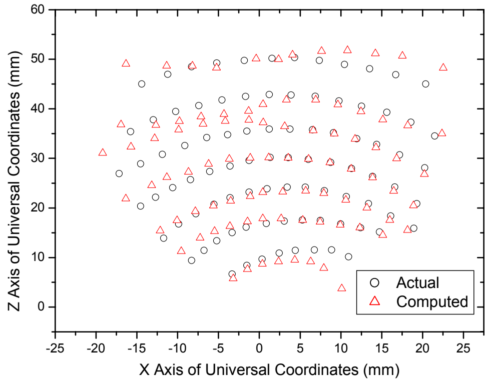
Z Axis of Universal Coordinates (mm)
X Axis of Universal Coordinates (mm)
0
10
20
30
40
50
60
-25
-20
-15
-10
-5
0
5
10
15
20
25
Actual
Computed

(h)

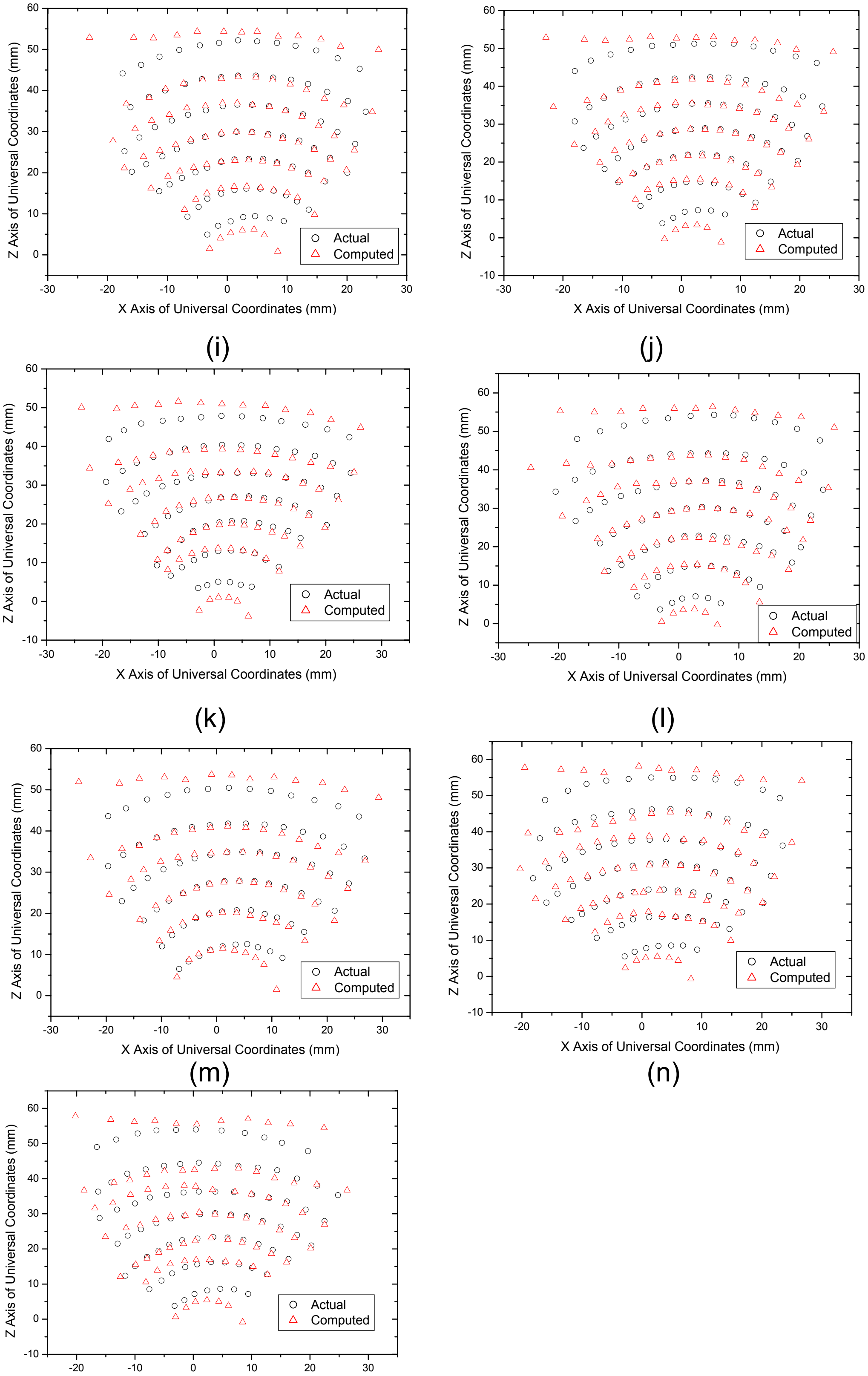

(i) (j)

(k) (l)

(m) (n)

(o)

Figure 7-10, Computed and actual reflected points in comparison

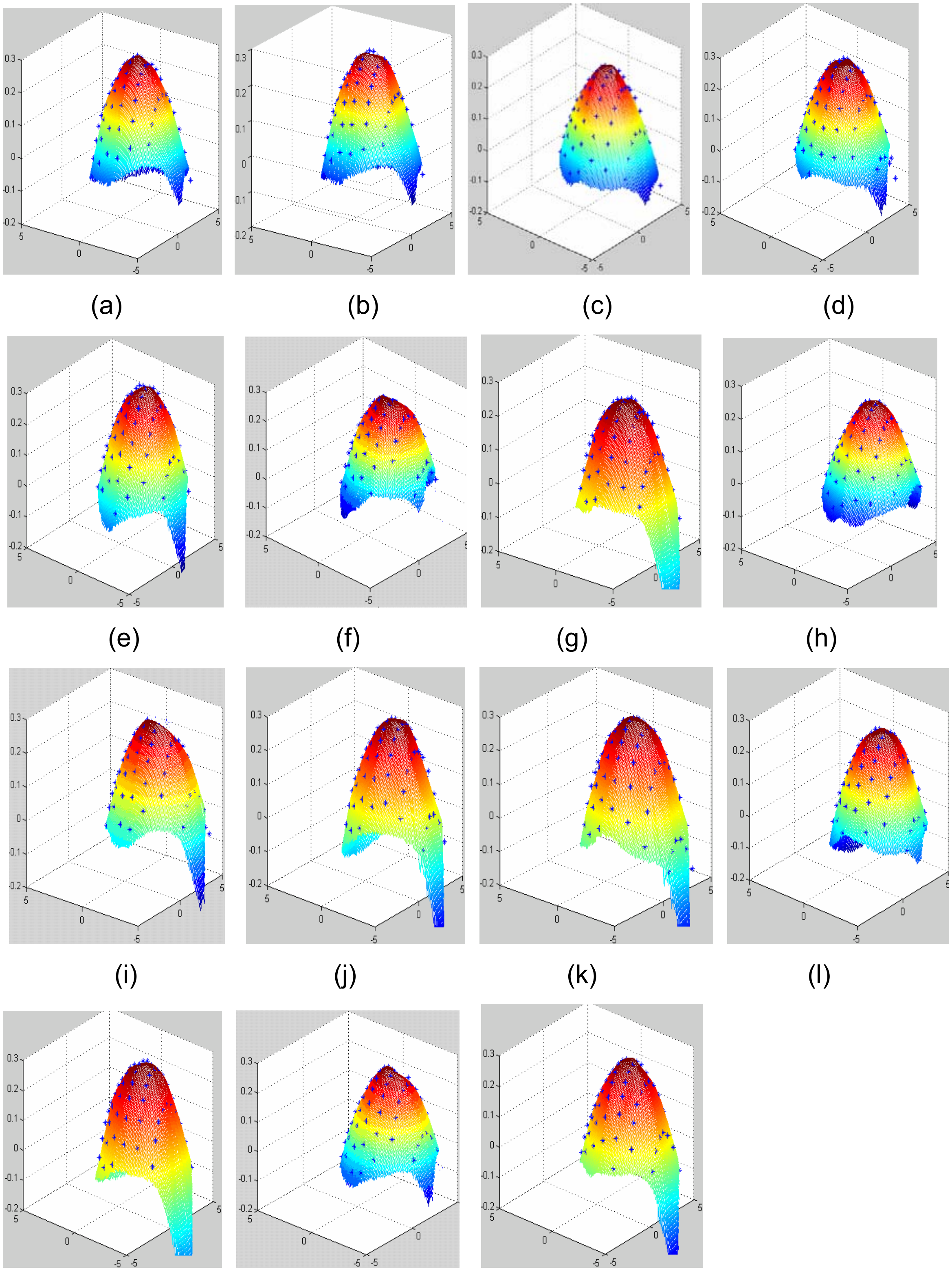

(a) (b) (c) (d)

(e) (f) (g) (h)

(i) (j) (k) (l)

(m) (n) (o)

Figure 7-11, Reconstructed three-dimensional weld pool surface

After the computation of the two-dimensional boundary model, the whole weld pool surface can be reconstructed by using ERS and they are shown in Figure 7-11. The shapes variation of these reconstructed surfaces can be clearly seen, especially for the rear part.

In Figure 7-12 the computed average reflection errors (ARE) for different reflected images vary insignificantly in a range of (0.13632mm, 0.23247mm). Figure 7-13 shows the variation of two-dimensional parameters of the reconstructed weld pool: the width and the length, which are decided by the proposed boundary model. The width of weld pool surface varies in the range of (6.4463mm, 6.9183mm). The average width and its variance are calculated as:

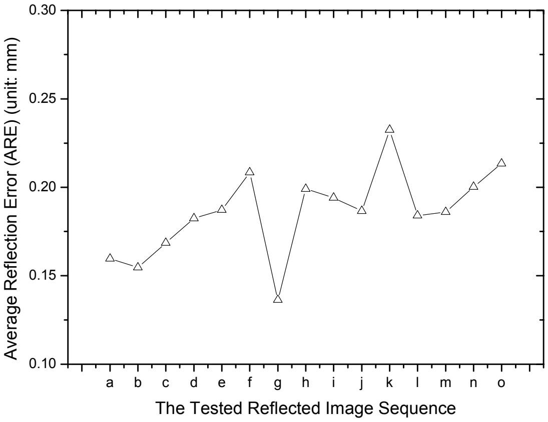

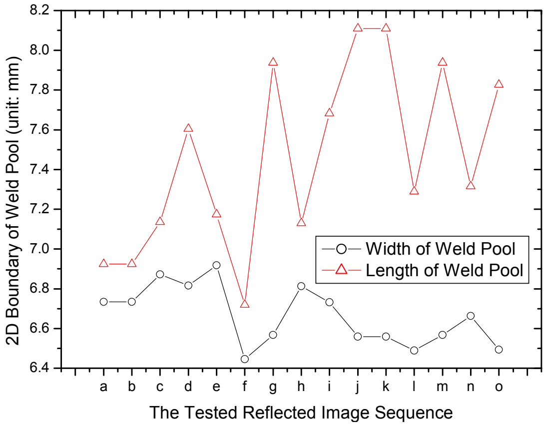

Figure 7-12, Average reflection errors Figure 7-13, Variation of weld pool surface

$$\overline{w} = E(w) = \sum_{i=1}^{15} w_i \Big/ 15 = 6.6645mm ,$$

$$V_w = E\left(\left(w_i - \overline{w}\right)^2\right) = \sum_{i=1}^{15} \left(w_i - \overline{w}\right)^2 \Big/ 15 = (0.15)^2 \, mm^2 \qquad \text{.... (Eq.7-2)}$$

where w_i presents the width of the i^th reconstructed weld pool surface. The length of the pool surface varies in the range of (7.1303mm, 8.1092mm). The average length and its variance are:

$$\bar{l} = E(l) = \sum_{i=1}^{15} l_i \Big/ 15 = 7.4549mm ,$$

$$V_l = E\left(\left(l_i - \bar{l}\right)^2\right) = \sum_{i=1}^{15} \left(l_i - \bar{l}\right)^2 \Big/ 15 = (0.46)^2 \, mm^2 \qquad \text{.... (Eq.7-3)}$$

where l_i presents the length of the ith reconstructed weld pool surface. It can be seen that the variation of weld pool surface length is greater than that of the width. Meanwhile these two-dimensional parameters can be further used to estimate the change of weld pool surface area.

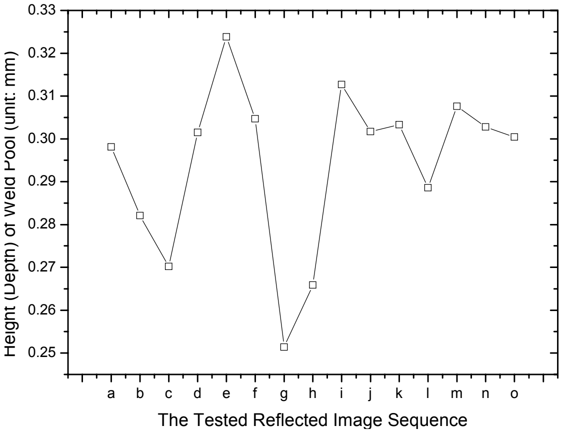

Figure 7-14, Variation of pool height

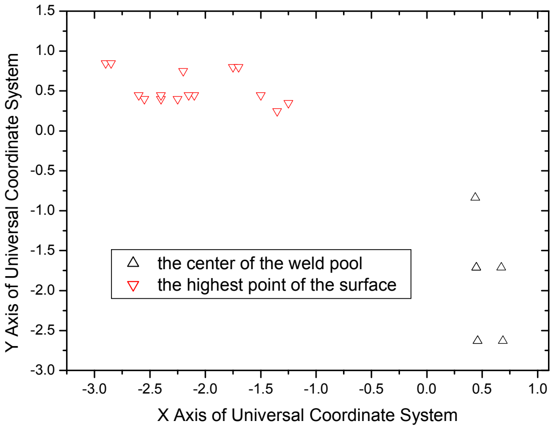

Figure 7-15, Variation of pool position

Figure 7-14 shows the variation of the height of the weld pool surface. Since the reconstructed surfaces are all convex, and the Z coordinate of the highest point in the surface is considered as the height of the weld pool surface. From the figure, it can be seen the heights of the surfaces vary from 0.2514 mm to 0.3238 mm. The average height and variance are:

$$\bar{h} = E(h) = \sum_{i=1}^{15} h_i \Big/ 15 = 0.2943mm \quad ,$$

$$V_h = E\left(\left(h_i - \bar{h}\right)^2\right) = \sum_{i=1}^{15} \left(h_i - \bar{h}\right)^2 \Big/ 15 = (0.019)^2\, mm^2 \qquad \text{…. (Eq.7-4)}$$

where h_i presents the height of the ith reconstructed surface. The variation of the height is very small, which means it changes insignificantly.

In Figure 7-15, the variation of the weld pool positions is shown. It also can be seen that the positions of the center point and the highest point of the weld pool surface are also changing for the studied images. The position of the center point of weld pool is shown in Figure 7-7.

The variations of these three-dimensional parameters discussed above prove that the weld pool surface has small fluctuation even in the same nominal welding conditions and welding parameters. The possible reasons include the small disturbance of welding current and speed, the unstable shielding gas and other interference factors, and small variations in the actual thickness of the plate under the same nominal conditions/values.

7.4 Discussion of Reconstructed Surface

The reconstruction results of the three-dimensional weld pool surface proved the validity of the proposed system and showed the variation of the surface. To better understand the capability of the proposed system and improve the system, the measurement results can be further discussed and elaborated.

Firstly, in the reconstructed pool surfaces shown in Figure 7-8 in section 7.2, there is no obvious concave part inside the weld pool surface under the torch. However, a concave part should always be present because of the arc pressure. A possible explanation for such reconstructed results is that the concave part in the weld pool surface is very small due to the low welding current (75A) and there was no laser dots projected onto it.

Secondly, in section 7.3, some slightly concave segments did exist among upper rows in some of the studied reflected images in Figure 7-9 and the irregular concave parts were embedded in some reconstructed weld pool surfaces shown in Figure 7-11. Figure 7-16 shows some such cases, which include the magnified reflected images and the reconstructed surfaces corresponding to Figure 7-9 (b), (e) and (n). For example, in Figure 7-16 (a) the reflected dots at 4th, 5th and 6th row form non-smooth convex curves and some slightly concave segments exist, which make the reconstructed surface has an obvious concave part inside it. Since the positions of the projected laser rays are unchanged, the variation of the weld pool surface makes more rays projected onto the small concave part of the surface when capturing this image.

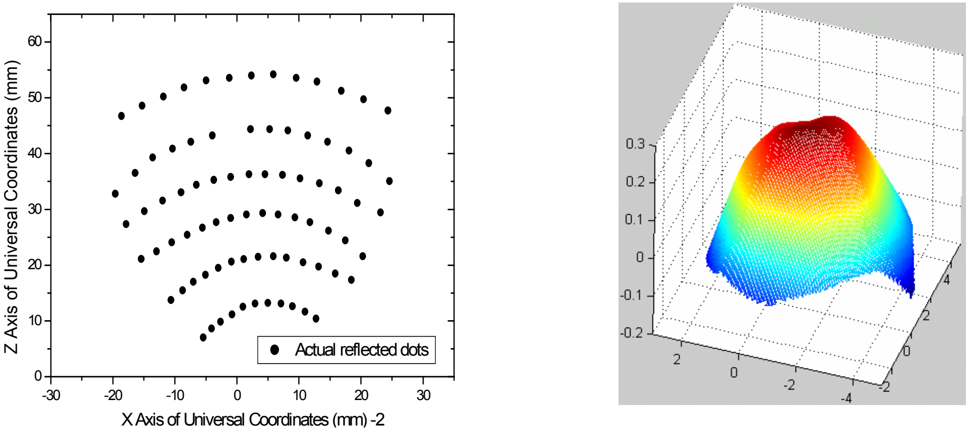

(a) Reflected image and reconstructed surface of Figure 13 (b)

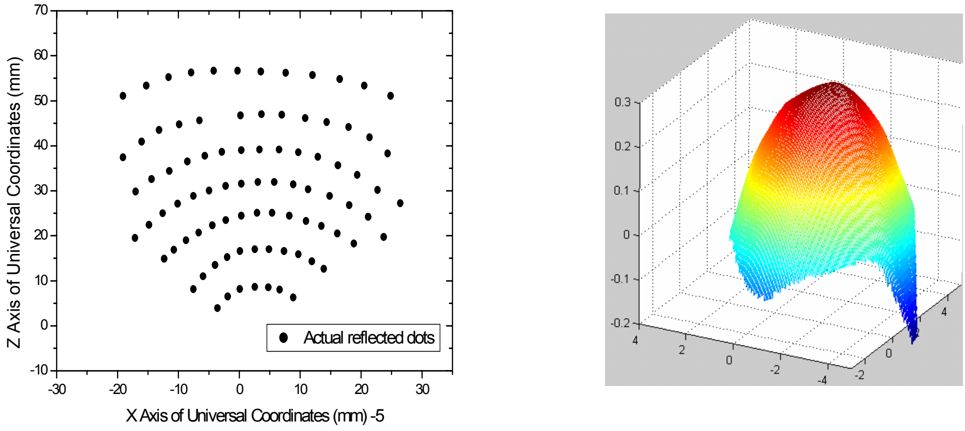

(b) Reflected image and reconstructed surface of Figure 13 (e)

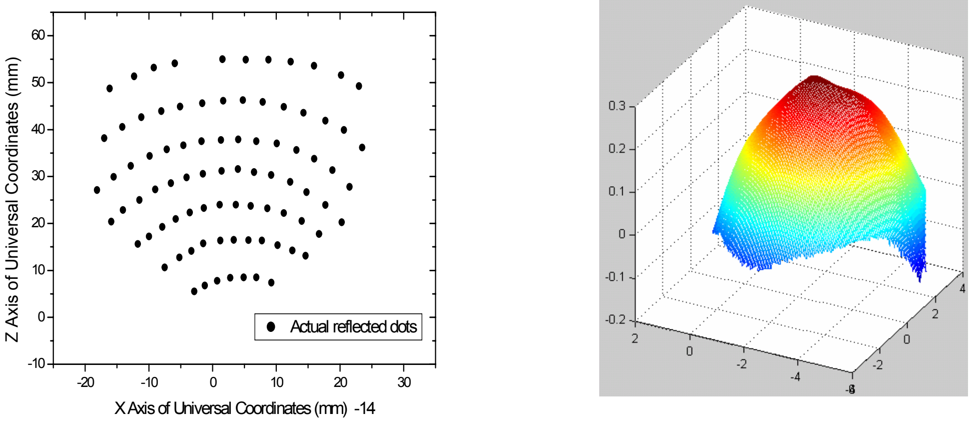

(c) Reflected image and reconstructed surface of Figure 13 (n)

Figure 7-16, Examples of reconstructed weld pool surfaces embedded with concave parts

It can be seen although the errors of optimal results are small, obvious differences of the computed and captured reflected images still can be seen in

Figure 7-6 and Figure 7-10. Since it is a sensing system for small object, there are many factors in each step of the scheme that may bring the errors, such as the parameter measurement, image processing, the surface interpolation/extrapolation and boundary modeling process. Thus the error analysis of the proposed system is needed and some possible ways should be found in order to improve the accuracy of the reconstructed three-dimensional weld pool surface, such as increasing the density of the projected laser rays so as to extract more detail information of the weld pool surface.

7.5 Summary

To derive the three-dimensional weld pool surface based on the image processing results, extrapolation reconstruction scheme (ERS) is proposed in this chapter to improve the interpolation reconstruction scheme (IRS). It is found:

- In comparison with the result of the interpolation reconstruction scheme (IRS), the boundary of weld pool surface reconstructed by using the extrapolation reconstruction scheme (ERS) can achieve better accuracy especially for the rear part of the weld pool.
- Through applying ERS to a series of acquired reflected images in an experiment with nominal constant welding parameters and conditions, the variations of the three-dimensional parameters of the weld pool surface are studied. It is found that the variation of the length is greater than that of the weld pool width, and the variation of the height (depth) of the weld pool surface is much smaller compared to variations of length and width.
- In ERS, the base point is chosen on the head of weld pool surface and its height is reasonably assumed zero. The iterative search process used in IRS is avoided and the reconstruction speed is improved.
- In some reconstructed surfaces, the concave part under the torch, which is formed by arc pressure, can be clearly seen. The capability to detect such detail further verified the effectiveness of the proposed measurement system.

CHAPTER 8

ERROR ANALYSIS OF SYSTEM

Accurate measurement of three-dimensional (3D) weld pool surface not only helps better understand/control the complex welding process but also provides reliable data to verify weld pool numerical models.

To understand the proposed machine vision measurement system and study ways to improve the measurement accuracy, the errors of the reconstructed 3D weld pool surface are analyzed in this chapter. Firstly the error sources of the sensing system are investigated, and then the overall measurement error and other separated errors are discussed and evaluated respectively, such as non-optimal configuration error, system limitation error and reconstruction methodology error. It is found that the major error is from a kind of usage error caused by the non-optimal configuration parameters. The experimental results further show the small measurement error is acceptable and the system limitation error and reconstruction methodology error are insignificant, which verify the accuracy of the proposed three-dimensional GTA weld pool surface measurement system.

8.1 Error Classification

In the proposed measurement system, many factors would cause errors for the reconstructed three-dimensional weld pool surface. Figure 8-1 shows the classification of the possible errors in the measurement system and among the listed errors measurable ones are marked with shadow. Here measurement error refers to the overall error of the reconstructed weld pool surface introduced by the proposed system. There are mainly three kinds of error sources in the system, which contribute to the measurement error. They are system limitation error, usage error and processing error.

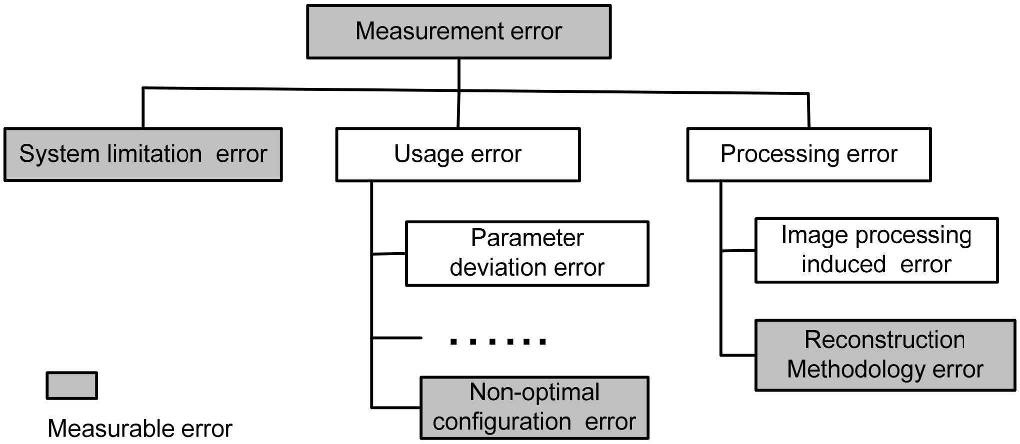

Figure 8-1, Error classification in the proposed measurement system

System limitation error refers to the error due to the fundamental limitation of the system and components used. It is the minimal error achievable with the system used. In the proposed system, although clearer reflected image can be achieved by using multiple-line pattern of structured light, dot-matrix pattern is selected for easy matching reflected and projected rays and effective reconstructing pool surface in our study. In the measurement system, reflection (projected) dots on weld pool surface are firstly computed in order to rebuild the whole surface. Theoretically, the more dots are projected onto the weld pool surface, the more information of the pool surface shape can be obtained from reflected image. However, in the system implementation a commercially available diffractive lens with 19-by-19 dot-matrix pattern is selected for the experiments rather than an infinite-by-infinite dot-matrix pattern. Hence, limited reflection dots' positions on the weld pool surface can be calculated and surface area not covered by the illumination dots can only be predicted by interpolation (or extrapolation) method in the proposed reconstruction schemes. It is then impossible that the reconstructed surface can be measured precisely. As can be see, the system limitation error is caused by the limited resolution of the camera and laser dot matrix etc. in the practical system used. This type of error may be reduced by using better system components.

Usage error in the system is induced during the experiment of acquiring reflected images. In this stage, it is inevitable that there are some deviations between the measured nominal values and the actual values of the system parameters. The corresponding error is defined as ‘parameter deviation error’. This is a kind of man-made random error belonging to usage error. Possible ways to reduce this type of error include improving the accuracy of the calibration method for the system parameters and averaging the values from multiple measurements. Another major usage error is non-optimal configuration error which is caused by non-optimal selection of system parameters. For instance, if the position or projection of the laser diode is not proper, only few points can be reflected onto the imaging plane, which would ultimately cause the reconstructed surface inaccurate. In addition, other factors may also cause related usage error, such as the little shift or tilt of component displacements.

Another class of error is the processing error, which includes image processing induced error and surface reconstruction methodology caused error. In the procedure of image processing, the reflected images are processed and the reflected dots are extracted from the background based on the intensity difference. As can be seen in Figure 3-17, the shape and size of reflected dots vary because of their different projected positions/angles (focusing extent) and the divergence of laser light. Thus it is possible that the extracted position of reflected dots may not be exactly precise. Furthermore since the shape of the reflected dot-matrix pattern is distorted and the dots are densely distributed, the row/column positions of reflected dots sometimes would be difficult to be decided. Hence, mismatches between projected and reflected dot will also cause the measurement error. These errors are defined as “image processing induced error”. During surface reconstruction process, the reflection point on the pool surface can not be precisely decided according to the reflection law if only incident ray and its one reflected dot are known. Thus in the reconstruction schemes an iteration process is proposed to find the optimal estimation for the weld pool surface. Firstly the reflection dots are computed based on assumed surface and slope field, and then the interpolation (or extrapolation) method is used to reconstruct the surface according to the calculated reflection dots. It can be seen the proposed schemes can only find estimated weld pool surface and the error of estimated surface caused by the reconstruction schemes is called "reconstruction methodology error".

As can be seen, there are many error sources existing in the measurement system. They all contribute to the overall measurement error of the reconstructed three-dimensional weld pool surface. Among them, some errors are random and unpredictable, such as the parameter deviation error and the imaging processing induced error; while some are measurable and can be analyzed quantitatively through experiments or simulations. In the following, measurement error, non-optimal configuration error, system limitation error and reconstruction methodology error are discussed respectively.

8.2 Measurement Error

Measurement error refers to the overall error caused by the measurement system. In the welding process, it is impossible to obtain the precise size of three-dimensional molten weld pool surface to evaluate the measurement error. Thus an object with known dimensions should be used to replace the weld pool in the measurement error experiment. Here thumb tack is selected because its size and shape are similar to the weld pool and its surface can reflect the laser light well. By comparing the reconstruction result and the measured object (thumb tack), the measurement error introduced by the whole system can be calculated. Both interpolation and extrapolation reconstruction schemes (IRS and ERS) are tested here.

8.2.1 Experiment design

In Figure 8-2 (a), a thumb tack is pushed into a paper surface under the torch to simulate the molten weld pool, and the 19-by-19 dot-matrix pattern is projected onto its surface. In the experiment, the projection angle of the laser diode is 30.56 degree and the distance between laser diode and origin of coordinate system is 46.4 mm. The distance between imaging plane and the torch is 40.69 mm, and the inter-beam angle of laser diode is 0.77 degree. Figure 8-2 (b) and (c) show the captured image and the result of image processing.

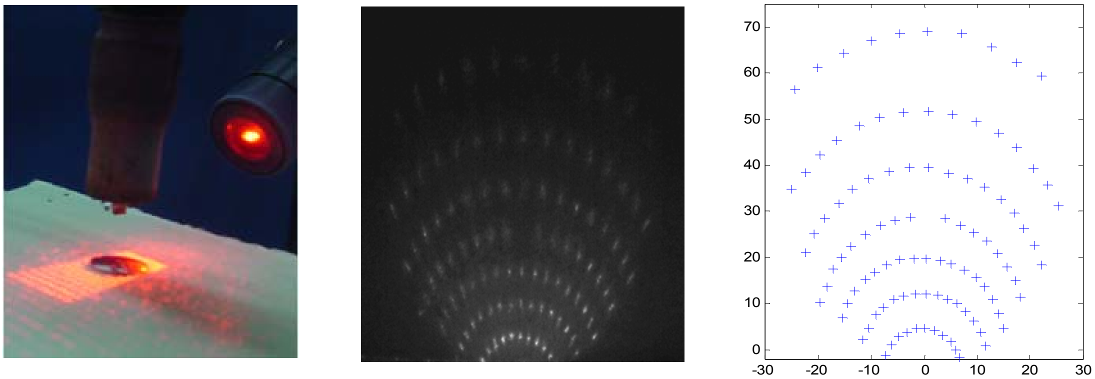

(a) Experiment design (b) Captured image (c) Extracted reflected dots

Figure 8-2, Experiment of measurement error analysis

In the experiment, the two-dimensional piecewise boundary model in the reconstruction schemes is changed to a circle boundary model here since the boundary shape of the thumb tack is known in advance. The basic idea is to extract the boundary (end) points at each reflection row on work piece, and use them to fit a circle, whose center is decided at the middle position of the longest reflection row (end points pair).

By using the interpolation reconstruction scheme (IRS) and the extrapolation reconstruction scheme (ERS), the surfaces are rebuilt as shown in Figure 8-3. As can be seen, the shape of reconstructed surfaces fit the thumb tack well. By using ERS, the computed average reflection error (ARE), which is defined in Eq.6-3, is 0.188150 mm, which is smaller than the result of IRS 0.220807mm.

The comparison between actual and calculated reflected image using the optimally estimated surfaces in IRS and ERS are shown in Figure 8-4. In both figures, the difference between the computed and actual reflection points is small in the middle part, but larger for the edge points. It can be seen the performance of ERS is better than that of IRS. It should be noticed that the absent center reference point in the captured image is also shown in the figures since it is also assumed as a reflected point in the reconstruction schemes. Its position is set at the center of its adjacent dots at the same row.

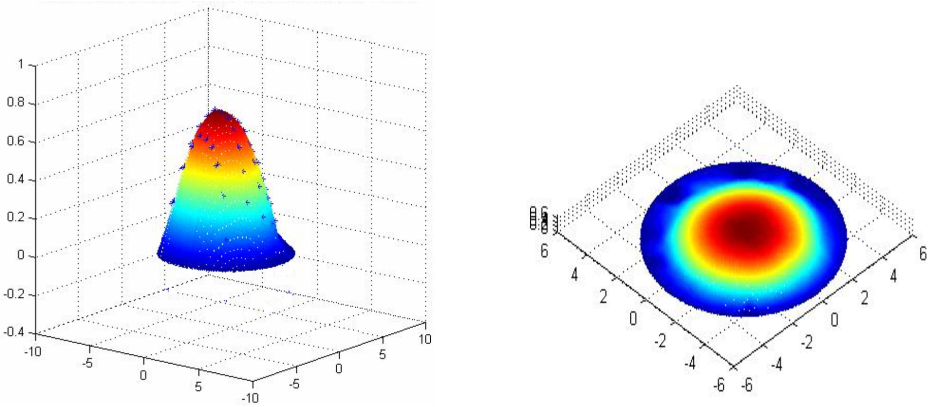

(a) Result of IRS (close view and view with equal axes)

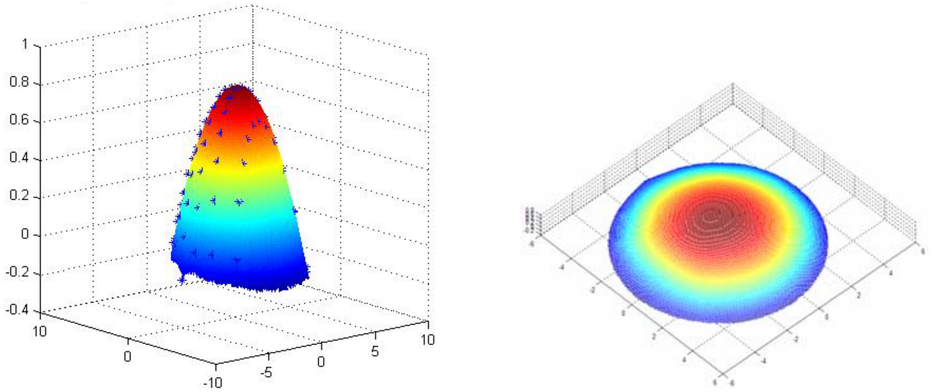

(b) Result of ERS (close view and view with equal axes)

Figure 8-3, Reconstructed surfaces of thumb tack using different reconstruction schemes

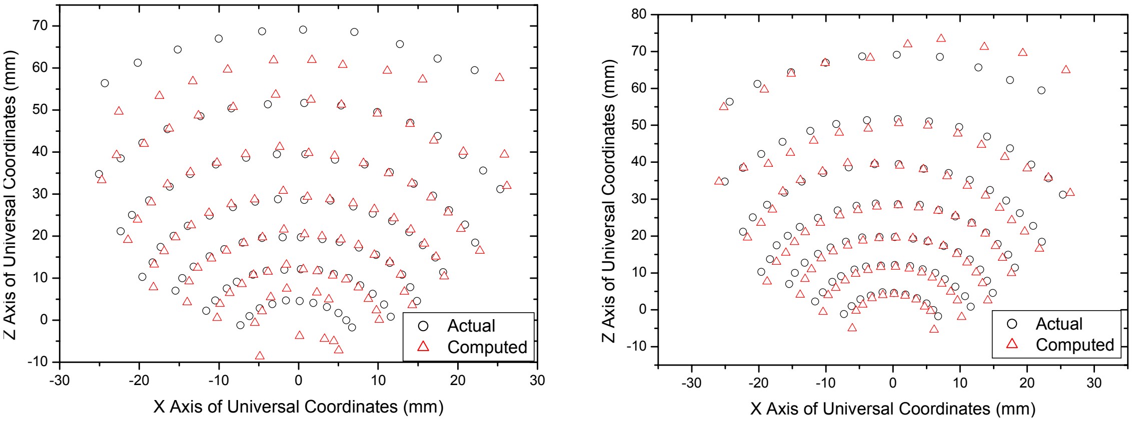

(a) Result by using IRS

(b) Result by using ERS

Figure 8-4, Computed and actual reflection points compare using different schemes

8.2.2 Error computation

Through measurement, the actual three-dimensional parameters of the thumb tack are obtained, which can be used to evaluate the measurement error of the system. The diameter of the thumb tack is 9.75 mm and its height above the paper surface is 0.91 mm. In the experiments, the measurement error (ME) is defined as a percentage error:

$$ME = \frac{|L_c - L_a|}{L_a} \cdot 100\% \qquad \text{.... (Eq.8-1)}$$

where L_c presents the calculated value (of diameter or height) and L_a presents the actual value (of diameter or height). For the reconstruction results of IRS and ERS, the diameters of the pool boundaries are both 9.8953 mm with 1.4903% measurement error. For IRS, the calculated height is 0.7483 mm with 17.77% measurement error. For ERS, the calculated height of the surface (above Z=0 plane) is 0.8270 mm with 9.12% measurement error. It is obvious that this result is better than that of IRS.

As can be seen from the experiment, three types of errors shown in Figure 8-1 are all counted within the measurement error. Since it is a sensing system for small object, the acceptable low values of measurement errors verified the accuracy of the proposed three-dimensional weld pool surface measurement system.

8.3 Analysis of Separated Errors

In the proposed measurement system, reflected image acquisition, processing and surface reconstruction are three sequential procedures and the errors induced in these processes are joined together to impact the precision of the reconstructed weld pool surface. In order to study the errors quantitatively, those error sources should be separated. In this section, to eliminate the impact of the error introduced by system displacement, parameter deviation and image processing, the known convex or concave surfaces are used. Thus some other measurable errors, such as non-optimal configuration error, system limitation error and reconstruction methodology error, can be evaluated by using extrapolation reconstruction scheme (ERS).

In the error numerical simulations, firstly known (convex or concave) surfaces are chosen as the tested weld pool surfaces placed in the universal coordinate system, and the dot-matrix laser pattern is assumed to be projected onto the surfaces to form the reflected images on the imaging plane. Then the obtained reflected images are regarded as the captured images in the practical experiment, which can be further used as the input of the proposed reconstruction schemes to do the error analysis. As can be seen, here precise system position parameters, the position and row/column relationship of the reflected dots can also be used as the input of the reconstruction scheme since they are known in advance.

Figure 8-5 shows the simulated concave and convex surfaces in universal coordinate system. The surface can be as simple as a part of sphere. In the figure, B refers to the diameter of the weld pool surface boundary (circle) and D is its depth. In the tested surfaces, the diameter B changes from 5 mm to 8 mm and the depth D is equal to B/20 or B/10, which are chosen according to the practical dimensions of gas tungsten arc weld pool surface. In the simulations, the shape of the reflected images may vary. However, the correct corresponding relationship is assured since it is known in advance and the correspondence error is not considered.

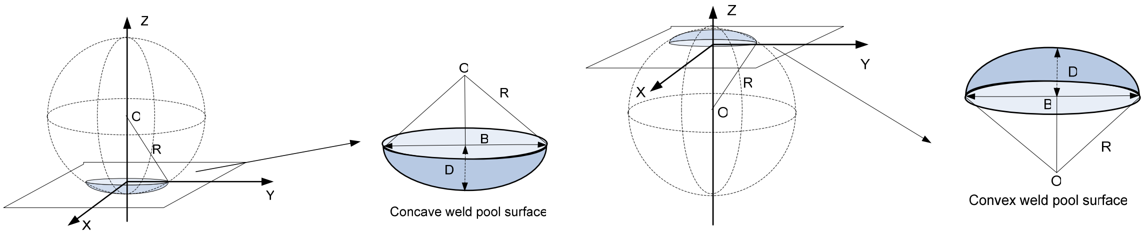

(a) Concave simulation surface (b) Convex simulation surface

Figure 8-5, Two kinds of tested surfaces for calculating errors

8.3.1 Non-optimal configuration error

As discussed in section 8.1, non-optimal configuration error (CE) is caused by the non-optimal displacement of components in the proposed system especially laser diode. In non-optimal configuration error simulation, only one case is studied as a representative to evaluate non-optimal configuration error and the parameters used are those in the experiment which produced the reflected image in Figure 3-17. In that experiment, the projection angle of the laser diode is 31.14 degree and the distance between laser diode and origin is 31.48 mm. The distance between imaging plane and the torch is set to 50 mm.

- Dimensional parameter error

In order to describe the differences between the reconstructed and actual three-dimensional weld pool surfaces, two dimensional error measurement parameters are introduced: non-optimal configuration error of depth (CE-D) and non-optimal configuration error of boundary (CE-B). They are defined as Eq.8-2 and Eq.8-3, which are similar to the definition of measurement error.

$$CE-D=\frac{|D_c-D_a|}{D_a}\cdot 100\%$$

……. (Eq.8-2)

where D_c is the computed depth of the reconstructed surface and D_a is the actual depth of the simulated surface.

$$CE-B=\frac{|B_c-B_a|}{B_a}\cdot 100\%$$

……. (Eq.8-3)

where B_c is the computed diameter of surface boundary and B_a is the actual diameter of the simulated surface.

Figure 8-6 shows the non-optimal configuration errors for different convex and concave surfaces by using extrapolation reconstruction scheme (ERS). In the simulation, the boundary model is also changed to a circle model. As can be seen, the non-optimal configuration errors of boundary (CE-B) are very small for both convex and concave surfaces, and they are in a range from 0.0265% to 2.51%, which shows the boundary model is suitable for the tested surfaces. But the non-optimal configuration error of depth (CE-D) are relative large. For the tested convex surfaces, it varies from 0.78% to 10.85%. For the tested concave surfaces, it varies from 0.1% to 26.9%. The average CE-D is 8.0025%

accordingly. It can be concluded that the error performance even under the same system configuration may vary greatly according to different weld pool surfaces.

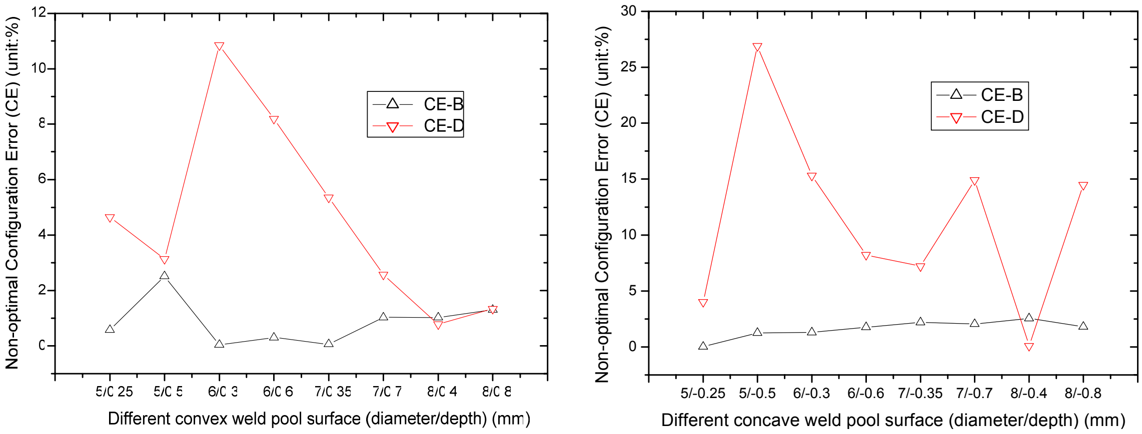

(a) Result by using convex surfaces (b) Result by using concave surfaces

Figure 8-6, Non-optimal configuration errors measured by using different surfaces

- Reflection points error

Despite of the diameter and height/depth of surface, the error caused by non-optimal configuration can be further investigated by evaluating the differences between computed and actual reflection point positions. In the reconstruction scheme, the estimated difference is computed as average reflection error (ARE), which is defined in Eq.6-3. Moreover, since the tested surface is known, the actual ARE can also be achieved by using Eq.8-4.

$$actualARE = \sum_{i,j} D_{i,j} \Big/ n ,....(i, j) \in S \qquad .... \text{(Eq.8-4)}$$

where S refers to the weld pool surface and n present the number of the reflection points on pool surface. $D_{i,j}$ presents the distance between the computed reflection point $p'_{i,j}$ on the estimated pool surface and the actual reflection point $p_{i,j}$ on the tested surface.

Figure 8-7 shows the computed average reflection error (ARE) by using ERS and the actual ARE. As can be seen, the difference between computed and actual ARE are small. It proved the validity of this proposed error measurement parameter. Most of the computed ARE is larger than the actual ARE, which is ranging from 0.0021 mm to 0.2543 mm. The small value of difference verified the accuracy of the proposed reconstruction schemes.

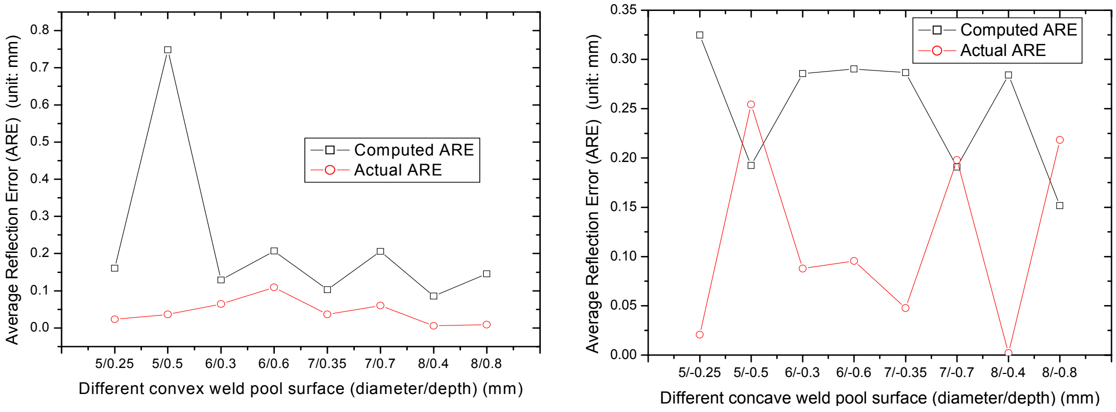

(a) Result by using convex surfaces

(b) Result by using concave surfaces

Figure 8-7, Computed ARE and actual ARE by using different surfaces

From Figure 8-6 and Figure 8-7, it can be seen the differences of the errors are caused by different tested situations, such as the curvature/dimension of tested surfaces. For the large variation of the CE-D, the possible explanation is in some cases laser dots are not projected onto the highest/lowest position of the convex/concave surfaces because of the limited density of the projected dot matrix (19-by-19). Then the height/depth of surface can not be reconstructed correctly by the reconstruction scheme. This phenomenon shows the optimal system configuration is only related to a specific weld pool surface, not all the situations.

It should be noted that the intent here is to investigate the non-optimal configuration error. However, it is impossible that this error can be decoupled from the system components used without using a surface reconstruction method although one may assume a perfect image processing result. Hence, the non-optimal configuration error computed in Figure 8-6 and Figure 8-7 includes the system limitation error and reconstruction methodology error. Fortunately, as will be seen from the discussion in Section 8.3.2 and 8.3.3, these errors are very small. Hence, the above computation does give us reasonable estimation of the non-optimal configuration error.

8.3.2 System limitation error

As mentioned above, two possible reasons for large non-optimal configuration error are non-optimal system configuration parameters and limited scale of dot-matrix pattern. In order to minimize the impact of system configuration parameters and investigate the system limitation error caused by the 19-by-19 dot-matrix pattern, simulations with various system parameters are conducted.

In system limitation error simulation, the 19-by-19 dot matrix pattern is used and the laser position and projection angle are varied in a range. In one of the experiments, the selected system parameters (laser projection angle 31.14 degree and projection distance 31.48 mm) are reasonable since the dot-matrix can not only cover the whole simulated weld pool surface but also make the distances among the projected dots reasonably small (about 0.3~0.5 mm). Hence, different combinations of the system configuration parameters in simulations are selected based on it. The projection angle of the laser diode varies from 25 degree to 35 degree, and the distance between the laser diode and the origin of universal coordinate system changes from 25 mm to 35 mm. Thus the system limitation error can be estimated as the minimal error in the conducted simulations. Here the system limitation error is also evaluated from the two aspects (dimensional parameter and reflection points) as shown in Section 8.3.1.

Figure 8-8 shows the system limitation errors by applying ERS to different tested convex and concave surfaces. Here two dimensional error parameters, called system limitation error of boundary (LE-B) and depth (LE-D), are defined similarly as the definition of CE-D and CE-B in Eq.8-2 and Eq.8-3. As can be seen in Figure 8-8, the system limitation errors (LE-B and LE-D) are both much less than the non-optimal configuration errors (CE-B and CE-D) in Figure 8-6. In particular, the maximal boundary error LE-B is reduced from 2.8% to 0.1%, and the maximal depth error LE-D is reduced from 26.9% to 0.6%. Hence, the non-optimal configuration error appears to be the major contribution to the overall measurement error.

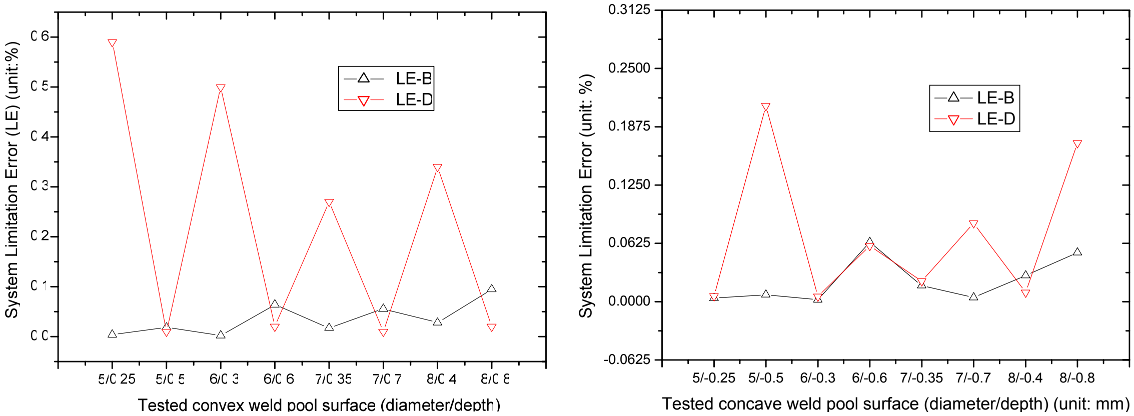

(a) Result by using convex surfaces (b) Result by using concave surfaces

Figure 8-8, System limitation error measured by using different surfaces

Figure 8-9 shows the computed average reflection error (ARE) and the actual ARE. It can be seen the results are much smaller than that in the non-optimal configuration error simulation. The performance by using convex surfaces is a little better than that by using concave surfaces. As the same, the computed ARE is larger than actual ARE and the actual ARE can even be neglectable.

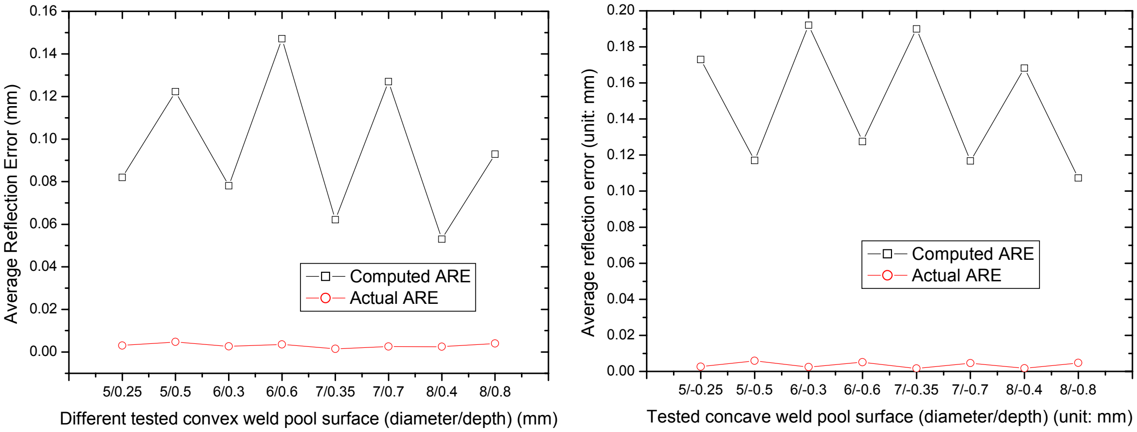

(a) Result by using convex surfaces (b) Result by using concave surfaces

Figure 8-9, Computed ARE and actual ARE by using different surfaces

It can be seen from Figure 8-8 and Figure 8-9, the system limitation error in the proposed system is very small. Further, it is apparent that the system limitation error computed above also includes the reconstruction methodology error. Hence, to understand and estimate the contribution of the reconstruction methodology to the system limitation error, an investigation is needed to estimate the error caused by the reconstruction method.

8.3.3 Reconstruction methodology error

In the proposed measurement system, reconstruction scheme is the last but the most important process used to reconstruct the weld pool surface. As can be seen above, non-optimal or imprecise inputs used by the reconstruction scheme can cause errors. Meanwhile the scheme itself may also introduce error because of some assumptions and approximations taken in it.

In order to eliminate the impact of other error sources, the same simulations as section 8.3.2 is done while the used projected laser pattern is improved with a 39-by-39 dot-matrix. Although its scale is not approaching infinite-by-infinite, it is still reasonable to use it to investigate the improved error performance quantitatively and obtain the approximate value of reconstruction methodology error. In the simulation, the inter-beam angle of the dot-matrix laser pattern is decreased to 0.385 degree (half of its original value) accordingly so as to make the dot projected denser without changing the projection area too much.

Figure 8-10 shows the computed reconstruction methodology errors. Here reconstruction methodology error of boundary (ME-B) and depth (ME-D) are also defined according to Eq.8-2 and Eq.8-3. Compared with the result of using 19-by-19 dot-matrix pattern, the reconstruction methodology error by using 39-by-39 pattern is much less, and the values of ME-B and ME-D approach to zero for both convex and concave surfaces. If given infinite dense projected dot-matrix, the reconstruction methodology error should not even exist.

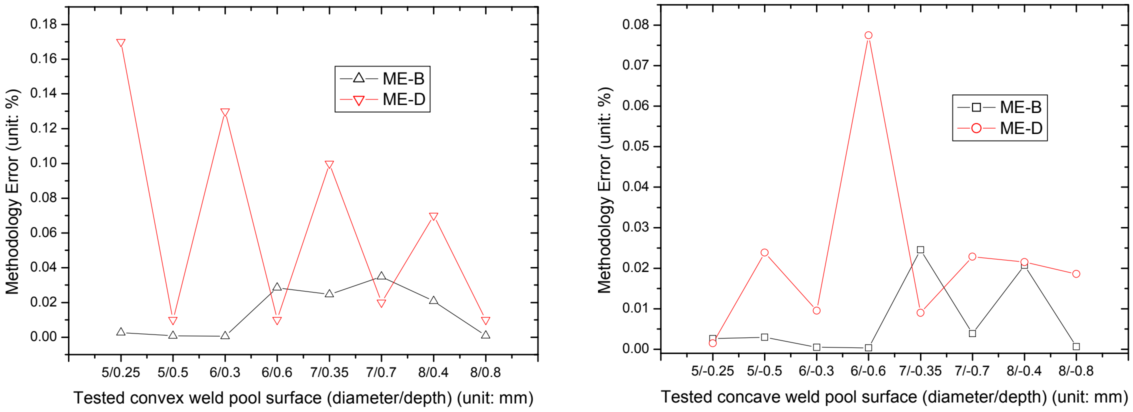

(a) Result by using convex surfaces

(b) Result by using concave surfaces

Figure 8-10, Reconstruction methodology errors using different surfaces

Figure 8-11 shows the computed average reflection error (ARE) and the actual ARE. It can be seen the result is also much smaller than that in the system limitation error simulation. Both computed and actual AREs are extremely small and approach to zero. The insignificant reconstruction methodology errors proved the accuracy of the proposed reconstruction scheme and validated the three-dimensional specular weld pool surface measurement system.

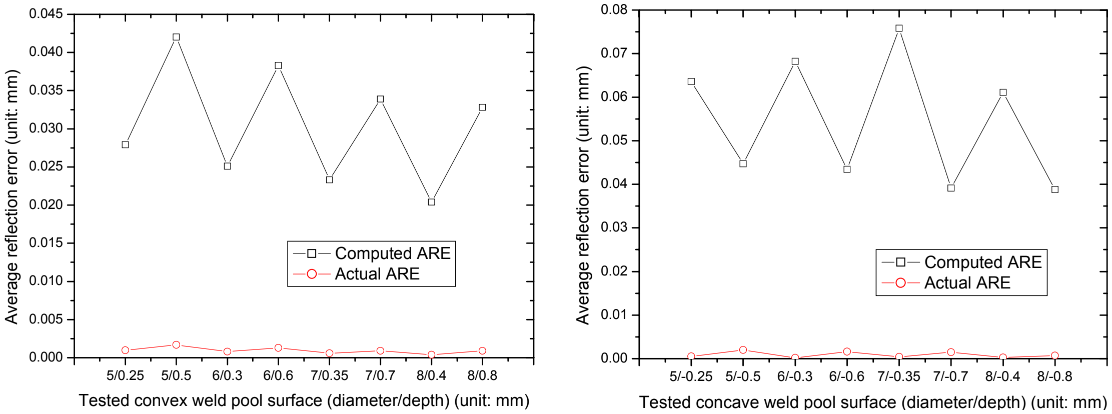

(a) Result by using convex surfaces (b) Result by using concave surfaces

Figure 8-11, Computed ARE and actual ARE by using different surfaces

8.4 Summary

Since the actual dimensional information of the molten weld pool can not be obtained directly through welding experiments, a series of simulated experiments have been conducted to evaluate the various errors in the proposed measurement system. In the measurement system, induced errors have been classified into three major types: system limitation error, usage error and processing error. Through the experiments and error analysis, the authors found:

- The non-optimal configuration error is the major error source contributed to the overall measurement error of the weld pool surface. Other error sources studied including the system limitation error and surface reconstruction methodology error are relatively insignificant.
- The non-optimal configuration error is primarily caused by the mismatch of the projected laser pattern in relation to the particular weld pool surface to be measured. When the mismatch is eliminated, the configuration

becomes optimal and the error reduces to the system limitation error. Reduction of the mismatch may be a method to improve the measurement accuracy significantly without changing either the components of the measurement system or the surface reconstruction method. While in practical experiments, the variance of the weld pool surface makes it difficult to always achieve optimal configuration. Thus increase of the density of projected laser dot-matrix appears to be a more practical and effective way to reduce both non-optimal configuration error and system limitation error.

- Through the test for a physical object with known dimensions, the measurement error is obtained. The reasonably small measurement error verified the accuracy of the proposed three-dimensional specular surface measurement system.

CHAPTER 9

CONCLUSION AND FUTURE WORK

9.1 Conclusion

Welding processes are widely used in many manufacturing areas, such as automotive, aerospace and shipbuilding industries. Meanwhile, welding is a labor intensive and skill required operation. Although current welding robots can assure and help improve productivity, they lack the intelligent capabilities to achieve good weld quality through ‘observation’ of welding process. Hence, observation and measurement of weld pool surface is a fundamental capability that next generation automated welding machines must possess.

In this dissertation, a new machine vision system is proposed in order to precisely measure the three-dimensional weld pool surface. The main work in the thesis includes three parts: establishment of weld pool surface sensing system (Chapter.3 and Chapter.4), processing of acquired reflected images (Chapter.5) and reconstruction of three-dimensional weld pool surface based on achieved information (Chapter.6 and Chapter.7). The three procedures can be briefly described as “Acquisition’, ‘Processing’ and ‘Reconstruction’ process based on the operations for recorded reflected images. By using the developed system, the 3D shape of the weld pool surface can be computed off-line and error analysis verified the accuracy of reconstructed results and the validity of the proposed system (Chapter.8). This research is not only important for development of next generation intelligent welding machine, but also useful to provide reliable data for validation of welding process models.

The main achievements and contributions in this dissertation can be summarized as follow:

1. Proposed a new approach to effectively observe and measure weld pool surface. Different from the normal direct-view vision-based methods, in the proposed approach the reflection of projected structured laser light from

the specular weld pool surface can be clearly imaged to extract the pool surface shape, which takes advantage of the specular surface and the difference between propagation in an illumination laser and arc plasma.

2. Established a machine vision system using the proposed method. In the phase of implementation, the selection and displacement of system components assured the validity of the system. Through many experiments, the suitable system parameters are decided to achieve good results (clear reflected images), which give a good direction for system improvement.
3. Developed robust Image processing algorithms to effectively analyze the acquired reflected images. By applying them, some useful information, such as the reflected dots' coordinates and row/column positions, can be extracted. Combined with the results of correspondence simulation, the projected and reflected dot pair can thus be determined, which will be used for weld pool surface reconstruction.
4. Proposed interpolation and extrapolation reconstruction schemes (IRS and ERS) to rebuild three-dimensional weld pool surface and compared their performance. This research provides an effective way for the proposed system to reconstruct the weld pool surface off-line, and it is also valuable for developing real-time sensing system. The reconstruction results verified the accuracy of the machine vision measurement system.
5. Analyzed the errors existing in the proposed system. The error sources are classified and investigated quantitatively by simulations. The analysis shows the main error comes from non-optimal configuration and it also proved the insignificant errors induced by the system limitation and proposed reconstruction method. Through error analysis, reasonable approaches can be adopted to improve the proposed system.

9.2 Future work

The proposed system used in this dissertation is intended for laboratory experiments and realized only for off-line processing. To make the system more practical and be used in next generation intelligent welding machines, more future work can be done in different aspects to improve the design and algorithms of the machine vision sensing system, which include:

1. Simplify design and make system compact

To simplify the system design, the imaging system consisting of the imaging plane, band-pass filter and the camera as used in this dissertation should be replaced by an imaging sensor chip behind a band-pass filter without any lenses. But the limited practical size of the sensor chip is a further problem for the improvement.

One more practical improvement is to make laser diode parallel to the torch and use highly reflective mirror with adjustable angle to reflect incoming laser light onto the weld pool. In the meantime, the imaging plane is rotated at an angle to make the reflected image can be captured by a compact camera. The drafts of the possible designs are shown in Figure 9-1.

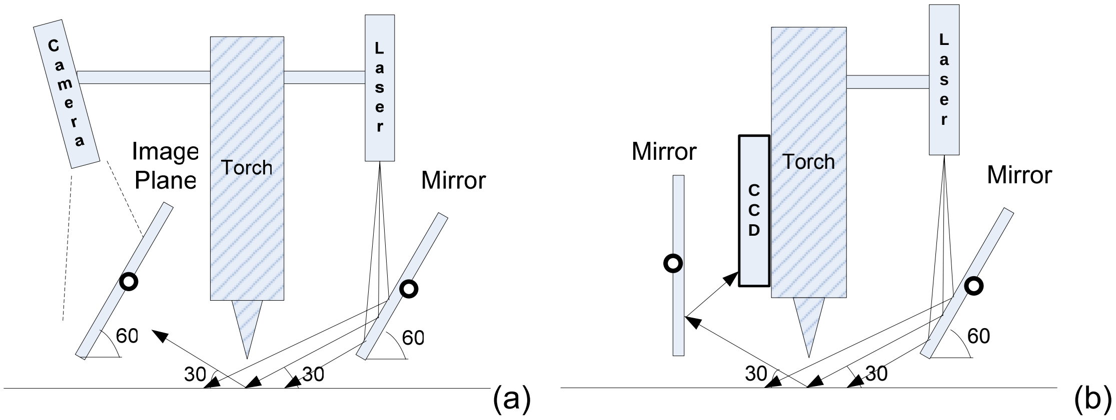

Figure 9-1, Two possible improvements of system design

Furthermore, to ensure clear reflected images captured, the system position parameters should be adjustable according to an intelligent image decision system (software part), which can decide if the obtained image is clear enough for further processing. This is helpful especially for the applications by using robots.

2. Improve the projected laser pattern and power

From the system error analysis, it can be seen if the projected laser dot-matrix become denser, the system performance would be greatly improved. Thus if possible denser commercial available laser pattern should be applied to improve the sensing system.

In our experiments, the power of continuous laser is only 20 mW. In order to improve the contrast of the reflected images and ease the image processing algorithm, the laser diode with larger power should be used. It is also necessary in the applications by using large welding current.

3. Realize real-time measurement and control

One important reason for establishing the machine vision measurement system is to realize on-line quality control during the welding processes. To achieve this goal, the current used image processing algorithms and reconstruction schemes should be simplified and expedited to be suitable for real-time environment. Meanwhile the model of weld pool surface related to the welding parameters should be developed and proper on-line control algorithms should be applied to realize real-time three-dimensional weld pool surface control, which is the ultimate objective of our research.

APPENDIX I

LASER CALIBRATION

Calibration of laser is done during the experiment configuration, which is used to measure the position and the projection angle of laser diode precisely [52]. Since it is not possible to measure the parameters directly, a new cross-hair pattern diffractive lens is used for laser calibration. Once its position is fixed, another lens with needed pattern can be used to replace it.

For our application a model SNF-501H laser (20 mW laser centered at 685nm) fitted with a cross-hair generation optic is used for calibration. The fan angle θ of the laser is 10 degree. Because the cross hair formed on the plane changes with laser position, measuring the cross hair length and knowing the fan angle can reveal the position of the laser. If the laser is perpendicular to the projection plane, then all the cross hair lengths will be equal. The distance of the laser from the plane can be found out by measuring the length of the cross hair as shown in Figure A-1 (a), and the distance x_l is given as $x_l = \frac{l_1}{\tan(\alpha)}$, where $\alpha = \frac{\theta}{2}$ is half of the laser fan angle.

Now consider the calibration which requires the laser projected onto the work piece plane at an angle inclined in just one direction with the pattern projected aligned with the tilt as shown in Figure A-1 (b). The pattern formed on the plane have different cross hair lengths, i.e., l_2 is longer than l_1 and each horizontal line (l_3) is equal in length. The distance x_l can be computed using the horizontal cross hair lengths l_3 as $x_l = \frac{l_3}{\tan(\alpha)}$. Length l_3 will not be distorted by the projection angle of the laser, where as lengths l_1 and l_2 will be distorted and can be used to determine the angle of tilt which is denoted as α_5 in Figure A-1 (b). To this end, a perpendicular plane to the laser (i.e., with the laser axis as its normal) is drawn at a distance x_l across the center of cross hair as shown in Figure A-1 (b)

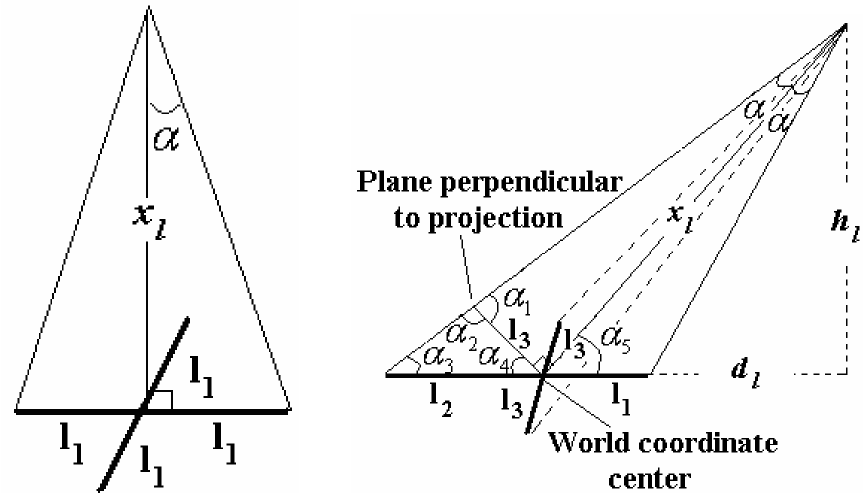

(a) (b)

Figure A-1, Laser calibration. (a) Laser projected perpendicular to the surface. (b) Laser projected at an angle (alpha5) to the surface. [52]

and the least angle this plane forms with the front incident laser ray is α_1. The length of all laser hairs on this perpendicular plane will be l_3 based on the geometry of projection. The angle α_1 will be $\alpha_1 = 90^o - \alpha$, and therefore $\alpha_2 = 180^o - \alpha_1$. Using the law of sines α_3 can be found to be $\alpha_3 = \sin^{-1}\left(\frac{l_3}{l_2}.\sin(\alpha_2)\right)$. Hence $\alpha_4 = 180^o - (\alpha_2 + \alpha_3)$ can be calculated and α_5 (the angle of the laser projection) is given by $\alpha_5 = 90^o - \alpha_4$. The height of the laser from the projection plane is given by $h_l = x_l.\sin(\alpha_5)$, and the distance by $d_l = x_l.\cos(\alpha_5)$. Hence the distance, height and angle of the laser in relation to the center of the cross hair which is aligned with the origin of the world coordinate system are obtained and the laser is calibrated.

APPENDIX II

EXPERIMENTAL INSTRUCTIONS

Here the procedures to set up the observation system are discussed in detail. The list of necessary equipments is also presented.

Before system configuration, two safety alerts should be addressed for the process. One is the “Laser safety”. The class IIIb laser diode of 20 mW is used in this experiment. Some issues about safety operation of laser should be remembered. Do not project the laser directly into your or someone else’s eyes! It is very dangerous, and may cause eye injury. And always remember to wear special goggles when operate the laser diode, which can filter out the laser at certain wavelength. In the experiment, the wavelength of the laser is 685nm. Related knowledge can be found in the website: http://ehs.uky.edu/classes/laser/lastrain.html.

Another issue is “Welding safety”, which is about the welding process itself. During process, strong arc light and sometimes some splattering will occur. So before welding, welding goggles and dress should be worn. And do not approach the welding arc or use hands to touch it because the temperature of arc is very high.

The main steps to set up the experiment are listed below. The system picture is shown in Figure A-2 (camera is not included).

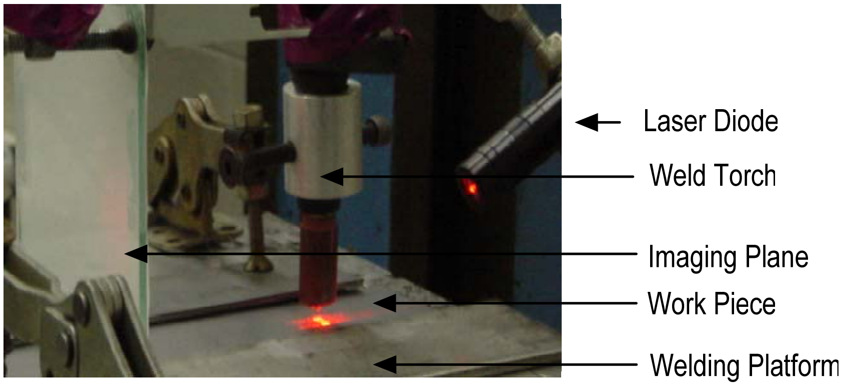

Figure A-2, Experiment system setup

Step 1: Put one piece of 2mm mild steel on the welding platform. Here in order to simplify the process, only one work piece is used instead of two. The experiment result should be the same for the observation of weld pool surface.

Step 2: Place the GTAW welding torch vertically above the work piece and the distance between the tungsten electrode tip and the surface of work piece is about 3~5 mm, which enable the start of welding arc.

Step 3: The structure laser diode is placed along the welding direction with an angle about 30 degree. The distance between the laser head and electrode tip is approximately 90 mm for 5-line pattern, 35 mm for 19*19 dot-matrix pattern. When multiple-line pattern is projected onto the work piece, make sure that the pattern cover the whole area of weld pool below the electrode tip and the lines are vertical to welding direction. Here some more calibration steps will be needed if the result of the experiment is used for measurement of weld pool surface, the laser position should be measured precisely by using the calibration method in Appendix I.

Step 4: An imaging plane is placed parallel to the OXZ plane at a distance of around 50 mm from the axis of the electrode (i.e., axis Z). The imaging plane is fixed on the other side of torch, which is vertically to the work piece and the welding direction. In the experiment, the objective of imaging plane is to intercept the reflected laser light and it can be as simple as a piece of paper attached on a square glass.

Step 5: Place the high-speed camera about 2 meters away and vertically to the imaging plane. A 20nm band-pass filter is used in the camera, which is centered at 685nm (wavelength of laser diode). Adjust the focus and aperture to make the imaging plane can be clearly seen through the camera. The recording speed is set to 60 frames per second or higher.

Step 6: Turn on the GTAW machine, water cooling system and shielding gas. Put some welding wires between the electrode tip and work piece and put on welding goggles. Switch on the welding machine power and adjust the welding current to a reasonable range (65-75 A). At the same time, start the movement of welding platform and turn on the camera to record. After a while, the clear reflection image should be seen by the camera. If the welding current is changed, the change of reflection images can also be seen, which reflected the change of the status of weld pool surface. At last, turn off the welding machine to end the experiment.

The equipments and tools used in the observation system of weld pool surface are listed below:

- PULSEWELD gas tungsten arc welding (GTAW) machine with cooling system and shielding gas;
- Welding platform;
- StockerYale Laser Diode (wavelength: 685nm, power: 20mW) with the following diffractive lens:
    1. Five-line pattern - fan angle: 5 degree, inter-beam angle: 0.23 degree);
    2. 19-by-19 dot-matrix pattern – inter-beam angle: 0.77 degree
- Imaging plane;
- Olympus *i-SPEED* high-speed camera;
- Laser protection goggle for 685nm laser;
- Welding safety goggles and clothes.

REFERENCE

[1] Groenwald, R. A., Mathieson, T. A., Kedzior, C. T. and Gaid, I.N.C., “Acoustic emission weld monitor system – data acquisition and investigation”, US Army Tank-Automotive Research and Development Command Report ADA085-518, October 1979.

[2] Siores, E., “Development of a realtime ultrasonic sensing system for automated and robotic welding”, PhD Thesis, Brunel University, December 1988.

[3] Guu A. C.and Rokhlin S., “Computerized radiographic weld penetration control with feedback on weld pool depression”, Mater. Eval. 47 1204–10, 1989.

[4] Gohar M. Saeed, “3 Dimensional Measurement of Specular Surfaces and Its Application in Welding Process”, Ph.D thesis, University of Kentucky, 2005

[5] R. Kovacevic, Y. M. Zhang, and S. Ruan, "Sensing and control of weld pool geometry for automated GTA welding," ASME Journal of Engineering for Industry, 117(2): 210-222, 1995.

[6] R. Kovacevic, Y. M. Zhang, "Real-time image processing for monitoring of free weld pool surface," ASME Journal of Manufacturing Science and Engineering, 119(2): 161-169, 1997.

[7] Mnich, C., Al-Bayat, F., Debrunner, C., Steele, J., Vincent, T., “In Situ Weld Pool Measurement using Stereovision”, ASME, Proceedings 2004, Japan – USA Symposium on Flexible Automation, Denver, Colorado, July 19-21, 2004.

[8] Choong Don Yoo and Jihye Lee, 3D measurement of weld pool using biprism

stereo vision sensor, http://joining1.kaist.ac.kr/research/vision.htm, Seoul National University.

[9] Y.M. Zhang, H.S. Song, and G. Saeed, 2006, “Observation of a dynamic specular weld pool surface,” Measurement Science & Technology, 17 (6): L9-L12.

[10] Hongsheng Song, Gohar Saeed and YuMing Zhang, 2006, “Observation of Dynamic Specular Weld Pool Surface”, Proceedings of 2006 ISFA (International Symposium on Flexible Automation), 0252-b(S) pg.661-662, Osaka, Japan, July 10-12, 2006

[11] Hongsheng Song, Yuming Zhang, “An Image Processing Scheme for Measurement of Specular Weld Pool Surface”, Proceedings of the 2nd IEEE Conference on Industrial Electronics and Applications (ICIEA 2007), Harbin, China, May 23-25, 2007

[12] Hongsheng Song, Yuming Zhang, “Image Processing for Measurement of Three-Dimensional GTA Weld Pool Surface”, Accepted for publication by Welding Journal.

[13] Hongsheng Song, Yuming Zhang, “Three-dimensional Reconstruction of Specular Surface for Gas Tungsten Arc Weld Pool”, (submitted to Measurement Science & Technology)

[14] Allen Sun and Elljah Kannatey-Asibu, Jr., “Sensor systems for real-time monitoring of laser weld quality”, Journal of Laser Applications, Volume 11, Number 4 153-168, Aug 1999

[15] W. Swaim. “Gas tungsten arc welding made easy,” Welding Journal, 77(9): 51-52, 1998

[16] R. Kovacevic, Y. M. Zhang, and S. Ruan, "Sensing and control of weld pool geometry for automated GTA welding," ASME Journal of Engineering for Industry, 117(2): 210-222, 1995..

[17] Mingji Lou, ”Computation of Weld Pool Surface from Specular Reflection and Optical Flow”, Master Thesis, University of Kentucky, 2004

[18] C. S. Wu, P. C. Zhao, and Y. M. Zhang, “Numerical simulation of transient 3-D surface deformation of full-penetrated GTA weld pool,” Welding Journal, 83(12): 330s-335s, 2004.

[19] http://en.wikipedia.org/wiki/Machine_vision

[20] Y. M. Zhang, R. Kovacevic, and L. Li, "Adaptive control of full penetration GTA welding," IEEE Transactions on Control Systems Technology, 4(4): 394-403, 1996

[21] Gohar Saeed, “Vision-based sensing of the welding process: a survey”, Int. J. Modelling, Identification and Control, 2005

[22] Kovacevic, R, Zhang, Y.M. and Ruan, S. (1995), “Sensing and control of weld pool geometry for automated GTA welding”, ASME Journal of Engineering for Industry, Vol.117, No.2, pp.210-222.

[23] Richardson, R.W. et al. (1984), “Coaxial arc weld pool viewing for process monitoring and control”, Welding Journal, Vol.63, No.3, ppl43-50.

[24] Wu, C. S., Gao, J. Q., Liu, X. F, Zhao, Y. H., “Vision-based measurement of weld pool geometry in constant-current gas tungsten arc welding”. Proc. Instn Mech. Engrs Vol. 217 Journal engineering manufacture. IMechE 2003.

[25] Peiyong Duan and Yu Ming Zhang, “CMAC-based modelling for HPDDL welding process control”, International Journal of Modelling, Identification and Control, Volume 1, Number 2 / 2006, pp. 107 – 114.

[26] Kovacevic R and Zhang Y M, “Real-time image processing for monitoring of free weld pool surface”, ASME J. Manuf. Sci. Eng. 119 161–9, 1997

[27] Yu J-Y and Na S J, “Study on vision sensors for seam tracking of height-varying weldment”, Mechatronics 8, 21–36, 1998

[28] Bonser G and Parker G A, “Robotic gas metal arc welding of small diameter saddle type joints using multistripe structured light”, Opt. Eng. 38 1943–9, 1999

[29] Zhang Y M and Li L, “Interval model based robust control of weld joint penetration”, ASME J. Manuf. Sci. Eng. 121 425–33, 1999

[30] Klein M V and Furtak T E, Optics (New York: Wiley) chapter 3, 1986

[31] Saeed G., Lou M. J., and Zhang, Y. M., “Computation of 3D weld pool surface from the slope field and point tracking of laser beams”. Measurement Science and Technology, 15(2): 389-403, (2004).

[32] Mnich, C., Al-Bayat, F., Debrunner, C., Steele, J., Vincent, T., “In Situ Weld Pool Measurement using Stereovision”, ASME, Proceedings 2004, Japan – USA Symposium on Flexible Automation, Denver, Colorado, July 19-21, (2004).

[33] Choong Don Yoo and Jihye Lee, 3D measurement of weld pool using biprism stereo vision sensor, http://joining1.kaist.ac.kr/research/vision.htm, Seoul National University.

[34] G. Saeed, “3 Dimensional Measurement of Specular Surfaces and Its Application in Welding Process”, Ph.D thesis, University of Kentucky, 2005

[35] Zhao, D.B., Yi, J.Q., Chen, S.B., Wu, L. and Chen, Q. (2003), “Extraction of Three-Dimensional Parameters for Weld Pool Surface in Pulsed GTAW With Wire Filler”, ASME J. Manuf. Sci. Eng. Vol. 125, pp.493-503

[36] Zhang Guangjun, Yan Zhihong and Wu Lin, “Reconstructing a three-dimensional P-GMAW weld pool shape from a two-dimensional visual image”, Meas. Sci. Technol. 17 (2006) 1877–1882

[37] P.C.J. Anderson, “Sensor systems for top-face penetration control”, Industrial Robot Vol. 22 No. 4, 1995, pp. 12-15, MCB University Press, 0143-991X.

[38] Guu A. C.and Rokhlin S., “Computerized radiographic weld penetration control with feedback on weld pool depression”, Mater. Eval. 47 1204–10, 1989.

[39] Siores, E., “Development of a realtime ultrasonic sensing system for automated and robotic welding”, PhD Thesis, Brunel University, December 1988.

[40] Lucas, W. and Maller, R.S., “Automatic control of penetration in pulsed TIG welding”, TWI Members Report P/72/1975.

[41] Groenwald, R. A., Mathieson, T. A., Kedzior, C. T. and Gaid, I.N.C., “Acoustic emission weld monitor system – data acquisition and investigation”, US Army Tank-Automotive Research and Development Command Report ADA085-518, October 1979.

[42] Chin, B.A., Madsen, N.H. and Goodling, J.S., “Infrared thermography for sensing the arc welding process”, Welding Journal, Vol. 62 No. 9, September 1983, pp. 227s-34s.

[43] Madigan, R.B., Renwich, R.J., Farson, D.F. and Richardson, R.W. “Computer-based control of full penetration GTA welds using weld pool oscillation sensing”, First International Conference on Computer Technology in Welding, Cambridge, 1987, pp. 165-74.

[44] Hongsheng Song, Gohar Saeed and YuMing Zhang, “Observation of Dynamic Specular Weld Pool Surface”, Proceedings of 2006 ISFA (International Symposium on Flexible Automation), 0252-b(S) pg.661-662, Osaka, Japan, July 10-12, 2006

[45] Y.M. Zhang, H.S. Song, and G. Saeed, “Observation of a dynamic specular weld pool surface,” MEASUREMENT SCIENCE & TECHNOLOGY 17 (6): L9-L12 JUN 2006.

[46] http://en.wikipedia.org/wiki/Machine_vision

[47] http://www.stockeryale.com/i/lasers/structured_light.htm

[48] http://en.wikipedia.org/wiki/Gas_tungsten_arc_welding

[49] G. Saeed, “3 Dimensional Measurement of Specular Surfaces and Its Application in Welding Process”, Ph.D thesis, University of Kentucky, 2005

[50] R. Kovacevic, Y. M. Zhang, and S. Ruan, "Sensing and control of weld pool geometry for automated GTA welding," ASME Journal of Engineering for Industry, 117(2): 210-222, 1995.

[51] Saeed G., Lou M. J., and Zhang, Y. M., "Computation of 3D weld pool surface from the slope field and point tracking of laser beams". Measurement Science and Technology, 15(2): 389-403, (2004).

[52] G. Saeed, "3 Dimensional Measurement of Specular Surfaces and Its Application in Welding Process", Ph.D thesis, University of Kentucky, 2005

[53] Mingjie Lou, "Computation of Weld Pool Surface from Specular Reflection and Optical Flow", Master thesis, University of Kentucky, 2004

[54] Rafael C. Gonzalez, Richard E. Woods, "Digital Image Processing", second edition, Prentice Hall, 2002

[55] Wesley E. Snyder and Hairong Qi, "Machine Vision", Cambridge University Press, ISBN 052183046X, 2004

[56] Kenneth R. Castleman, "Digital Image Processing", Prentice Hall, 1996

[57] R. Kovacevic and Y. M. Zhang, "Machine vision recognition of weld pool in GTAW," Proceedings of the Institution of Mechanical Engineers, Part B: Journal of Engineering Manufacture, 208(B2): 141-152, 1995.

[58] Y. M. Zhang, and R. Kovacevic, "Real-time sensing of sag geometry during GTA welding," ASME Journal of Manufacturing Science and Engineering, 119(2): 151-160, 1997.

[59] R. Kovacevic, Y. M. Zhang, "Real-time image processing for monitoring of free weld pool surface," ASME Journal of Manufacturing Science and Engineering, 119(2): 161-169, 1997.

[60] Mingjie Lou, "Computation of Weld Pool Surface from Specular Reflection and Optical Flow", Master thesis, University of Kentucky, 2003

[61] Barber, C. B., D.P. Dobkin, and H.T. Huhdanpaa, "The Quickhull Algorithm for Convex Hulls," ACM Transactions on Mathematical Software, Vol. 22, No. 4, Dec. 1996, p. 469-483.

[62] R. Kovacevic and Y. M. Zhang, "Machine vision recognition of weld pool in GTAW," Proceedings of the Institution of Mechanical Engineers, Part B: Journal of Engineering Manufacture, 208(B2): 141-152, 1995.

[63] R. Kovacevic, Y. M. Zhang, and L. Li, "Monitoring of weld penetration based on weld pool geometrical appearance," Welding Journal, 75(10): 317s-329s, 1996.

[64] Sandwell, David T., “Biharmonic Spline Interpolation of GEOS-3 and SEASAT Altimeter Data”, Geophysical Research Letters, 2, 139-142,1987.

VITA

Hongsheng Song was born on September 22, 1976 in XiangTan, HuNan, China.

EDUCATION:

Beijing University of Posts and Telecommunications, China 06/2004
Ph.D. in Telecommunication Engineering

Beijing University of Posts and Telecommunications, China 07/1999
B.S. in Electrical Engineering

RECENT AWARD:
Kentucky Opportunity Fellowship (07/2006 – present)

PUBLICATIONS:
Journal Papers:

1. Y.M. Zhang, H.S. Song, and G. Saeed, "Observation of a dynamic specular weld pool surface," *MEASUREMENT SCIENCE & TECHNOLOGY* 17 (6): L9-L12 JUN 2006.

2. Song, H.S. and Zhang, Y.M., "An Image Processing Scheme for Measurement of Specular Weld Pool Surface", accepted for publication, *Welding Journal*.

3. Hongsheng Song and YuMing Zhang, "Three-dimensional Reconstruction of Specular Surface for Gas Tungsten Arc Weld Pool", (Submitted to *MEASUREMENT SCIENCE & TECHNOLOGY*, in review)

4. Hongsheng Song and YuMing Zhang, "Measurement and Analysis of Three-dimensional Specular Gas Tungsten Arc Weld Pool Surface", (Submitted to Welding Journal, in review)

5. Hongsheng Song and YuMing Zhang, “Error Analysis of Three-dimensional Specular Surface Measurement System for GTA Weld Pool”. (in review)

Conference Papers:

1. Hongsheng Song, Yuming Zhang,” An Image Processing Scheme for Measurement of Gas Tungsten Arc Weld Pool Surface”, *IEEE Conference on Industrial Electronics and Applications (ICIEA 2007)*, May 2007

2. Hongsheng Song, “Measurement of Gas Tungsten Arc Weld Pool Surface”, *2006 FABTECH International & AWS Welding Show*, Georgia World Congress Center, Atlanta Georgia USA, Oct 31 - Nov 2, 2006

3. Hongsheng Song, Gohar Saeed and YuMing Zhang, “Observation of Dynamic Specular Weld Pool Surface”, *Proceedings of 2006 ISFA (International Symposium on Flexible Automation)*, 0252-b(S) pg.661-662, Osaka, Japan, July 10-12, 2006

Hongsheng Song

07/24/2007